C

liegt aus

Measurement of the Cross Section and t Distribution in Diffractive Deep Inelastic Scattering at HERA

by

E. Barberis

University of California
Santa Cruz

Measurement of the Cross Section and t Distribution in Diffractive Deep Inelastic Scattering at HERA

A dissertation submitted in partial satisfaction
of the requirements for the degree of

Doctor of Philosophy

in

Physics

by

Emanuela Barberis

July 1996

To Basil

UNIVERSITY OF CALIFORNIA
SANTA CRUZ

Measurement of the Cross Section and t Distribution in Diffractive Deep Inelastic Scattering at HERA

A dissertation submitted in partial satisfaction
of the requirements for the degree of

DOCTOR OF PHILOSOPHY

in

PHYSICS

by

EMANUELA BARBERIS

July 1996

Abstract

Diffractive events in proton-positron deep inelastic scattering are studied at HERA with the ZEUS detector. The selection criterium is based either on the presence of a rapidity gap, produced through the exchange of a pomeron between the outgoing proton system and the remaining hadronic system, or on the identification of the diffracted proton by the ZEUS Leading Proton Spectrometer. The properties of the events are investigated and measurements of the diffractive cross section and the diffractive structure function are presented.

Contents

List of Figures

List of Tables

Introduction

≪You have missed the point completely, Julia.
There *were* no tigers. *That* was the point≫.

T.S. Eliot, *The Cocktail Party*

This thesis reports on the study of diffraction in inclusive $e - p$ deep inelastic scattering collisions at HERA with the ZEUS detector. Diffraction was extensively studied in hadron-hadron interactions about thirty years ago, when, using a purely phenomenological approach, a mathematical formalism was developed to reproduce the asymptotic behaviour of diffractive cross sections. HERA offers the unique possibility to resolve the structure of diffraction at different scales using the virtual photon as a probe. By requiring the scale governing the interaction to be large, through a large photon virtuality, the dynamics of diffraction can be investigated and compared to perturbative calculations.

The two measurements described in this thesis took place over a two year period and share many common features, notably the the preparation and use of a dedicated detector component, the Leading Proton Spectrometer (LPS).

Diffractive processes are understood to proceed through the exchange of a colourless object which carries the quantum numbers of the vacuum; in $e - p$ diffractive collisions the proton emerges intact from the interaction and is deflected through a very small angle, thus escaping undetected in the beam pipe. The LPS is an in-pipe detector complex which allows one to tag and reconstruct the momentum of the diffracted proton, completing the kinematics determination of the event and offering, by far, the most correct selection criterium for diffraction.

The thesis is organised as follows:

- The first chapter gives a very brief overview of the theory of deep inelastic scatter-
ing. Diffraction is introduced through the study of hadron-hadron reactions and the
applicability of the hadronic picture of diffraction to $e - p$ collisions at small photon
virtualities. Diffraction at large photon virtualities is discussed in connection with the
experimental observations on the behaviour of diffractive and elastic cross sections at
large interaction scales. The relevant theoretical models for deep inelastic diffractive
scattering are reviewed.

- The second chapter gives a description of the HERA collider and the ZEUS apparatus.
Particular emphasis is placed on those components used extensively in this analysis.

- The third chapter describes the LPS. In particular its general hardware characteristics, mechanics, design, testing and detector module assembly are described.

- A description of the ZEUS software and the Monte Carlo generators used to simulate diffractive processes and related backgrounds is contained in the fourth chapter.

- The fifth chapter summarises the performance of the LPS during the data taking period relevant to the present analysis. Its subsequent calibration, alignment and the basics of the track reconstruction are also described.

- The methods of reconstruction of the event kinematics are discussed in the sixth chapter. The event selection procedure is discussed at length in the seventh chapter including the selection criteria necessary to improve the accuracy of the reconstruction, and to suppress the various backgrounds. The statistics and event characteristics of the final sample are then given.

- Chapter eight contains the first determination, using the LPS, of the dependence of the DIS diffractive cross section on the four-momentum transfer at the proton vertex.

- Without the tagging of an intact proton emerging from the interaction, the measurement of diffraction at HERA has been based on the identification of a particular topology in the final state (i.e. the presence of a large gap in pseudo-rapidity between the outgoing proton direction and the remaining hadronic final state) which is consistent with the exchange of a colourless object. The measurement of the diffractive structure function based on the selection of the event topology is discussed in chapter nine, while, in the last chapter, the diffractive structure function is extracted using the LPS, both for the event tagging and the kinematics reconstruction. The comparison between the two measurements and the improvements introduced by the LPS are discussed.

This thesis contains the first analysis of deep inelastic diffractive scattering events selected with the LPS. The data were collected during the 1994 running period. A number of measurements not possible in this first analysis, due to the limited statistics, will be possible with the analysis of the 1995 LPS data. In 1995 the increase of the delivered luminosity and the installation of the second half of the spectrometer translated into a factor of ~ 6 increase in statistics.

Chapter 1

Theoretical review

1.1 Deep Inelastic Scattering (DIS)

1.1.1 Electron-Proton elastic scattering

The cross section for elastic scattering of an unpolarised point-like charged particle, for example an electron, on an extended target such as a proton, can be derived by comparison with the cross section for scattering electrons from a point charge (see Fig. 1.1a), given by [1, 2]:

$$\frac{d\sigma}{d\Omega} = \left(\frac{d\sigma}{d\Omega}\right)_{point} |F(q)|^2, \qquad (1.1)$$

where q is the momentum transfer between the incident electron beam and the target carried by the virtual photon, $q = k_f - k_i$, the subscripts i and f denote the initial and final state respectively, Ω is the solid angle around the outgoing electron and $F(q)$ is the form factor which describes the structure of the target[1]. For a structureless target with a static, spinless charge distribution[2] $Ze\rho(\vec{x})$, the cross section is:

$$\left(\frac{d\sigma}{d\Omega}\right)_{point} = \left(\frac{d\sigma}{d\Omega}\right)_{Mott} = \frac{(Z\alpha)^2 E^2}{4k^4 sin^4(\frac{\theta}{2})}\left(1 - v^2 sin^2\frac{\theta}{2}\right), \qquad (1.2)$$

where $k = |k_i| = |k_f|$, E is the energy of the incoming electron, $v = k/E$ and θ is the scattering angle of the electron.

In the case when the electron is scattering off a proton not only is the proton's charge involved but also its magnetic moment. Secondly, the proton is not stationary, but will recoil under the effect of the interaction. Assuming that the proton is a point with charge e having a Dirac magnetic moment of $e/2m_p$ then the expression for the cross section can be taken directly from electron-muon scattering by replacing the mass of the muon with the mass of the proton m_p [1]:

$$\frac{d\sigma}{d\Omega}|_{lab} = \left(\frac{\alpha^2}{4E^2 sin^4\frac{\theta}{2}}\right)\frac{E'}{E}\left\{cos^2\frac{\theta}{2} - \frac{q^2}{2m_p^2}sin^2\frac{\theta}{2}\right\}, \qquad (1.3)$$

---

[1]For a static target $F(q)$ is simply the Fourier transform of the charge distribution.
[2]Normalised so that $\int \rho(\vec{x})d^3x = 1$
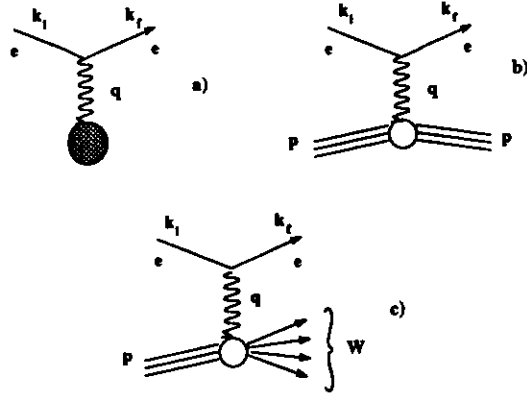
Figure 1.1: a) Electron elastic scattering by a Coulomb potential. b) Electron-proton elastic scattering. c) Inelastic electron-proton scattering.

where E' is the energy of the scattered electron, the factor $\frac{E'}{E} = \frac{1}{1+\frac{2E}{m_p}\sin^2\frac{\theta}{2}}$ is equal to unity for a non recoiling target, and the four momentum squared transferred in the process is $Q^2 = -q^2 = 4E'E\sin^2\frac{\theta}{2}$.

Finally one more ingredient is necessary in order to calculate the cross section for elastic electron-proton scattering (see Fig. 1.1b). Unlike the muon, the proton is not a point-like spin 1/2 particle, but an object of extended structure carrying both electric charge and spin. The expression for the elastic $e - p$ cross section, known as the Rosenbluth formula [3] thus becomes:

$$\frac{d\sigma}{d\Omega} = \frac{\alpha^2\cos^2\frac{\theta}{2}}{4E\sin^4\frac{\theta}{2}}\frac{E'}{E}\left\{\frac{G_E^2 + \tau G_M^2}{1+\tau} + 2\tau G_M^2\tan^2\frac{\theta}{2}\right\}, \quad (1.4)$$

where $\tau = \frac{Q^2}{4m_p^2}$ and G_E, G_M are the proton's electric and magnetic form factors[3]. Experimentally G_E and G_M are given [4] by:

$$G_E(q^2) \approx \frac{G_M(q^2)}{\kappa_p} \approx \frac{1}{(1-\frac{q^2}{0.7}GeV^2)^2}, \quad (1.5)$$

where $\kappa_p = 2.79$ is the magnetic moment of the proton. If the proton were a point-like structureless particle, the form factors would be $G_E(q^2) = G_M(q^2) = 1$. Thus, the non trivial dependence on q^2 indicates that the proton is an extended object with an estimated mean square charge radius of $< r_p^2 > \sim 10^{-13}cm$. Also, for large q^2, the elastic cross section falls off rapidly, since $G_E \approx G_M \approx q^{-4}$.

---

[3] $G_E(q^2)$ and $G_M(q^2)$ can be related via Fourier transforms to the proton charge and magnetic distributions when the recoil of the proton can be neglected, i.e. in the Lorentz frame where no energy is transferred to the proton (the so-called Breit frame).

1.1.2 Inelastic Electron-Proton scattering

With increasing Q^2, the proton is more likely to break into a multi-particle system of invariant mass $W^2 = (q+P)^2$ (Fig. 1.1c). The interaction scale shifts from the size of the proton radius to resolve the inner structure. The differential cross section can be written as the invariant product of two tensors:

$$d\sigma \sim L^e_{\mu\nu}W^{\mu\nu}, \quad (1.6)$$

where $L^e_{\mu\nu}$ describes the lepton vertex and can be calculated in the framework of Quantum Electrodynamics (QED), while $W^{\mu\nu}$ parameterises the hadronic vertex and can be written as the most general combination of the four momenta of the particles entering the vertex (q and P) and the metric tensor $g^{\mu\nu}$, compatible with parity and electromagnetic current conservation:

$$W^{\mu\nu} = W_1\left(-g^{\mu\nu} + \frac{q^\mu q^\nu}{q^2}\right) + W_2\frac{1}{m_p^2}\left(p^\mu - \frac{p\cdot q}{q^2}q^\mu\right)\left(p^\nu - \frac{p\cdot q}{q^2}q^\nu\right). \quad (1.7)$$

Unlike elastic scattering, where the process can be described by only one angle (or by Q^2), in the inelastic case there are two independent variables, chosen to be Q^2 and $\nu \equiv \frac{p\cdot q}{m_p} = E - E'$, the photon energy in the proton rest frame. The inelastic form factors $W_{1,2}$ depend only on Q^2 and ν. The inelastic cross section with respect to E' and $\theta(\Omega)$ can be written as:

$$\frac{d^2\sigma}{dE'd\Omega} = \frac{4\alpha^2 E'^2}{Q^4}\left\{W_2(\nu,Q^2)\cos^2\frac{\theta}{2} + 2W_1(\nu,Q^2)\sin^2\frac{\theta}{2}\right\}. \quad (1.8)$$

Experimentally [5] the inelastic cross section, for large values of W, $W \gg m_p$, has a much more moderate dependence on Q^2 than the elastic cross section (whose form factors fall with a $(1/Q^2)^2$ dependence). This suggests that the scattering takes place on point-like objects inside the proton, much as the large angle scattering on α particles in Rutherford's experiments suggested the presence of charged point-like nuclei inside the target atom. The point-like objects resolved in the proton are called "partons".

1.1.3 The parton model, Bjorken scaling

The parton model [6] pictures the inclusive scattering at large Q^2 as due to the incoherent sum of elastic interactions between the electron and the constituent spin 1/2 partons in the proton. The cross section for elastic electron-parton scattering resembles the $e - \mu$ scattering cross section:

$$\frac{d^2\sigma}{dQ^2 d\nu} = \frac{4\pi\alpha^2}{Q^2}\frac{E'}{E}\left[e_i^2\cos^2\frac{\theta}{2} + e_i^2\frac{Q^2}{2m_i^2}\sin^2\frac{\theta}{2}\right]\delta\left(\nu - \frac{Q^2}{2m_i}\right), \quad (1.9)$$

where e_i, m_i are the electric charge and the mass of parton i. Summing over all partons, the delta function which enforces the mass-shell condition of the final parton leads to a dependence of the form factors (or the more commonly used structure functions $F_{1,2}$) on $\omega = -\frac{q^2}{2\nu m_p}$ alone (Bjorken scaling [7]):

$$m_p W_1(\nu,q^2) \xrightarrow{large\ Q^2} F_1(\omega), \quad (1.10)$$

$$\nu W_2(\nu,q^2) \xrightarrow{large\ Q^2} F_2(\omega), \quad (1.11)$$

as proven by the SLAC experiments in 1969 [8]. The scaling is clearly identified as the result of the electron-parton interaction in the infinite momentum frame of the proton, where $|\vec{p}| \gg m_p, m_i$. In this frame, relativistic time dilation slows down the interaction rate of the partons, which can be considered as non interacting free particles. Energy and momentum conservation at the photon-parton vertex forces a photon of a given energy ν and Q^2 to interact only with partons that carry a fraction of the total proton momentum equal to:

$$x = \frac{Q^2}{2m_p\nu} = \frac{1}{\omega}. \tag{1.12}$$

After the collision hadronisation of the struck parton takes place without interfering with the photon-parton scattering. The distribution of parton momenta in the proton is described by the differential probability $f(x_i)$ of finding parton i with momentum fraction between x and $x + dx$ in the proton, with the constraint:

$$\sum_i \int dx\, x f_i(x) = 1. \tag{1.13}$$

The individual parton structure functions can be written, from the comparison of eqns. 1.8 and 1.9 as:

$$F_2^{parton}(\omega) = x\delta(x - \frac{1}{\omega}), \tag{1.14}$$

$$F_1^{parton}(\omega) = \frac{1}{2x\omega}\delta(x - \frac{1}{\omega}). \tag{1.15}$$

Integration over x and summation over all partons gives the following expressions for the proton's structure functions:

$$F_2(x) = \sum_i e_i^2 x f(x), \tag{1.16}$$

$$F_1(x) = \frac{1}{2x}F_2(x), \tag{1.17}$$

where the latter is known as the Callan-Gross [10] relation and is a direct consequence of the assumption for spin 1/2 free partons in the proton. These partons were later identified with the quarks that Gell-Man [11] and Zweig [12] had introduced in hadron spectroscopy, three "valence" quarks, $uud(udd)$, for the proton(neutron). In 1979 evidence for the existence of gluons was provided at DESY via the observation of three-jet events in e^+-e^- annihilation [9].

1.1.4 Quantum cromodynamics and partons evolution

The Quark Parton Model (QPM) ignores the presence of gluons in the proton. The data show, however, that a large fraction of the proton momentum cannot be accounted for by quarks alone; the scaling hypothesis does not hold for small(large) values of x where the structure function F_2 is observed to increase(decrease) with Q^2 (see Fig. 1.2). On the other hand, the fact that quarks are confined into hadrons implies the presence of strong binding forces among them. The theory governing the interactions between quarks via the exchange of gluons is called Quantum Cromodynamics (QCD) and it is more generally believed to govern strong interactions. QCD is a non abelian gauge theory based on the SU(3) symmetry group whose
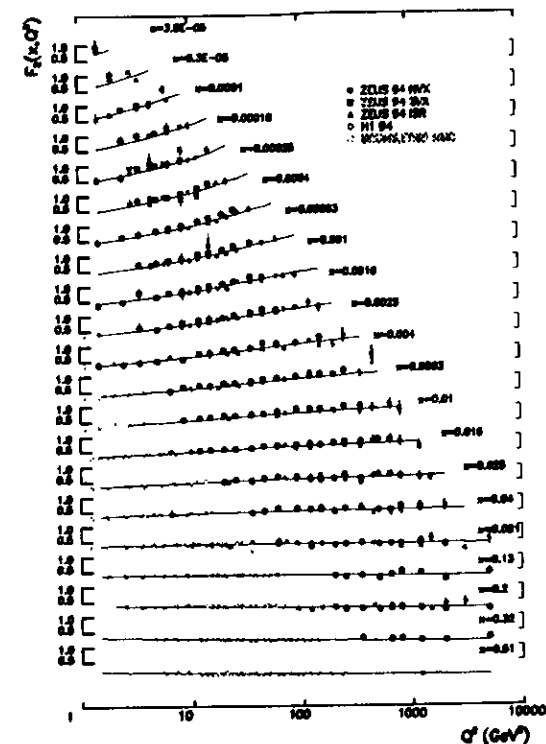
Figure 1.2: The structure function F_2 as a function of Q^2 for different x values. The ZEUS results as well as a compilation of fixed target results are shown.

representation predicts that each quark has three possible charges (colours); 8 gauge particles, called gluons, are responsible for transmitting colour forces among them. As a fundamental difference between QCD and QED, gluons carry the colour charge and can couple to each other. The coupling constant of strong interactions, α_s, is a function of the interaction scale; at high momentum transfers (high Q^2, short distances) it is small enough that quarks can be considered free (asymptotic freedom) and perturbation theory can be used to calculate the scattering amplitudes.

In deep inelastic scattering (DIS), the structure functions $F_{1,2}$ receive contributions from the diagrams where a quark can radiate a gluon before or after absorbing the virtual photon or where a gluon absorbs the virtual photon via the production of a quark-antiquark pair. As the scale that is probed inside the proton becomes smaller (increasing Q^2) a finer structure can be resolved, i.e. the splitting of gluons into quark-antiquark pairs or more gluons, and the radiation of gluons from quarks. Scaling is violated and the structure functions depend (logarithmically) on Q^2. The evolution of the parton densities with Q^2 is given by the

Dokshitzer-Gribov-Lipatov-Altarelli-Parisi equations (DGLAP) [13]; for quarks of flavour i:

$$\frac{dq_i(x,Q^2)}{dlnQ^2} = \frac{\alpha_s}{2\pi} \int_x^1 \frac{dy}{y} \left(q_i(y,Q^2)P_{qq}(\frac{x}{y}) + g(y,Q^2)P_{qg}(\frac{x}{y}) \right), \qquad (1.18)$$

and for gluons:

$$\frac{dg(x,Q^2)}{dlnQ^2} = \frac{\alpha_s}{2\pi} \int_x^1 \frac{dy}{y} \left(\sum_i q_i(y,Q^2)P_{gq}(\frac{x}{y}) + g(y,Q^2)P_{gg}(\frac{x}{y}) \right), \qquad (1.19)$$

where $y = \nu/E$ and P_{ij} are the lowest order splitting functions shown in Fig. 1.3. The
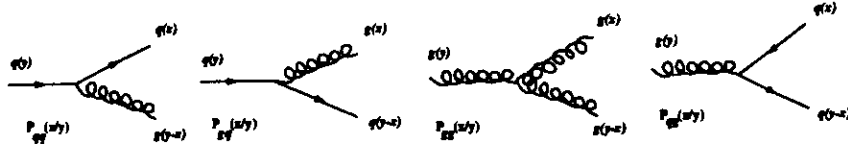
Figure 1.3: The splitting functions $P_{ij}(\frac{x}{y})$, that express the probabilities of finding a parton i inside parton j with a fraction $\frac{x}{y}$ of the parent momentum.

DGLAP equations express the fact that a quark or gluon with momentum fraction x could have originated from a parent parton with momentum fraction y with a probability $P_{ij}(\frac{x}{y})$. The number of "soft" quarks produced with a small fraction x of the parent parton momentum (sea quarks) grows with Q^2, leading to the increase of the parton densities at low values of x (the gluon-gluon diagrams predominate in this region). On the contrary, at high values of x, the partons distributions are decreased because the partons with momentum x can be resolved into a parton with lower momentum $x' < x$. The scaling violations of the structure function F_2 have been used by both the HERA experiments, ZEUS and H1, to determine, through QCD fits, the gluon density $xg(x)$. The concept of partons evolution can be generalised to include higher order corrections involving more than one quark-gluon or gluon-gluon vertex. It can be shown [16] that with the choice of a gauge in which the gluons have only the two transverse polarisation states, the amplitude for the inelastic process can be obtained as the sum of ladder diagrams of consecutive gluon emissions (as sketched in Fig. 1.4). The quark which absorbs the photon evolves from the incoming proton via gluon emission thus losing, gradually, its longitudinal momentum, in other words the fractions of longitudinal momentum x_i carried by the ladder's rungs are decreasingly ordered:

$$x_1 > x_2 > ... > x_{n-1} > x_n > x, \qquad (1.20)$$

while the transverse momenta of the emitted gluons increase:

$$k_{T1}^2 \ll k_{T2}^2 \ll ... \ll k_{Tn-1}^2 \ll k_{Tn}^2 \ll Q^2. \qquad (1.21)$$

The summation of these diagrams is performed by the DGLAP equations in the leading $\log(Q^2)$ approximation where k_T^2 is strongly ordered.

8
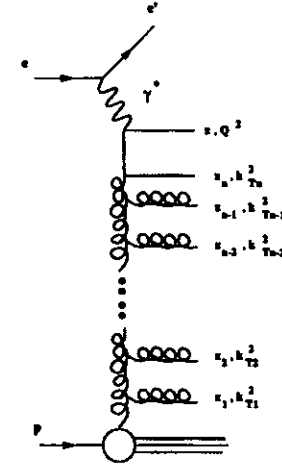
Figure 1.4: A ladder diagram. Additional diagrams originate from the substitution of some of the gluons lines with quark lines.

1.1.5 The $x - Q^2$ plane

The DGLAP equations are applicable in a region of moderate x, where:

$$\alpha_s(Q^2)lnQ^2 \sim 1, \qquad (1.22)$$

$$\alpha_s(Q^2)ln\frac{1}{x} \ll 1. \qquad (1.23)$$

At low values of x, the region of interest for HERA (as shown in Fig. 1.5), different evolution equations and approximations should be used:

• leading log $(\frac{1}{x})$ approximation:

$$\alpha_s(Q^2)lnQ^2 \ll 1, \qquad (1.24)$$

$$\alpha_s(Q^2)ln\frac{1}{x} \sim 1. \qquad (1.25)$$

At small x and moderate Q^2 the Balitsky, Fadin, Kuraev, Lipatov [15] equation (BFKL) can be used to resum the singular $\frac{1}{x}$ terms. The equation, if applicable, predicts no ordering in transverse momentum k_T and, when solved analytically, results in a gluon distribution function of the form:

$$G(x,Q^2) \equiv xg(x,Q^2) \sim x^{-\lambda}, \qquad (1.26)$$

9
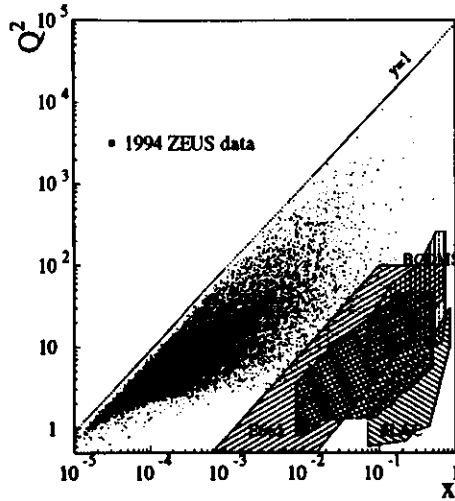
Figure 1.5: Region covered in the $x - Q^2$ plane by the published HERA data. Also shown are the regions covered by the previous fixed target experiments which show how HERA extends the kinematical region towards small x values.

with $\lambda \approx 0.5$[4]. Approaching the low x region, the scale that sets the centre of mass energy available to the process, Q^2/x, becomes large. In this context the BFKL evolution might be thought to supplement the Regge description of the high energy hadron-hadron interactions (detailed in the following sections), differing from the phenomenological approach of the latter because of the presence of the hard Q^2 scale, which validates the use of perturbative techniques.

- double log ($\frac{1}{x}, Q^2$) approximation:

$$\alpha_s(Q^2) ln Q^2 \sim 1,\tag{1.27}$$

$$\alpha_s(Q^2) ln \frac{1}{x} \sim 1.\tag{1.28}$$

Since at low x the gluon density is large, the gluons start to overlap in the proton and recombine via the QCD process $gg \rightarrow g$. This process limits the gluon density and ensures unitarity to the cross section. Gribov Levin and Ryskin [14] have added a non-linear term in the evolution equations (either DGLAP or BFKL) to describe this effect. So far the HERA

---

[4]at leading order and depending on Q^2 through $\alpha_s(Q^2)$.

data are consistent with the standard DGLAP evolution and no saturation effects on the gluon density have been observed.

1.1.6 The full expression for the cross section

The cross section for neutral current interactions results not only from the exchange of a virtual photon, but also from Z^o exchange and their interference. The inclusion of the Z^o exchange, which can be neglected at moderate Q^2, requires also the introduction of the structure function F_3. The deviation from the Callan-Gross equality, arising from the presence of the gluons, is called the longitudinal structure function F_L:

$$F_L = F_2 - 2x F_1\tag{1.29}$$

and the cross section can be written as:

$$\frac{d^2\sigma}{dx dQ^2} = \frac{2\pi\alpha^2}{2Q^4} \left[Y_+ F_2(x, Q^2) - y^2 F_L(x, Q^2) + Y_- x F_3(x, Q^2) \right] (1 + \delta_r),\tag{1.30}$$

where $Y_\pm \equiv 1 \pm (1 - y)^2$ and δ_r is the electromagnetic radiative correction vertex for the electron line.

1.2 Diffraction

The dominant mechanism for deep inelastic scattering, as discussed in the previous sections, is the scattering of the incident electron from a coloured quark which evolves, initially, into a system of partons, independently of the rest of the proton. The size of this system grows until it reaches a sizable overlap with the proton remnant and then strong correlations lead to colour neutralisation and hadronisation. The final state consists, at first order, of the scattered electron, of a jet structure (current jet) originating from the struck quark, and of the fragments of the remainder of the proton (remnant jet). Due to the colour string connection (see Fig. 1.6a) the gap in pseudorapidity[5] between the struck parton and the proton remnant is filled with particles produced in the hadronisation process. This picture does not take into
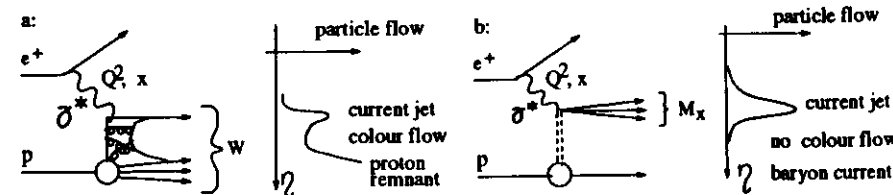
Figure 1.6: a) Deep inelastic scattering event. b) Deep inelastic peripheral scattering: diffractive dissociation of the photon on a baryon current.

account the existence of long range correlations in the proton at the beginning of the hadronisation process. These correlations arise because of colour confinement, which constrains

---

[5]The pseudorapidity η is defined as $-\ln(\tan\frac{\theta}{2})$, where θ is the polar angle.

quarks and gluons to propagate at large distances as if they were colourless hadrons. Long distance scales, which lead to peripheral scattering processes, involve small transverse momenta and small momentum transfer. These events are characterized by the presence, in the final state, of a baryon current (either a diffracted proton, or a neutron, or a resonance) as a substitute for the remnant jet. The absence of colour connection at the baryon vertex (direct consequence of the small momentum transfer) results in a gap interval between the baryon and the photon system which survives the hadronisation process (as shown in Fig. 1.6b) [a].

1.2.1 Diffraction in hadron-hadron collisions, Regge theory and the soft pomeron

Since diffractive or, more generally, peripheral processes appear to carry the signature for soft interactions (i.e. small transverse momenta), it is obvious that they had to emerge from the study of hadron-hadron collisions.

A well defined mathematical formalism, called Regge theory, was introduced in the '60s in order to explain the long range force phenomenology in t-channel exchange processes in hadron physics at high energy [18]. For scattering of hadron h and h' in the t-channel (see Fig. 1.7a) the amplitude can be calculated as the sum over the family of exchanged particles which satisfy the following condition: in the cross channel, where $\sqrt{t}$ is the centre of mass energy, all these particles lay on a straight line in the complex plane of angular momentum[7] J and mass squared $M^2 = t$ and have the same isospin I, strangeness S and baryon number B. Such lines are the so called Regge trajectories, each one of them corresponding to a family of particles which can be exchanged in a specific interaction. Experimentally it is found (Fig. 1.7b) that there are at least four families of spin-1 particles, ρ, ω, a and f, which coincide. The significance of a trajectory $J = \alpha(t)$ for a family of particles is that the scattering amplitude $A_{\lambda\lambda'}(J,t)$ has a pole in the complex plane:

$$A(J,t) \sim \frac{1}{J - \alpha(t)},\tag{1.31}$$

giving a simple high-energy behaviour to the scattering amplitude T in the t-channel, where $\sqrt{s}$ is the centre of mass energy, in the limit where all masses are small compared to s:

$$T(s,t) \sim \beta(t)s^{\alpha(t)}\zeta_\alpha(t).\tag{1.32}$$

$\beta(t)$ is the residue function of the pole which parametrises, through form factors, the couplings at the hadron vertices, and $\zeta_\alpha(t)$ is a phase factor.

Total cross section and elastic scattering

The optical theorem relates the total cross section (Fig. 1.8a) to the imaginary part of the forward elastic scattering amplitude (Fig. 1.8b) at the same s [52]:

$$\sigma(hh')_{TOT} = \frac{1}{s}ImT(s,t=0) \sim s^{\alpha(t)-1},\tag{1.33}$$

---

[a] A formal definition of diffractive processes by Bjorken [17] reads: *Diffractive processes are those that lead to large rapidity gaps in the final state phase space which are not suppressed as a function of the gap width.*

[7] More precisely, paths are traced in the complex plane by the singularities corresponding to the exchanged particles as t changes, while the linear correlation can be drawn by the considering the real part, $Re|J|$ of the angular momentum.
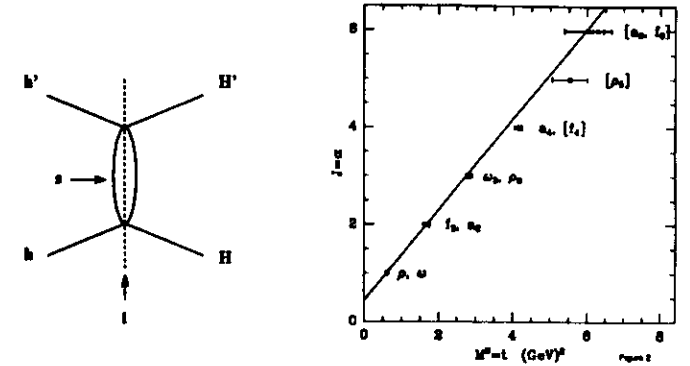
Figure 1.7: a) diagram for the scattering of hadron h on hadron h' in the t-channel at the centre of mass energy s. b) The Regge trajectories for ρ, ω, a and f on the $J - M^2$ plane.

where

$$\frac{d\sigma_{el}(hh')}{dt} \propto \frac{1}{s^2}|T(s,t)| \sim s^{2(\alpha(t)-1)}.\tag{1.34}$$

Regge theory therefore predicts the behaviour of the total and elastic cross section as a function of s through a simple power law controlled by the Regge trajectory $\alpha(t) = \alpha(0)+\alpha't$. The observation that hadronic cross sections (as shown in Fig. 1.9) are constant for a large interval of s and then slowly grow with s implies the existence of a Regge trajectory which carries no quantum numbers and has $\alpha > 1$, the so called Pomeron (IP), which dominates the amplitude for $s \to \infty$. A universal fit [19] to the σ_{TOT} hadron-hadron data as a sum of Reggeon ($R = \rho, \omega, a_2, f_2...$) and pomeron trajectories gives an excellent description[b] of all existing data with a pomeron trajectory of:

$$\alpha_{IP}(t) = \alpha_{IP}(0) + \alpha't = 1.08 + 0.25t,\tag{1.35}$$

referred to as the "soft" pomeron. A value of $\alpha_{IP}(0)$ close to unity implies that the Froissart bound, which defines the upper limit to the total cross section for $s \to \infty$,

$$\sigma_{TOT} \leq \frac{\pi}{m_\pi}\ln^2 s,\tag{1.36}$$

is not violated up to very high energies (where higher order corrections might come to restore its validity). Unitarity violations may become an issue for values of the pomeron intercept above ~ 1.3.

Moving to the analysis of the cross section dependence upon t in the framework of Regge theory, it must be noted that the differential elastic cross section $d\sigma/dt$ shows (e.g. in pp scattering data [21]), as the energy increases, a clear exponential peak at low values of t,

---

[b] The only exception being the CDF value for σ_{TOT} of 80.6 ± 2.3 mb against the predicted value of 73 mb (and the latter value is in agreement with other FNAL results).

Figure 1.8: Regge diagrams: a) Total cross section, b) Differential elastic cross section, c) Differential diffractive dissociation cross section.

followed by a secondary diffraction maximum. This is reminiscent of optical diffraction, where the intensity of the scattered light from a circular aperture as a function of angle θ (for small angles) is given by:

$$ I = I_o \left(1 - \frac{R^2}{4}(k\theta)^2 \right), \tag{1.37} $$

where k is the wave number of the photon, R is the radius of the aperture, and $\frac{\sin\theta}{\theta} \cong kR$. For pp elastic scattering:

$$ \frac{d\sigma}{dt} = \left(\frac{d\sigma}{dt}\right)_{t=0} \cdot e^{bt} \cong \left(\frac{d\sigma}{dt}\right)_{t=0} \cdot (1 - b(p\theta)^2), \tag{1.38} $$

where p is the momentum of the incoming proton.

Comparison of eqns. 1.37 and 1.38 shows that the slope parameter of the t dependence is proportional to the interaction radius R,

$$ b = \frac{R^2}{4} \tag{1.39} $$

and therefore inversely proportional to the mass of the scattering objects or systems. In the case of the interacting hadrons h and h' of masses m_h and $m_{h'}$ respectively:

$$ b \propto \frac{1}{m_h^2 + m_{h'}^2}. \tag{1.40} $$

Figure 1.9: Total pp, $\bar{p}p$, πp, and real γp cross sections with simple power fits to the s dependence.

The expression for the elastic cross section as given by Regge theory (eq. 1.34) leads to a dependence of the slope parameter b on the centre of mass energy s. By substituting in eq. 1.34 the general form for the Regge trajectory $\alpha(t) = \alpha(0) + \alpha' t$, the differential elastic cross section $d\sigma/dt$ reads:

$$ \frac{d\sigma}{dt} \propto s^{2\alpha(0)-2} e^{[2\alpha' \ln(s)]t}, \tag{1.41} $$

that is: the slope parameter b evolves with energy like $b \propto 2\alpha' \ln(s)$. This effect, called shrinkage, has been observed in hadron-hadron data and is compatible with the assumption that the exchange is driven by a soft pomeron trajectory as given by eq. 1.35.

Diffractive dissociation

The exchange of a small momentum transfer can lead to the inclusive reaction $hh' \to hX$, where a mass state M_X is produced with no exchange of quantum numbers, similarly to the

elastic case, at the target hadron's vertex[9].

The analogy with optics sets the limit beyond which the cross section for diffractive dissociation dies out: the wavelength associated with the momentum loss, $m_h \cdot \frac{M_X^2}{s}$, of the target hadron should be smaller than the interaction radius R.

For $R = \frac{1}{m_\pi}$ and in the case the target hadron is a proton:

$$1 - x_F = \zeta = \frac{M_X^2}{s} < \frac{m_\pi}{m_p} \simeq 0.15, \tag{1.42}$$

where $\zeta(x_F)$ is defined as the fractional momentum lost(carried) by the target proton.

The mass spectra of diffractively excited states of hadrons consist of some resonance-like structures superimposed on a continuum (see Fig. 5.2).

With a generalization of the optical theorem [22] to relate the total cross section for the production of the inclusive state X (Fig. 1.8c) to the forward scattering amplitude for a three body elastic scattering, the differential cross section for diffractive dissociative scattering can be calculated from the diagram on the right inside of Fig. 1.8c. For $s, M_X^2 \to \infty$ and $s \gg M_X^2 \gg t$ (triple Regge approximation) the cross section is proportional to:

$$s\frac{d^2\sigma}{dM_X^2 dt} \propto \frac{1}{s}\left(\frac{s}{M_X^2}\right)^{2\alpha(t)} \cdot (M_X^2)^{\alpha(0)}, \tag{1.43}$$

which, in the limit where only one trajectory b dominates (i.e. the pomeron IP), can be rewritten in terms of a total $h'b$ cross section (upper part of the diagram, through the optical theorem) and a flux which parametrises the emission of b from h at the lower vertex and depends only on the variables at that vertex[10], i.e. ζ and t:

$$s\frac{d^2\sigma}{dM_X^2 dt} = \frac{d^2\sigma}{d\zeta dt} \propto \zeta^{1-2\alpha(t)} F_h^2(t)\sigma_T^{h'b} \propto f_{b/h}(\zeta,t)\sigma_T^{h'b}, \tag{1.44}$$

where $F_h(t)$ is the form factor of hadron h. Although a candidate particle corresponding to the Regge pole for the pomeron trajectory has been observed near $t = 4GeV^2$ by the WA91 collaboration [20], when it is exchanged near $t = 0$ the pomeron cannot be said to be a particle. Nevertheless the factorisation 1.44 makes pomeron exchange rather similar to particle exchange.

For γp scattering at high energies, with a dominant pomeron trajectory:

$$\frac{d^2\sigma}{d\zeta dt} \propto \zeta^{1-2\alpha(t)} F_p^2(t)\sigma_T^{\gamma IP} \propto f_{IP/p}(\zeta,t)\sigma_T^{\gamma IP}. \tag{1.45}$$

Assuming a soft pomeron trajectory (eqn. 1.35) the cross section in the continuum region, at fixed t, has a $\sim 1/M_X^2$ behaviour.

---

[9]Another way of looking at inelastic hadron diffraction is through the idea of coherence. The lower the momentum transfer in the collision, the higher the probability that the target hadron h will remain intact, implying that no quantum numbers are transferred in the interaction and hadron h' is simply excited in a higher mass state X. Since hadron h does not change identity, the various amplitudes that originate at different parts of the hadron add up coherently. In this context coherence is synonym of diffraction.

[10]The factorisation of the vertices implies that the differential cross sections of a hadron dissociating on different targets scale as the elastic cross sections while those of different hadrons dissociating on the same target scale as the corresponding total cross sections. Both rules have been tested experimentally and found to hold within experimental accuracy.

Photoproduction cross sections

The whole Regge picture can be transported to the case of real photon-proton interactions, i.e. at HERA in the so called photoproduction regime ($Q^2 \approx 0$) at a centre of mass energy W, where the photon manifests hadron-like properties and, being quasi on mass-shell, justifies the use of the Regge S-matrix theory. The experimental evidence supports the hypothesis of a soft pomeron trajectory controlling the energy dependence both of the total cross section [23] (Fig. 1.9c):

$$\sigma_{TOT}^{\gamma p} = 0.0677(W^2)^{0.0808}(IP) + 0.129(W^2)^{-0.4525}(\rho,\omega,f_2,a_2)\ mb \tag{1.46}$$

and of the counterpart for the elastic hadron-hadron differential cross section, namely the elastic vector mesons production cross section [24]:

$$\frac{d\sigma_{VM}^{\gamma p}}{dt} \sim (W^2)^{2(\alpha(t)-1)}, \tag{1.47}$$

which gives, after t integration:

$$\sigma_{VM}^{\gamma p} \approx W^{0.22}. \tag{1.48}$$

Moreover, the elastic peak is observed to shrink with W accordingly to the prescription (eq. 1.41) of the theory.

1.2.2 Diffraction at larger scales

Regge theory gives a unified description of the pre-HERA diffractive data and HERA photoproduction data within a non-perturbative phenomenological approach. On the other hand, as mentioned in section 1.1.5., it is possible to apply perturbative QCD (pQCD) techniques to calculate parton dynamics in the limit $\frac{Q^2}{x} \approx W \to \infty$ and predict the asymptotic behaviour of total cross sections for high virtuality Q^2 or, in general, if either of the scales Q^2, M_X^2 and t becomes much larger than the QCD scale Λ^2. In a QCD framework the interaction proceeds through the exchange of an infinite gluon ladder (as obtained by taking the square of the amplitude in Fig. 1.4) or, at lowest order, by the exchange of a pair of gluons, a gluonic system being the only QCD treatable object to satisfy the requirement of being a colour singlet. The corresponding trajectory has a fairly large value of the intercept[11], $\alpha(0) \approx 1.5$, and it is often referred to as the "hard" pomeron trajectory.

The interesting question is, of course, whether and at which scale the Regge approach is going to break down. The most striking evidence for the possible occurrence of a new phenomenon comes from the measurement of the t-integrated cross section for elastically photoproduced J/ψ. The process presents a very clean topology from the experimental point of view and the $Q^2 \approx 0$ value sets the scale for the applicability of the Regge formalism. Nevertheless, the effective dependence on W of the J/ψ cross section [25], $\approx W^{0.8}$ (see Fig 1.10), is much steeper than the one obtained for the lighter vector mesons, which is of the type $\propto W^{0.22}$ (as indicated in eq. 1.48). The J/ψ mass scale, M_ψ^2, is much larger than the QCD scale Λ^2 and it might therefore justify the use of pQCD techniques. pQCD models exist [26] which ascribe the W dependence to the rise of the gluon density observed from the scaling violations of the proton structure function F_2.

---

[11]Energy conservation in the BFKL equation is still an open issue.
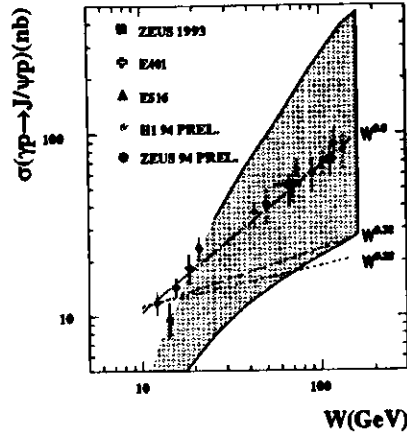
Figure 1.10: Total cross section for elastic production of J/ψ at $Q^2 \approx 0$ as a function of the $\gamma - p$ centre of mass energy W. The shaded region represents the prediction of the Ryskin model (cf. chapter 4) using the upper and lower limits of the gluon density as extracted by the ZEUS experiment.

In these models the interaction is understood to proceed through the exchange of a gluon ladder. A similar W dependence can be observed by switching from the M_X^2 to the Q^2 scale and studying the electroproduction of light vector mesons (ρ, ϕ) at high photon virtualities $Q^2 > 8 GeV^2$ [111], for which the pQCD inspired models predict a relation between the cross section and the gluon density similar to the photoproduced J/ψ's one.

The steep increase of the cross section for both the photoproduced J/ψ and the electro-produced ρ and ϕ is directly related, through the gluon density, to the small-x dependence of the structure function F_2. The low-x behaviour of F_2 maps into the high-W dependence of the total cross section for virtual photon-proton interaction $\sigma_{TOT}^{\gamma^* p}$ by virtue of the relation:

$$\sigma_{TOT}^{\gamma^* p}(W^2, Q^2) \approx \frac{4\pi^2\alpha}{Q^2} F_2(x, Q^2). \qquad (1.49)$$

The total $\gamma^* p$ cross section shows an effective W dependence which grows more steeply than the γp W dependence with increasing Q^2, as shown in Fig. 1.11, where the F_2 parametrisation based on the soft Regge formalism considerably underestimates the data. A parametrisation of the W (or x) dependence of $\sigma_{TOT}^{\gamma^* p}$ (or F_2) with a Q^2 variable power law led to the idea that there is a smooth transition region [27] between the QCD governed high Q^2 regime, characterized by a "hard" pomeron trajectory, and the hadronic domain, where the Regge "soft" approach has shown to be valid. Two pomerons are therefore needed or, alternatively, a single pomeron with a Q^2 dependent intercept [28]. The question is, of course, if the Regge pole or, equivalently, the S-matrix theory makes sense off the mass shell. No theory has explained so far how the properties of the pomeron depend on the virtualities of the external
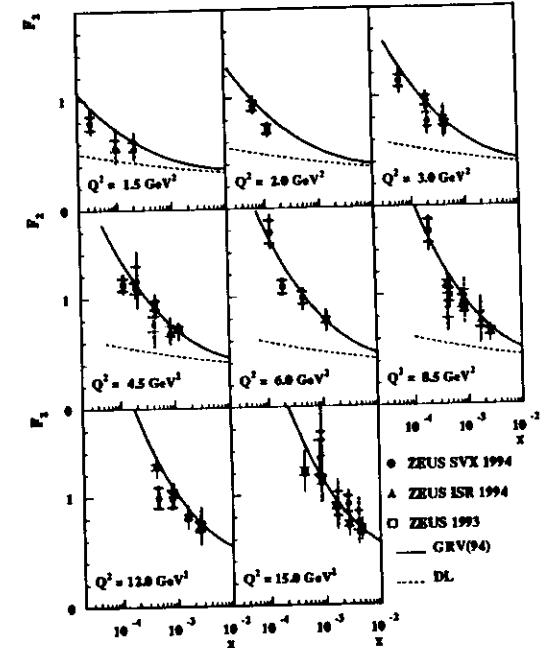
Figure 1.11: The 1994 ZEUS F_2 compared with the predictions of a soft pomeron Regge parametrisation (DL, by Donnachie and Landshoff) and the Gribov, Levin and Ryskin parametrisation.

particles. The pomeron might thus be unique and non perturbative, with a Q^2 evolution driven by the inelastic γ^* vertex [29] and scarcely reminiscent of the properties of the pomeron itself.

1.2.3 Deep inelastic diffractive dissociation, theoretical models

Whether BFKL evolution effects can be detected at HERA or not [30], the study of diffraction in deep inelastic scattering is of primary importance for sheding light on the microscopic structure of the pomeron. Although the pomeron cannot be strictly considered a particle, the use of a virtual probe with variable Q^2 can resolve the parton level structure of the interaction.

Several models have been proposed to explain diffractive interactions at high Q^2 in $e - p$ scattering. In the following a simple description of some of these models (identified with the names of the authors) is presented in conjunction with the observables most relevant to the current HERA analyses.

Definition of variables in $\gamma^* - p$ diffractive scattering

Since diffractive scattering in $\gamma^* - p$ collisions is characterized by the emission of a pomeron by the proton (Fig. 1.12), the number of variables needed to describe the interaction is larger than in standard deep inelastic $\gamma^* - p$ scattering. All variables are summarized below.

The vertex $I\!P - p$ is described by two variables: $x_{I\!P}$, the fraction of the incoming proton
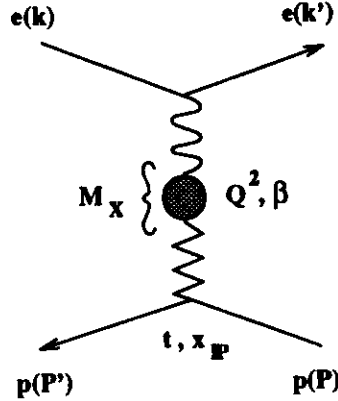
Figure 1.12: Definition of kinematics for a diffractive dissociation deep inelastic scattering event.

beam momentum carried by the pomeron, and t, the pomeron invariant mass.

$$x_{I\!P} = \frac{(P - P') \cdot q}{P \cdot q} = \frac{M_X^2 + Q^2 - t}{W^2 + Q^2 - M_p^2} \simeq \frac{M_X^2 + Q^2}{W^2 + Q^2},$$ (1.50)

$$t = (P - P')^2.$$ (1.51)

The diffracted proton is left with a fractional momentum $x_L = \frac{|p'|}{|p|}$.

The $\gamma^* - I\!P$ hard scattering can be parametrised in terms of Q^2 and β, where β is the fraction of the pomeron momentum carried by the parton which interacts with the virtual photon:

$$\beta = \frac{Q^2}{2(P - P') \cdot q} = \frac{x}{x_{I\!P}} = \frac{Q^2}{M_X^2 + Q^2 - t} \simeq \frac{Q^2}{M_X^2 + Q^2}.$$ (1.52)

For the structure of the pomeron in DIS, the variable β plays a role analogous to that of Bjorken-x for the structure of the proton.

Ingelman and Schlein (IS)

In 1985 Ingelman and Schlein proposed [55] to investigate the partonic structure of the pomeron through the reaction $p\bar{p} \to X\bar{p}$. With the assumption that the process can be decomposed in the emission of a pomeron by the proton and its subsequent hard interaction

with the antiproton, the cross section can be calculated with QCD techniques and a pomeron structure function can be defined.

The differential cross section for the process $ep \to epX$ can be written as:

$$\frac{d^5\sigma(ep \to epX)}{dx_{I\!P}dtdQ^2dp_T^2} = f_{I\!P/p}(x_{I\!P}, t)f_{g(q)/I\!P}(\beta)f_{\gamma/e}(x, Q^2)\frac{d\hat{\sigma}(\gamma g(q) \to X)}{dp_T^2},$$ (1.53)

where $f_{I\!P/p}(x_{I\!P}, t)$ is the flux factor describing the flux of pomerons in the proton:

$$f_{I\!P}(x_{I\!P}, t) = \frac{1}{2}\frac{1}{2.3 \cdot x_{I\!P}} \cdot (6.38\ e^{8t} + 0.424\ e^{3t}),$$ (1.54)

which, given the hypothesis of factorisation at the $I\!P - p$ vertex, is universal and can be extracted from hadron-hadron scattering data, $f_{\gamma/e}(x, Q^2)$ is the photon flux, $\frac{d\hat{\sigma}(\gamma g(q) \to X)}{dp_T^2}$ is the matrix element for the hard scattering (the dominant process being $\gamma^* g \to q\bar{q}$, with the production of high p_T jets in the final state) and $f_{g(q)/I\!P}$ represent the parton densities inside the pomeron, which, as a consequence of factorisation, are independent of the process of emission. Given its quasi-hadronic nature, the pomeron is treated as a particle and a structure function can be defined as:

$$F^{I\!P}(\beta, Q^2) = \sum_i e_i^2[\beta q_i(\beta) + \beta\bar{q}_i(\beta)].$$ (1.55)

The normalisation of the parton densities is determined by the fulfillment of the momentum sum rule (as given in eq. 1.13).

Donnachie and Landshoff (DL)

In the Donnachie-Landshoff [54] (DL) model diffraction in DIS is described through pomeron exchange between the virtual photon and the proton, with the pomeron coupling predominantly to quarks, in analogy with the photon. The authors calculate the cross section in the framework of Regge theory:

$$\frac{d^2\sigma}{dtd\beta} = f_{I\!P}(x_{I\!P}, t) \cdot F_{q/I\!P}(\beta, Q^2).$$ (1.56)

The flux factor,

$$f_{I\!P}(x_{I\!P}, t) = \frac{9\beta_0^2}{4\pi^2}F_1(t)^2 x_{I\!P}^{1-2\alpha(t)},$$ (1.57)

is related to the elastic form factor of the proton, $F_1(t) = \frac{4M^2 - 2.8t}{4M^2 - t}(\frac{1}{1 - t/0.7})^2$, and to the pomeron-quark coupling, $\beta_0 \simeq 1.8\ \text{GeV}^{-1}$, extracted from hadron-hadron data. The pomeron trajectory is the "soft" one, i.e. $\alpha(t) = 1.08 + 0.25t$. The similarity between the pomeron and the photon leads to a quark structure function $F_{q/I\!P}$ of the form:

$$F_{q/I\!P} = \frac{1}{3}C\pi\beta(1 - \beta),$$ (1.58)

with $C \approx 0.25$ for each light quark and antiquark. Just as for the case of the photon structure function, a term that is important at low β must be added, in the form $\beta^{-\epsilon_o}$ (with $\epsilon_o \approx 0.08$ or larger). No prediction is made for the pomeron's gluon structure function; as the pomeron is not a particle, there is no momentum sum rule.

Nikolaev and Zakharov (NZ)

The diffractive interaction is viewed [63] as photon diffractive dissociation on a proton. The photon fluctuates in different hadronic states with a wave function which can be expressed as:

$$|\gamma> = |\gamma>_{bare} + |q\bar{q}> + |q\bar{q}g> + ... \qquad (1.59)$$

The cross section is proportional to the transverse size ρ of these fluctuations ("colour transparency"):

$$\sigma(\rho) \propto \alpha^2\rho^2, \qquad (1.60)$$

which, for $q\bar{q}$ fluctuations, leads to one of the strongest predictions of the model; since $\rho \propto \frac{1}{m_f}$ (where m_f is the mass of the quark of flavour f):

$$\sigma \propto \frac{1}{m_f^2}, \qquad (1.61)$$

i.e. the production of heavy quarks is strongly suppressed.

The interaction with the proton proceeds through the exchange of two gluons (see Fig. 1.13) and the idea of pomeron flux and structure function is not used.

The cross section assigned to the $q\bar{q}$ fluctuations, the valence component of the exchange
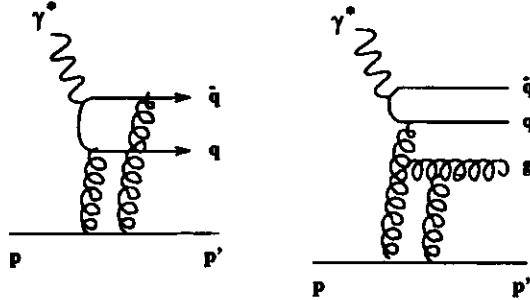
Figure 1.13: Diagrams for the production of $q\bar{q}$ and $q\bar{q}g$ states in the NZ diffractive model.

(dominant at $M_X^2 < Q^2$), is given by:

$$\frac{d^2\sigma}{dt dM_X^2}|_{t=0} \propto \frac{M^2}{(Q^2+M^2)^3}, \qquad (1.62)$$

while the cross section corresponding to the $q\bar{q}g$ fluctuations, sea component (dominant for $M_X^2 \gg Q^2$), is given, in the triple Regge approach, by:

$$\frac{d^2\sigma}{dt dM_X^2}|_{t=0} \approx \frac{\sigma_{TOT}(\gamma^*p)A_{3IP}}{M_X^2}, \qquad (1.63)$$

where A_{3IP} is the triple pomeron coupling. Although the pomeron in this model is not treated as a particle with a well defined partonic structure, it is possible to give an operational definition of the cross section in terms of a two component (valence and sea) diffractive structure function. The splitting of the structure function emphasizes the breaking of factorisation predicted by the model. The x_{IP} and β dependence can be factorised for each of the two components separately with the following global result for the cross section:

$$x_{IP}\frac{d\sigma}{dt dx_{IP}}|_{t=0} = \frac{\sigma_{TOT}(pp)}{16\pi B_{3IP}}\frac{4\pi^2\alpha}{Q^2}\cdot\left[\frac{B_{3IP}}{B_{el}}\phi_{IP}(x_{IP})F_{val}^{IP}(\beta,Q^2) + f_{IP}(x_{IP})F_{sea}^{IP}(\beta,Q^2)\right], \qquad (1.64)$$

with the factor $\frac{B_{3IP}}{B_{el}}$ arising from the limit $t \to 0$ of the t-dependent part of the flux factors: $\phi_{IP}(x_{IP})exp(-B_{el}|t|)$ and $f_{IP}(x_{IP})exp(-B_{3IP}|t|)$ [12]. The x_{IP} dependence is well reproduced by the formula:

$$f_{IP}(x_{IP}), \phi_{IP}(x_{IP}) = \left(\frac{x_{IP}^o}{x_{IP}}\right)^{p_1}\left(\frac{x_{IP}+p_3}{x_{IP}^o+p_3}\right). \qquad (1.65)$$

The values of the parameters p_1, p_2 and p_3 can be found in [64]. The valence $q\bar{q}$ and sea $q\bar{q}g$ structure functions are defined as:

$$F_{val}^{IP}(\beta,Q^2) = 0.27\beta(1-\beta), \qquad (1.66)$$

$$F_{sea}^{IP}(\beta,Q^2) = 0.063(1-\beta)^2. \qquad (1.67)$$

Partonic models of diffraction, Buchmüller and Hebecker

A non-IP model has been developed by Buchmüller and Hebecker [31] to picture diffractive interactions in DIS in terms of γ^*-gluon scattering. The rapidity gap in the final state is restored through a colour reorientation of the produced quark-antiquark pair in the colour field of the proton. The probability of obtaining a colour singlet or octet configuration are simply $\frac{1}{9}$ and $\frac{8}{9}$, respectively. This leads to the prediction that diffraction should account for 1/9 of the proton structure function. A simple scaling law, which relates the diffractive to the proton structure function, is predicted in the form:

$$\langle F_2^{D(3)}(\beta,Q^2,x_{IP}=\zeta)|_{Q^2} = 0.04F_2(x=\zeta,Q^2)|_{Q^2}. \qquad (1.68)$$

---

[12] The excitation of the $q\bar{q}$ valence is the counterpart of diffraction production of resonances in hadronic scattering and/or real photoproduction when it is appropriate to use the diffraction slope of elastic πN scattering $B_{el} \approx 12 GeV^{-2}$, whereas excitation of the sea is the counterpart of the triple-pomeron regime with $B_{3IP} \sim \frac{1}{2}B_{el}$.

Chapter 2

HERA and ZEUS

The chapter briefly describes the HERA collider and the ZEUS detector, focusing on the detector components most relevant to the present analysis. A description of the ZEUS trigger architecture is given at the end of the chapter.

2.1 Hadron Elektron Ring Anlage, HERA

HERA is the world's first lepton proton collider, designed to have a centre of mass energy $\sqrt{s} = 314GeV$, an order of magnitude higher than the fixed target experiments which preceded it. To reach an equivalent centre of mass energy using a fixed target would require a lepton beam of $52TeV$. HERA was commissioned in 1991 and the first ep interactions were observed in H1 and ZEUS during spring 1992.

Five data taking periods have taken place since then: July 1992, September-October 1992, May-November 1993, 1994, and 1995. The 1996 running period is ongoing. During 1994 HERA switched from electron to positrons resulting in a greatly improved beam lifetime. It is foreseen that the machine will return to circulating electrons in 1997. The energy of the proton beam was kept at $820GeV$ and that of the electron beam at $26.7GeV$ during 1992 and 1993 periods, raised to $27.5GeV$ since 1994 onwards.

HERA is located in Hamburg, across the DESY laboratory site. An underground tunnel of $6.34Km$ circumference houses two separate rings for electrons and protons. The beams are brought into collision at zero crossing angle at four interaction points around the ring [1]. The two main experiments, H1 and ZEUS, are located in large underground halls at the north and south interaction points, respectively. The remaining two halls have been allocated in a second time to the HERMES and HERA-B experiments.

Fig. 2.1 shows the layout of the HERA accelerator complex. Protons from a H^+ source emerge from a LINAC at the energy of $50MeV$, then are accelerated to $7.5GeV$ in the DESY III Proton Synchrotron and transferred to PETRA, where 70 bunches are accelerated to an energy of $40GeV$ before being injected in the main HERA ring. LINAC I and II accelerate electrons and positrons to 220 and $450GeV$ respectively, which are then transferred to DESY II for further acceleration up to $7.5GeV$. They are finally injected into the HERA electron ring at $14GeV$ from PETRA.

---

[1]The necessary bending magnets produce strong synchrotron radiation close to the experimental area. Absorbers and collimators are placed at both ends of the experiments.
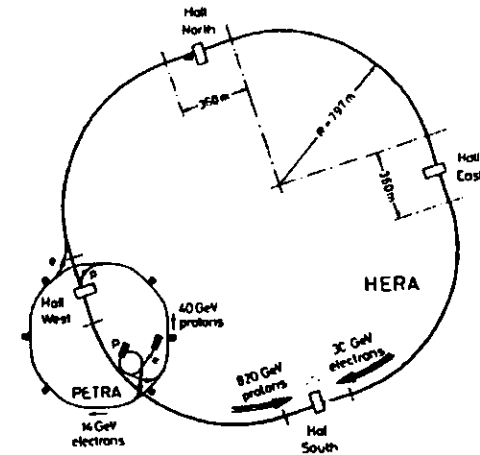
Figure 2.1: Overview of HERA, details in the main text

The proton ring employs $4.68T$ superconducting magnets in the curved sections while conventional magnets are in use for the electron ring.

During the 1993(1994) data taking period, 84(153) bunches were filled for each beam, and in addition 10(15) electron and 6(17) proton bunches were left unpaired for background studies.

The design parameters and the performance of the HERA machine during the 1994 data taking period are summarised in Table 2.1.

2.2 ZEUS

The construction and installation of the ZEUS detector in the HERA south hall was completed by autumn 1991. Since then, several detector upgrades took place as a consequence of the physics and technical understanding gained by the collaboration during the first years of data taking.

The coordinate system of ZEUS is defined as a right-handed system with the origin at the nominal interaction point (IP), and the z-axis pointing to the outgoing proton direction (defined as the forward direction). In this frame, the y-axis points upwards and the x-axis towards the centre of the HERA ring. Thus, the proton beam polar angle is $0°$, whereas the electron beam polar angle is $180°$.

Longitudinal and transverse (with respect to the beam direction) layouts of ZEUS are given in Fig. 2.2 and Fig. 2.3, respectively. The detector dimensions are $11.6m \times 10.8m \times 10m(x, y, z)$ and the total weight is 3600 tonns.

Radially outward from the interaction point are the beampipe, the vertex detector (Vertex

HERA parameters	Design values		1994	
	electron	protons	positrons	protons
Energy (GeV)	30	820	27.5	820
Instantenous luminosity (cm^{-2}s-1)	1.7 · 10^{31}		2.3·10^{30}	
Specific luminosity (cm^{-2}s^{-1}mA^{-2})	3.9 · 10^{29}		3.4·10^{29}	
Integrated luminosity (pb)	-		6.0	
Circumference (m)	6336		-	
Magnetic field (T)	0.165	4.65		-
Injection energy (GeV)	14	40	-	
Current(mA)	58	163	28	38
Number of bunches	210		153+15	153+17
Bunch crossing time (ns)	96		96	
Beam σ_x (mm) at IP	0.30	0.27	0.27	0.18
Beam σ_y (mm) at IP	0.06	0.09	0.06	0.06
Beam σ_z (cm) at IP	0.8	11	0.8	11
β (horizontal)	2	10	2	7
β (vertical)	0.9	1	0.9	0.7
Injection time (min.)	15	20	45	60
Efficiency	33%		-	

Table 2.1: HERA design parameters and performance during 1994 running.

Detector VXD), and a central drift chamber for charged particles (Central Tracking Detector, CTD). The CTD is surrounded by a superconducting magnet providing a field of 1.43T. Forward and rear tracking chambers (FTD and RTD) provide extra tracking information and particle identification in the forward and rear direction. The tracking chambers are surrounded by a high resolution Uranium Calorimeter (UCAL). The UCAL is divided in three sections: the FCAL in the forward direction, the RCAL in the rear direction, and the BCAL, a barrel section surrounding the central region. A small angle tracking detector (SRTD) is situated behind the RTD and covers the face of UCAL to a radius of ~ 34cm around the centre of the rear beampipe hole. The UCAL is enclosed by muon identification chambers (FMUI, BMUI, RMUI) situated in the inner side of the iron yoke, The yoke serves as absorber for the backing calorimeter (BAC, used to measure the energy of late-showering particles), and as a return path for the solenoid magnetic field. On the other side of the yoke, the outer muon chambers are installed (FMUO, BMUO, RMUO). Downstream of the main detector an iron/scintillator VETOWALL is used in order to reject beam-related backgrounds. The C5 beam monitor, a small led-scintillator counter, located around the beam pipe at $z = -3.15m$, monitors the syncrotron radiation accompanying the beams and the timing and longitudinal structure of the proton and electron bunches. Outside the picture limits are the luminosity monitor (LUMI), in the rear direction, the leading proton spectrometer (LPS) and the forward neutron calorimeter (FNC) in the forward direction.

The very short time interval (96ns) between the bunch crossing at HERA results in a nominal rate of 10MHz. In order to reduce the rate to a few Hz level, ZEUS employes a three-levels triggering system.

Given the complexity and variety of the HERA physics program, the detector components have to meet a series of design requisites. In particular, the calorimetry is required to be hermetic, both for the measurement of leptons and jets, have high energy and angular resolution,

Overview of the ZEUS Detector
(cross section)
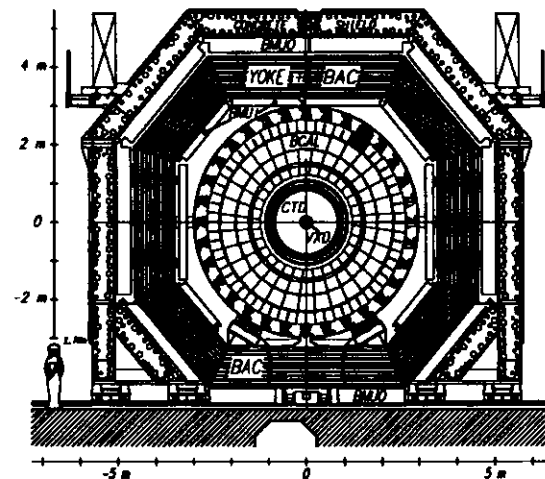
Figure 2.2: Cut of ZEUS along the beam direction

nearly equal response to electromagnetic and hadronic showers, and calibration uniformity and precision. The tracking detectors have to provide a precise vertex measurement, high momentum resolution, good tracks separation and a wide angular coverage.

The parts of the detector essential for the present analysis are described in more detail in the following sections. A more general and complete description can be found in [44].

2.2.1 The central tracking detector (CTD)

The inner tracking detectors provide charged particle detection in the angular range 7.5° ≤ θ ≤ 170°. As well as giving precision momentum, position measurement and primary vertex information, they are also designed to provide particle identification using dE/dx information and transition radiation, to reconstruct secondary vertices from short lived particles and to provide information to the ZEUS trigger system.

The cylindrical central tracking detector (CTD) covers the polar region 15° < θ < 164° and consists of 72 cylindrical drift chamber layers, organised into 9 superlayers [32]. The odd superlayers are axial layers which have sense wires parallel to the beam axis, whilst the even superlayers are stereo layers inclined at angles ≃ 5° to the beam axis, which allow the determination of the z-position.

The design and the 1993-1994 achieved resolutions in transverse momentum are 0.0021 p_T⊕ 0.0029 and 0.005 p_T ⊕ 0.0016, respectively.
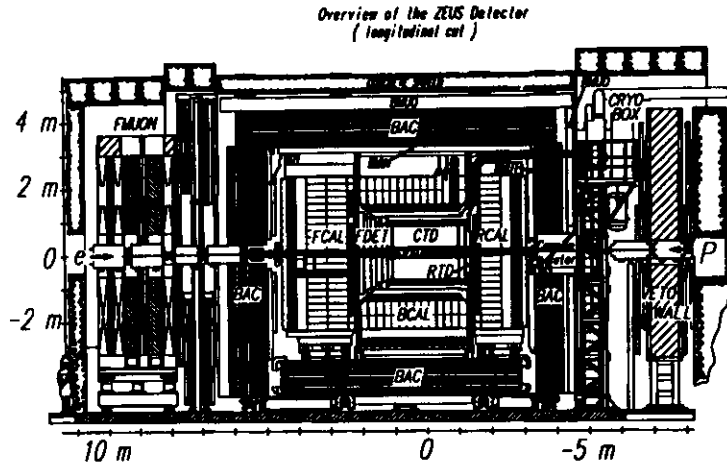
Figure 2.3: Cut of ZEUS perpendicular to the beam direction

Using the combined information of the CTD and the VXD, resolutions of 0.4 cm in z and 0.1 cm in radius in the xy plane were obtained for the primary vertex reconstruction for both 1993 and 1994 data.

2.2.2 The small angle rear tracking detector (SRTD)

For a precise measurement of the scattered electron energy and angle, for low Q^2 events in low-x DIS, additional tracking is needed to improve the calorimeter reconstruction in regions close to the rear beam pipe hole and to correct for energy losses due to the presence of inactive material in that specific region (VXD cables, flanges, etc.).

The Small angle Rear Tracking Detector or SRTD is a scintillator strip detector of dimensions 68 cm ×68 cm around the inner RCAL beampipe hole [33].

Fig 2.4 shows a schematic of the detector layout. Charged particles are detected by two planes of orthogonally arranged (x, y) strips with a 1 cm pitch which provide position and pulse height information via a photomultiplier readout. Each plane is divided into four quadrants as shown in the figure.

SRTD hit information is used in conjunction with that from the CTD for track reconstruction. The SRTD is also used to reject background by providing a fast timing measurement to the trigger, complementing the rejection provided by the C5 and VETOWALL counters at the first level trigger and the calorimeter at higher trigger levels.
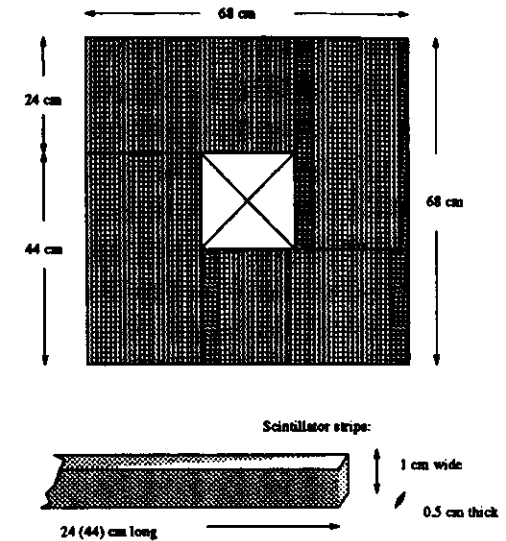
Figure 2.4: A schematic of the SRTD showing the orientation of the scintillator strips in the two orthogonal planes. The dimensions of the detector and a typical strip are also shown. The beampipe is accommodated in the central hole.

2.2.3 The uranium calorimeter (UCAL)

The ZEUS calorimeter is a high resolution uranium-scintillator compensating calorimeter. It consists of alternating layers of depleted[2] uranium (thick one radiation length corresponding to 3.3 mm), as absorber, and scintillator (2.6 mm thick), for readout purposes. The use of uranium helps to increase the response to hadrons. The ratio of scintillator thickness to absorber thickness has been chosen so that the calorimeter has an equal response to electrons and hadrons ($e/h = 1$), and a high energy resolution for hadrons and jets. The measured energy resolution of the ZEUS calorimeter is

$$\frac{\sigma(E)}{E} = \frac{35\%}{\sqrt{(E)}} \oplus 2\%,$$

for hadrons, and

$$\frac{\sigma(E)}{E} = \frac{18\%}{\sqrt{(E)}} \oplus 1\%,$$

for electrons. The calorimeter calibration is determined and maintained on a channel-by-channel basis using one among the observed uranium decay chains, i.e $U^{238} \rightarrow U^{234}$, which

---

[2]An alloy of 98.4% U^{238}, 1.4% Nb, and less than 0.2% U^{235}.

28

29

releases β particles with a maximum energy of $2.3 MeV$. A ^{60}Co source is also used.

The layout of the calorimeter is shown in fig. 2.5. It consists of three parts covering different regions of pseudorapidity $\eta = -ln(tan\theta/2)$:

- the forward calorimeter (FCAL), covering the forward region $1.1 \leq \eta \leq 4.3$,

- the barrel calorimeter (BCAL), covering the central region $-0.75 \leq \eta \leq 1.1$,

- the rear calorimeter (RCAL), covering the backward region $-3.8 \leq \eta \leq -0.75$.

With the exception of holes of 20×20 cm^2, in the center of FCAL and RCAL, which are necessary to accomodate the HERA beampipe, the calorimeter is $> 99.7\%$ of 4π hermetic.
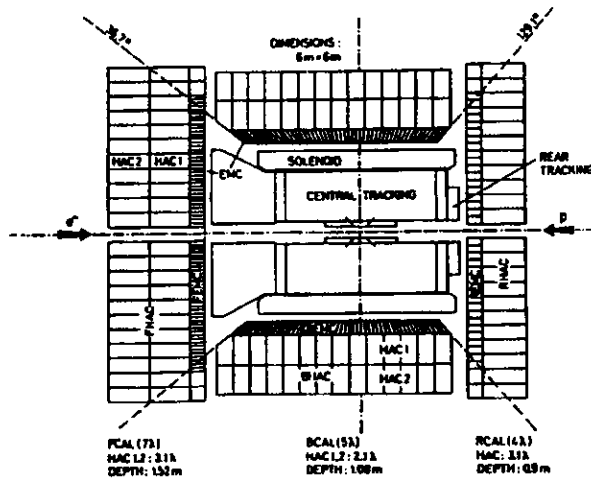
Figure 2.5: Side view of the ZEUS calorimeter.

The structure of the three calorimeter parts is similar. They are subdivided longitudinally into modules, which in turn are subdivided into towers of approximate transverse dimensions 20×20 cm^2.

Each tower is segmented longitudinally into an electromagnetic (EMC) and one (in RCAL) or two (in FCAL and BCAL) hadronic (HAC1,2) sections. The EMC sections consist of four 5×20 cm^2 cells in FCAL and BCAL, and two 10×20 cm^2 cells in RCAL. The HAC sections are cells on their own.

Each calorimeter cell is read out on two opposite sides by two photomultiplier tubes (PMTs) coupled to the scintillator through wavelength shifters, in order to achieve a more accurate position measurement within the cell. The EMC section has a depth of approximately 25 radiation lengths (X_o), or 1 absorption length (λ). The total HAC sections in

FCAL/BCAL/RCAL are 6λ, 4λ and 3λ deep, respectively. Very good containment of EM showers is therefore expected. Hadron-electron separation is achieved by the measurement of shower profiles, and in the RCAL is enhanced by additional silicon diode detectors: the hadron-electron separator (HES).

The calorimeter also provides accurate timing information with a time resolution better than 1 ns for energy deposits greater than 4.5 GeV. The total time of a calorimeter section (F/B/RCAL) is obtained from an energy weighted average of the times of all PMTs with energy deposits greater than 200 MeV.

2.2.4 The luminosity monitor (LUMI)

The ep luminosity is measured by the luminosity monitor using the rate of hard bremsstrahlung photons from the Bethe-Heitler process[3]:

$$ep \to e'p\gamma.$$

The cross section for this process is high and well known from theoretical calculations up to 0.1%. Two lead scintillators (see Fig 2.6) are used to measure both the scattered electron and the radiated photon: bremsstrahlung photons emerging from the electron-proton interaction
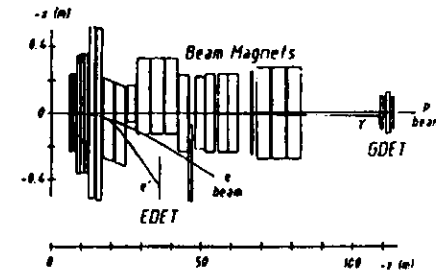
Figure 2.6: The two LUMI calorimeters.

point (IP) at angles $\theta_\gamma \leq 0.5 mrad$ with respect to the electron beam axis hit the photon calorimeter at 107 meters from the IP and electrons emitted at scattering angles $\leq 6 mrad$ and with energies $0.2E_e < E'_e < 0.9$ are deflected by beam magnets and hit the electron calorimeter placed at 35 meters from the IP.

2.3 The ZEUS trigger system

ZEUS uses a sophisticated trigger and read-out system, to enable operation with the very short beam crossing interval of HERA (96 ns). The rate of ep physics events in the ZEUS

---

[3]Since 1993 only the rate of hard photons with $E_\gamma > 5GeV$ is used for the measurement.

detector is of the order of a few Hz. However, the background from interactions of the proton beam with residual gas in the beampipe has a much higher rate, of the order of 100 kHz, which has to be reduced by the trigger system. In addition, background events from electron beam-gas interactions, beam halo, and cosmic rays, have to be rejected. The trigger system is organized in three levels.

The First Level Trigger (FLT) system is a hardware trigger, designed to reduce the input rate below 1 kHz. Each detector component has its own FLT, which stores the data in a pipeline, and makes a trigger decision within 2 μs after the bunch crossing. The decisions from the local FLTs are passed to the Global First Level Trigger (GFLT), which decides whether to accept or reject the event, and returns this decision to the component readout within 5 μs.

If the event is accepted, the data are transferred to the Second Level Trigger (SLT), which is software-based and runs on a network of Transputers. It is designed to reduce the rate below 100 Hz, using mainly timing cuts. Each component can also have its own SLT, which passes a trigger decision to the Global Second Level Trigger (GSLT). The GSLT then decides on accepting or rejecting the event.

If the event is accepted by the GSLT, all detector components send their data to the Event Builder (EVB), which produces an event structure on which the Third Level Trigger (TLT) code runs. The TLT is also software-based, runs on a farm of Silicon Graphics CPU's, and is designed to reduce the rate to a few Hz.

Events accepted by the TLT are written to tape.

Chapter 3

The Leading Proton Spectrometer

3.1 Spectrometer characteristics

The Leading Proton Spectrometer (LPS) is a component [44] of ZEUS designed to reconstruct small angle ($\sim$ 1 mrad) scattered protons which would otherwise escape undetected inside the beam pipe. It consists of six stations of position sensitive μ-strip silicon detectors placed along the proton beam line at a distance varying between 20 and 90 meters from the interaction point. The detector assemblies in each station are mounted on a moving arm, which allows them to be positioned near the proton beam. The spectrometer makes use of the beam elements of the proton ring in order to give a high resolution estimate of the momentum of the reconstructed track. A simplified diagram of the spectrometer optics is given in Fig 3.1, where all the elements and drift spaces in the beam have been grouped in order to show the main optical functions. The first three stations of the spectrometer (S1, S2, S3) can be
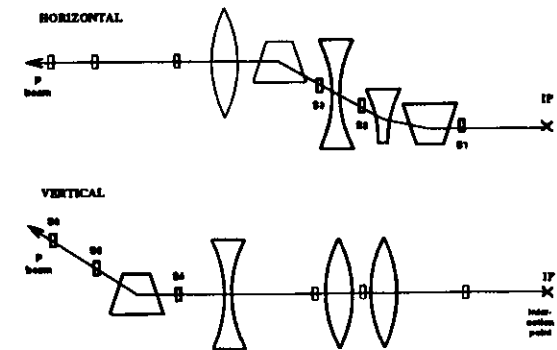
Figure 3.1: Simplified diagram of the HERA proton beam optics relevant for the LPS. The top view (above) shows the magnetic elements relevant to the S1, S2 and S3 spectrometer as thick lines. The side view (below) shows the magnetic elements relevant to the S4, S5 and S6 spectrometer as thick lines.

used independently from the second three (S4, S5, S6), having a small region of overlap in acceptance. In order to measure the momentum of the forward proton, S1, S2, and S3 use the combined horizontal bending of a septum magnet and three quadrupoles, while S4, S5, and S6 exploit the upward deflection of three dipole magnets. Each of the stations S1, S2, and S3 approach the beam horizontally from one side only; S4, S5, and S6 consist of two halves (up and down) which are lowered vertically inside the beam and partially overlap in the position of data taking, to fully enclose the beam profile. The six stations together give
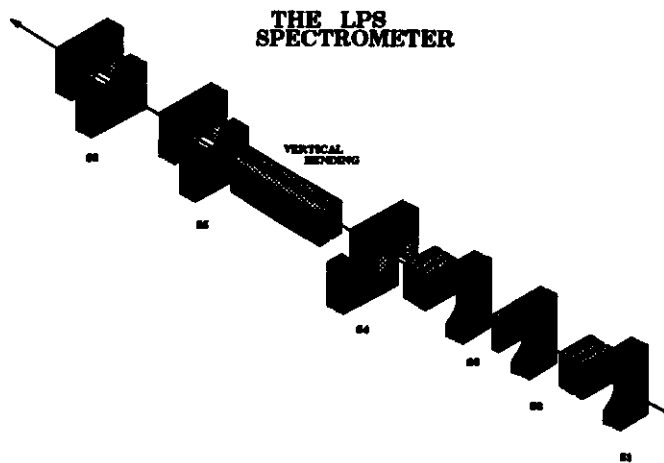
Figure 3.2: Scheme of the LPS detectors assemblies. The small trapezoidal areas in $S4up \rightarrow S6up$ correspond to the trigger detectors.

an almost complete coverage of the phase space between the 10 standard deviations profile of the beam and the magnets apertures. Costs and availability of space between the beam elements limit the number of stations to six.

Each station is equipped with six planes of DC-coupled, single sided μ-strip silicon detectors placed parallel to each other (at a distance of $\sim 6mm$ from each other) with three different strip orientations, chosen to achieve redundancy and remove reconstruction ambiguities: $\pm 45°$ (U and V) and $0°$ (Y) with respect to the vertical axis [1]. The detectors pitch is $115\mu m$ for the Y views and $115/\sqrt{2}\mu m$ for the U and V views, the number of strips per detector ranges from 448 to 1024. The shape of the detectors is rectangular (dimensions of the order of $40 \times 60 cm^2$, varying from one station to the other) with an elliptical cut-out along one edge (see Fig. 3.2) which follows at 10σ the profile of the beam at each station, according to the beam optics.

Smaller planes ($2cm^2$ area) of detectors are installed in $S4up$, $S5up$ and $S6up$ to trigger

[1]The vertical axis coincides with the direction of strongest magnetic deflection, given by the dipole magnets BU in between $S4$ and $S5$.

high x_L elastic and diffractive events. These detectors are AC coupled, single sided and have a larger pitch ($\sim 750\mu m$). Although installed during the 1994 data taking, the trigger planes became fully operational only in 1995. A partial read-out of the trigger rates was made available in order to enable the LPS alarm system to trigger a fast ejection of the detectors in case of high rates. A more detailed description of the trigger can be found in [34].

3.2 Mechanics

In order to access the inner part of the beam pipe without affecting the vacuum conditions, the detectors are inserted in the beam line by means of "roman pots". The pots are recipients made of stainless steel with an open end into which the detector planes can be moved, $3mm$ thick walls and thinner windows ($\approx 380\mu m$) in front of the detectors, perpendicularly to the beam direction.

The bottom of the pots is shaped, like the detectors, with an elliptical profile. Bellows connect the pots to the vacuum system, providing adequate vacuum tightness and allowing the movement of the pots inside the beam pipe (see Fig. 3.3). Inside the pots the detectors are operated at atmospheric pressure and room temperature. Each pot is fluxed with nitrogen in order to keep humidity at low levels.

High radiation levels in proximity to the beam pipe require the pots to be extracted during the filling operations of the machine. Remotely controlled motors drive the detectors, from a safe position of $\sim 50cm$ from the beam pipe, inside the pots, at the edge of the vacuum chamber. A second movement brings the pots and the detectors inside the pipe, at a lower speed. This movement can be performed only with stable beam conditions, i.e. when the proton beam collimators are closed. The moving mechanism and the position monitoring have been realised with a great care because the detectors, once extracted, have to be repositioned with a precision of $\sim 25\mu m$. An automatic procedure can be called to perform all the movements, monitoring the beam position, the rates on the proton collimators, background counters and LPS trigger planes.

Extraction with colliding beams occurs whenever triggered by an alarm system based on the requirement that the position of the beam, as detected by two beam position pick up monitors (located at 45 and 61 meters from the interaction point) does not exceed a window of $\pm 2.5mm$ within a run.

Each pot can also be moved transversely to the beam direction in order to allow careful centering of the detectors with respect to the beam axis.

The vacuum force which acts on the pots can be as large as $8KN$ and is compensated with a nitrogen pneumatic system in $S5$ and $S6$ and with mechanical constant tension springs in $S1, S2, S3$ and $S4$.

The movements are carried out by stepping motors (each pulse sent to the motor corresponding to a fixed angle of the screw which drives the detectors movement) with the exception of $S5$ and $S6$ which make use of DC motors. The position measurement is performed through resolvers which measure the revolving angles of the stepping motors ($\approx 5\mu m$ accuracy) and linear transducers ($\approx 20\mu m$ accuracy). In the eventuality of a power failure, two emergency power supply units (UPS) provide the motors with the power necessary to extract the pots. Two endstop switches prevent each detectors assembly to go outside the permitted range; in addition an intermediate precision switch is used to calibrate the system

z-y view   x-y view
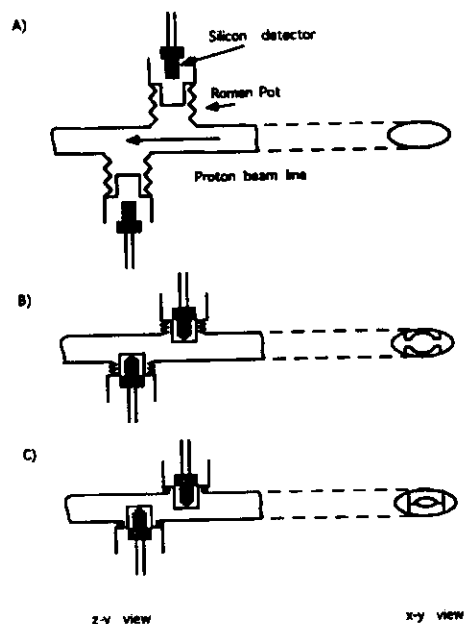
Figure 3.3: Schematic layout of a station (S4, S5 or S6). A) During filling and ramping, the detector planes are kept outside of the pots and the pots are placed far from the beam. The zig-zag lines indicate the bellows. B) The detector planes are inside the pots and the pots are being moved towards the beam. Note the elliptical profile of the fronts of the pots (x-y view), which matches the cut-out of the detector planes. C) When taking data, the pots are fully inserted and the detector planes in the upper and lower half of the station partially overlap in the transverse plane. This is the data taking configuration.

within $10\mu m$ accuracy.

3.3 Design and test of the silicon detectors

The detectors consist of p-type strips on n-type implant. The strips are DC coupled to the amplifier inputs and a positive bias voltage is applied, through the hybrid support (described in section 3.6), to the backplane of the detector. A grounded guard ring surrounds the strips in order to avoid large surface currents. The inactive region between the guard ring and the edge of the detector is of the order of $750\mu m$.

The detectors were built by three different manufacturers and the elliptical cut-out was realised with different techniques at the three locations: milling machine, diamond saw and laser. While the last two techniques showed results of similar quality, the first one caused, in several cases, sizable defects and cracks which affected the performance of the whole detector plane.

Tests were performed on each detector before the assembly [35], including the measurement of:

- leakage current per strip,
- bulk capacitance as a function of bias voltage,
- interstrip capacitance and resistance.

The leakage current is typically less than $\sim 10nA$ per strip in the depletion region of the detector (varying between 40 and 80 Volts). On some of the detectors breakdown effects in the current were observed to occur at bias voltages close to the depletion voltage as a consequence of the poor quality of the cut-out edges. Detectors with more than ten strips with leakage current $> 100nA$ at depletion voltage were discarded at assembly stage and the total current per detector was constantly monitored during data taking.

The total strip capacitance, as given by the sum of the capacitance strip to backplane (bulk capacitance) and of the interstrip capacitance (given at good approximation by the contribution of the first and second neighbouring strips), is of the order of[2] $\sim 2pF/cm$. The stability of the capacitance under irradiation was checked up to γ ray doses of 5 Mrad (^{60}Co) and proton fluences of $10^{14}p/cm^2$ with an increase in the interstrip capacitance up to $\sim 50\%$ [42].

3.4 Design of the frontend electronics (FEE)

The design and the choice of technology for the LPS front-end electronics [36] was based on a set of specifications following from the HERA machine and the ZEUS read-out and trigger environment:

- **Radiation hardness.** The electronics is located close to the silicon detectors and therefore operates in proximity to the beam, having to withstand proton fluences up to $10^{14}p/cm^2$.

- **Fast amplifier shaping time** commensurate with the collection time of the holes of a fully depleted detector. A shaping time of $\sim 30ns$ ensures also that the signal peaking time is less than the HERA bunch crossing time ($96ns$), which allows the correct assignment of the bunch crossing number to the detector's signal.

- **Narrow channel width** to match the smallest detectors pitch ($115/\sqrt{2} \approx 80\mu m$ for the $0°$ planes). The chips bonding pads had to be arranged, as well as the detectors ones, on a double row.

- **Low noise** to ensure good signal-to-noise ratio. With a signal charge of 25000 electron-hole pairs per minimum ionizing particle, a noise charge of about 1000 electrons gives good detection efficiency with low noise rate. The load capacitance varies between 1pF and 11pF depending on the strip length.

---

[2]For a $0°$ detector the coupling between strips was estimated to be $\sim 1.5pF$ and the coupling between a strip and the backplane $\sim 1.2pF$.

- **Low power consumption** to minimize temperature increase. An upper limit of 2mW/channel was required.

- **Operation with high input currents.** Since the detector is directly coupled to the amplifier, the anticipated radiation damage to the detector will result in high leakage currents (up to $2\mu A$ per strip) which the amplifier inputs have to absorb without loss of gain.

- **Pipelined operation** in order to comply with the ZEUS trigger architecture: the data can be stored on chip until a valid second level trigger arrives after about 2ms. This is achieved by a synchronous first level buffer $6\mu s$ deep followed by an asynchronous second level buffer.

Based on the above requirements, the combination of a bipolar amplifier-comparator VLSI chip and a CMOS digital pipeline chip (see Fig. 3.4) was selected. The number of channels
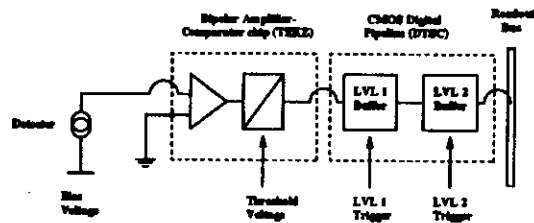
Figure 3.4: Block diagram of the front end electronics system

per chip is 64. Wire bonds connect the analog chip to the detector and the analog to the digital chip. The system is binary, i.e., for every channel a bit is stored in the time slice of the corresponding beam crossing, which is set if the pulse height exceeds a threshold value and is set to zero otherwise.

3.4.1 Bipolar amplifier-comparator chip (TEKZ)

The amplifier-comparator chip [37, 38] (see Fig. 3.5) was fabricated by Tektronix with SHPi bipolar technology. Each channel is laid out at $72\mu m$ width, including a grounded trace between each channel. To test functionality, gain and noise, test pulses can be injected in the amplifiers through $40fF$ input capacitors; four lines serve the 64 channels, grouped in four groups of sixteen. Given the variation in length of the detector's strips and, consequently, of the input capacitive load, the preamplifier needs to have low input impedance to keep gain variation within 5%. The shaping time is $\tau_s = 32ns$ and the overall gain is about $150mV/fC$.

The amplifier is followed by a comparator with externally programmable threshold, which gives an output signal of about $40ns$ width and $800mV$ amplitude. The minimum operable threshold corresponds to $1fC$ charge signal, equivalent to 25% of a minimum ionizing particle's signal[3]. The comparator is decoupled via a $10pF$ capacitor, resulting in a high-pass

---
[3]The threshold is typically at 4 sigma above the rms noise level.
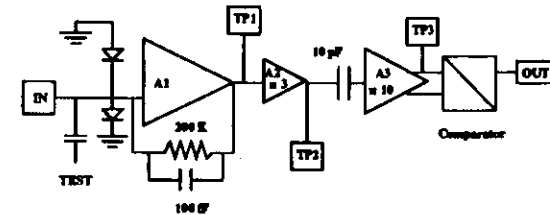
Figure 3.5: Functional circuit diagram of the amplifier-comparator chip TEKZ. TP1, TP2, and TP3 are internal probe points on the chip.

filter above 100 kHz. No reset is required and the dead time is of the order of $150ns$.

The power is $2mW/channel$ and the radiation resistance is guaranteed by the use of small npn emitter dimensions ($1.2\mu m \times 8\mu m$). The radiation hardness of the chip was tested up to radiation doses of 5 Mrad of γ rays and $10^{14}p/cm^2$ of $650MeV$ protons showing no sensible degradation in the performance [39].

3.4.2 CMOS Digital Time Slice Chip (DTSC)

The digital chip [40] (Digital Time Slice Chip, see Fig. 3.6) was designed in order to perform pipelining and multiplexing of the data flow, and it was realised in radiation hard $1.2\mu m$ CMOS technology by UTMC, California. Each DTSC has 64 input channels directly bonded
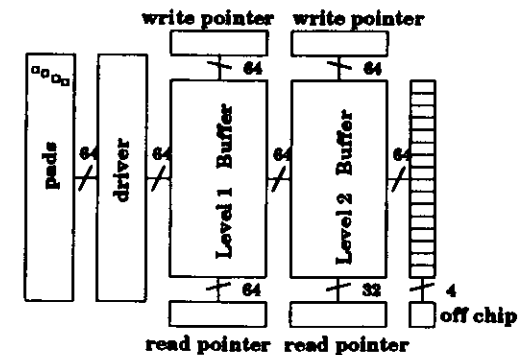
Figure 3.6: Block diagram of the Digital Time Slice Chip.

to the TEKZ outputs, it is controlled by four address lines and has four serial data lines in output. The chip consists of two pipelines whose length is determined by the time required to process the ZEUS GFLT and GSLT decisions.

The first pipeline is 64 locations deep, allowing for the ZEUS GFLT latency of $6\mu s$. The event is clocked as a time slice into the buffer with $10MHz$, the HERA collision, frequency and read out in case of a valid ZEUS trigger, otherwise overwritten.

The second pipeline is 32 locations deep to allow the storage of the data waiting for a valid GSLT decision even in case of high GFLT rates. Only the first buffer of the DTSC is used in the current read-out scheme. The data are transferred out of the DTSC, to the VMEbus memories, right after the GFLT decision is taken.

3.5 Testing of the FEE chips

The two chips were tested separately before assembly to minimize rework once the chips are glued on the hybrid support. The bipolar chip was tested in the Santa Cruz Institute for Particle Physics (SCIPP) laboratories and detailed information about the characteristics and their uniformity over the whole production was extracted [41]. The digital chip was mainly tested at the foundry but the functionality of a subsample ($\sim 10\%$) was cross-checked at SCIPP.

3.5.1 Testing of the bipolar amplifier-comparator chip (TEKZ)

The bipolar chips were delivered diced and they were tested using a probe card and a test apparatus as described in [41]. Given the tight space between the output pads, only 32 channels, selected with an alternate pattern among the two rows of pads, could be checked at a time. The remaining 32 channels were tested on a smaller sample with a specular probe card.

Using the test inputs, the gain and noise of the amplifier was determined by injecting through the calibration capacitors pulses of known charge, i.e. 1 and $2fC$, and measuring the counting rate fraction (occupancy) as a function of the threshold voltage on the comparator (see Fig. 3.7). The threshold voltage difference between the 50% occupancy points is the gain in mV/fC. The width of the curve (independently of the input charge) gives the noise, which, for a gaussian distribution, follows the relation:

$$\sigma(noise) = (88\% - 12\%) input\ charge/2.35,\qquad(3.1)$$

i.e. the threshold voltage difference between the 88% and 12% occupancy points is equal to the noise FWHM (the data are actually fitted with an error function in order to extract the 50% points and the noise sigma). Fig. 3.8a shows the distribution of the measured gains for the total number of TEKZ channels tested. The mean is $164mV/fC$ with an RMS of $7mV/fC$. The noise sigmas are shown in Fig. 3.8b with a central value of $17.2mV$, corresponding to a noise charge of $\sigma = 656e^-$. This gives an excellent $1120e^-$ noise for the maximum $11pF$ load.

The crosstalk of the system was checked bonding the chip to a 0° detector ($82\mu m$ strip pitch) and using a $1064nm$ laser source collimated to a spot size of $20\mu m$. The electronic channel crosstalk was measured to be less than 2%, while the analog signal sharing was around 14%.

The yield averaged over six wafers (669 chips) consisted in 72% of the chips having no bad channels over the 32 out of 64 measured ones. For the assembly chips with no bad channels were accepted, with an estimate of a 0.2% failures on the unmeasured 32 channels.
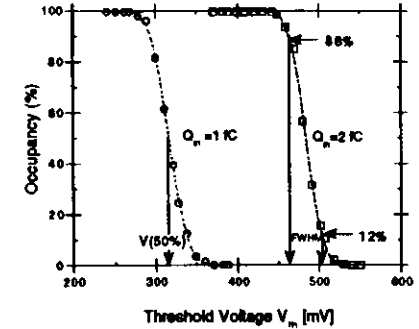
Figure 3.7: Schematic of the gain and noise determination from the threshold curves corresponding to 1 and $2fC$ input charges.

3.5.2 Testing of the CMOS Digital Time Slice Chip (DTSC)

The CMOS chips were tested at UTMC using test vectors derived in the simulation of the design. The functionality criteria were principally based on the measured current draw. Failures were introduced during the assembling and bonding procedure as a consequence of the breaking of the overglass protection.

3.6 Assembly and testing of the detector modules

The μ-strip silicon detectors and the front end electronics were assembled on a multilayer printed circuit board, realised with eight superposed layers of Copper and Invar in order to match the coefficient of thermal expansion of the silicon. The hybrid board, shown in Fig. 3.9 with all components, serves as mechanical support for detectors and electronics, as distribution network for the detector and electronics power lines, as fanout for driving out the signal lines, and as a thermal radiator and support for a cooling copper tube ($1mm^2$ section), which is used to water-cool the system [4]. Up to 16 pairs of analog and digital chips are assembled on one hybrid board[5]. To prevent oscillations and pick-up of digital signals, analog and digital signals and power lines are routed on different planes of the hybrid. Moreover, the power to the analog chip is bypassed with filter capacitors one every other chip.

A check of the complete read-out chain was performed [43] by injecting fast light pulses ($2-3ns$) from a $1064nm$ laser diode collimated to a spot size of $20\mu m$ into the silicon detector. The laser wavelength has an absorption length in silicon of the order of $2mm$ and, therefore, the energy deposition in a $300\mu m$ thick detector is, at good approximation, uniform. The

---

[4]Thermocouples are mounted directly on the multilayer in order to remotely control the temperature on each detector unit.

[5]The assembly of the entire module, with the exception of the glueing of the detector, which, as mentioned in chapter 5, needs careful alignement, is performed at Promex inc. (CA).
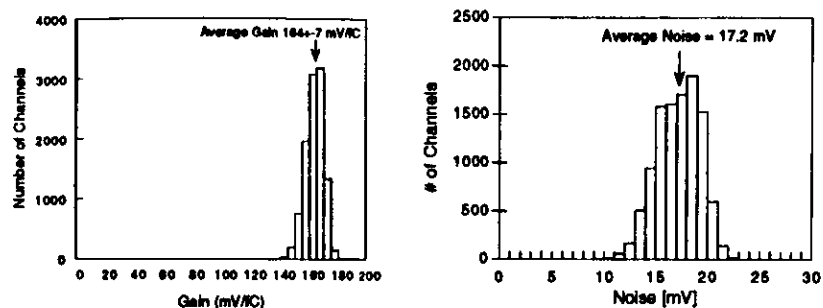
Figure 3.8: Distribution of gain (a) and noise (b) for 669 TEKZ chips with 32 channels tested.

amount of charge deposited with the laser can be set to be of the same order of the average charge deposited in silicon by a minimum ionising particle. A scan was performed across all channels with a $x - y$ platform. Dead and noisy channels were identified and the information was used later, after installation in the HERA tunnel, to check the integrity of the read-out chain.

For installation in the beam line the hybrid modules are mounted on a mechanical hand which allows precise mounting of the planes through machined locating pins. The hand is then attached, through an insulating support, to an arm which is connected, at the other end, to a moving carriage which drives the detectors towards or away from the beam. Three micrometric screws regulate the three degrees of freedom of the arm and can be used to adjust the detectors assembly inside the volume of the pot.

The hand also supports a Faraday cage that envelopes the detectors and is electrically insulated from the rest of the equipment.

3.7 The read-out system

Fig. 3.10 shows a block diagram of the LPS data path from the detector to the read-out VMEbus and the path of the signals issued from the GFLT to the front-end electronics. The main components that interface the front-end electronics and the ZEUS acquisition system are the Read-out Controller (ROC) [80] and the Serial Read-out Controller (SRC) [79].

- The ROC drives the signals responsible for managing the digital chip buffers. It contains a section of memories organised like the DTSC buffers: a mirror image of the 64 stage first level trigger buffer (Level 1), and of the 32 stage second level trigger buffer (Level-2). The Level 1 buffer map contains a record of the GFLT information (e.g. Level 1 trigger number and ambiguity, bunch crossing number, etc.), while the Level-2 buffer controls the pointers to the SRC memories, where, in the current operating mode (Level 1-driven mode), the data out of the DTSC first buffer are stored, waiting for
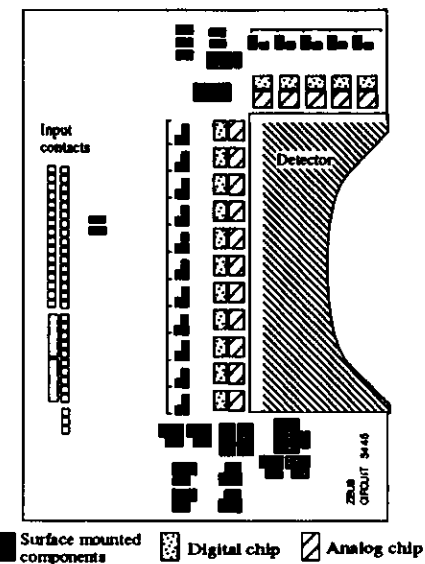
Figure 3.9: Layout of one of the LPS modules.

the GSLT decision. The ROC transmits the beam crossing syncronisation signal and interrupts the read-out processor (FIC) when the GFLT data are ready.

- The SRC modules control the data transfer between the front-end and the VMEbus environment and the ZEUS EVent Builder (EVB). One SRC serves one pot; in order to reduce cabling the data transfer is multiplexed in such a way that, for each pot, 4 signals (4 strips) are received in the SRC memory at a time. The SRC is equipped with a zero-suppressor, in such a way that only 4 strip groups containing at least one hit in the group are recorded in the memory. One 16 bit data word (whose sintax is defined in Fig. 6.3 encodes the 4 strip pattern and the address of this pattern within a pot. The sequence according to which the front-end is read out is fully software programmable; faulty DTSCs can be excluded and a subset of DTSCs masked in order to define a restricted detector region contributing to the LPS Level 2 trigger.

3.7.1 Data acquisition sequence

The different steps executed by the read-out sequence are :

- The HERA clock is received by the front-ends. All the digital responses (0 or 1) of the ~ 50000 TEKZ signals are then injected into the FLT pipelines in the DTSC chips. After 64 clock periods, the data come out of the pipeline exactly at the moment when the corresponding Level 1 decision is available. It is then either accepted by the GFLT and stored in the circular buffer or simply ignored in case of a Level 1 reject.

- The GFLT accepted data are stored in the circular 32 stage Level 2 primary buffer. At this level of the process, the read-out may operate in two modes depending whether or not the LPS contributes to the ZEUS GSLT :

  - Level-2-driven mode : the data are kept in the 32 stage second level buffer in the DTSC until the GSLT is received. In the case of a positive GSLT, a signal transmitted by the ROC moves the buffer pointers. The data are then transfered to the VMEbus memories.

  - Level 1-driven mode : the data are transfered as quickly as possible to the VMEbus memories in order to be available for LPS level 2 calculations. Up to now, only this mode is supported by the read-out software.

- In the Level 1-driven mode, the SRC memories are used as second level buffers. The locations of the data in these memories as well as their status are controlled by the read-out processor (FIC).

- The LPS Level 2 decision data is transmitted from the FIC to the GSLT by means of a transputer link.

- The GSLT decision is sent back to the FIC across another transputer link.

- When a GSLT is received in the VMEbus environement, the FIC is responsible either to discard the data in the SRC memories (negative GSLT) or to send the data to the ZEUS EVent Builder (EVB).

- Before being sent to the EVB, the data are collected by the FIC in an ADAMO table format [81]. The design value for the ZEUS positive GSLT rate is 100 Hz.

- LPS ADAMO data tables are sent to the ZEUS TLT computer farm. The design value for the ZEUS positive TLT rate is 3 Hz.

3.8 Performance during the 1993 data taking

Data were collected from the 26th of October to the 4th of November 1993, corresponding to an integrated luminosity of $\approx 28nb^{-1}$. About 30% of the complete spectrometer, namely 11 planes in the three stations $S4$, $S5$, and $S6$ were installed. By using simple reconstruction algorithms based on two station correlations (see chapter 5) a sample of $x_L = 1$ tracks was selected both in the deep inelastic and in the photoproduction regime. A first determination of the resolution in the transverse and longitudinal momentum of the detected proton was obtained [90] and some of the methods used in the 1994 alignment were established.

Figure 3.10: LPS signals and data paths.

Chapter 4

Monte Carlo

4.1 ZEUS offline software

The ZEUS offline software is structured into modules connected to the different physics requirements (e.g. the signal reconstruction and/or simulation of the various detector's components and the information matching between them). Each module is centrally maintained (by using the CMZ [45] code management tool) in order to comply with the developments of the detector description and of the analysis techniques whilst preserving the integrity of the existing code. The modules, although independently usable, are grouped into four main packages (the block diagram is shown in Fig. 4.1) which serve to the purpose of centrally producing the data used by the whole ZEUS physics analysis.

ZDIS (Zeus interface to Deep Inelastic Scattering) [46] is the interface program between the Monte Carlo generators and the simulation of the apparatus. The output consists of the four-momenta of the particles produced in the interaction and of the values of the relevant kinematical variables (e.g. x and Q^2).

MOZART (MOnte carlo for Zeus Analysis, Reconstruction and Trigger) is a description of the detector components including the characteristics of the materials and of the geometry. Through MOZART, particles traveling in the detector are tracked and their interaction with the variety of the detector materials is simulated (at this purpose MOZART is linked to the GEANT [47] package). The combination of events generators (ZDIS output) and the detector simulation relates the true distributions of variables (information stored in the data structure MCTRUTH) with those observed in the detector (contained in the RAWDATA structure).

ZGANA (ZG313 ANAlysis) [48] is a simulation of the ZEUS three levels trigger. Unlike the online case, the data which do not pass the trigger requirements are saved in order to estimate the trigger efficiencies.

ZEPHYR (ZEus PHYsics Reconstruction) [49] is the event reconstruction program. The raw data from the online acquisition system as well as the output of the simulation are processed in order to provide the energy, momentum and timing information used by the physics analysis. The reconstruction is divided in several phases:
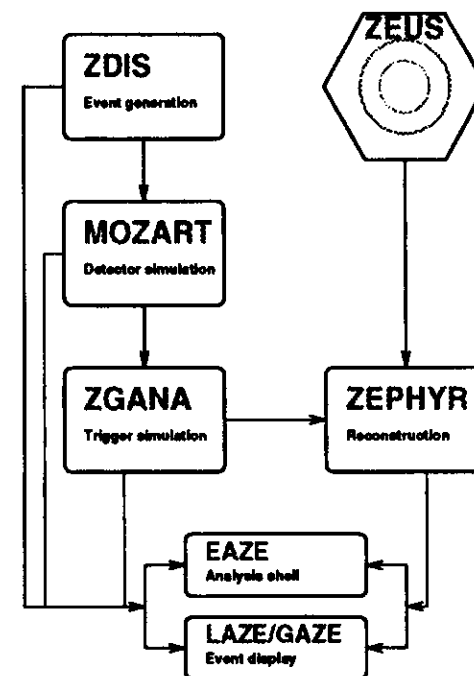
Figure 4.1: Block diagram of the ZEUS offline software. The arrows indicate the data production sequence. The Monte Carlo generation proceeds in three stages: ZDIS shapes the various ep scattering processes, MOZART reproduces the detector's response, and ZGANA simulates the ZEUS trigger logic. The data collected by the experiment together with those produced by the Monte Carlo chain are processed by the ZEPHYR reconstruction algorithms, stored and made accessible to the user through a graphic display program (LAZE) and a standard analysis shell (EAZE).

- *PHASE 1*: the data are reconstructed for the individual components giving quantities such as track segments in the chambers and calibrated calorimeter cells energy and timing. The LPS reconstruction takes place in this phase.

- *PHASE 2*: compound objects are formed, such as tracks in the different tracking devices (CTD/VXD/RTD and SRTD) to give a measurement of the interaction vertex and an extrapolation to the peripheral detectors (e.g. the muons chambers). Clustering algorithms are applied to group calorimeter cells.

- *PHASE 3*: provides information for the physics analysis: particles four-momenta, jets and electron identification, basic kinematical variables evaluation etc. It has been implemented for the first time in 1994.

- *DST selection*: the data corresponding to different physics processes are preselected and stored on disk in the form of a Data Summary Tape (DST). Each selection corresponds to a bit pattern associated to every event. The DST selection relevant to the neutral current DIS events can be found in [50].

4.2 Monte Carlo event generators

Event generators based on MC techniques have been extensively used in high energy physics to understand detector effects, acceptance and dependence of the observed distributions on the parameters of the physics models.

The inclusive diffractive cross section consists of elastic scattering, of the "resonance region" of enhancement and of the low and high mass continuum. This is illustrated in Fig. 4.2, which shows the differential cross section for $pd \to Xd$ scattering [52] as a function of M_X^2, at fixed t.
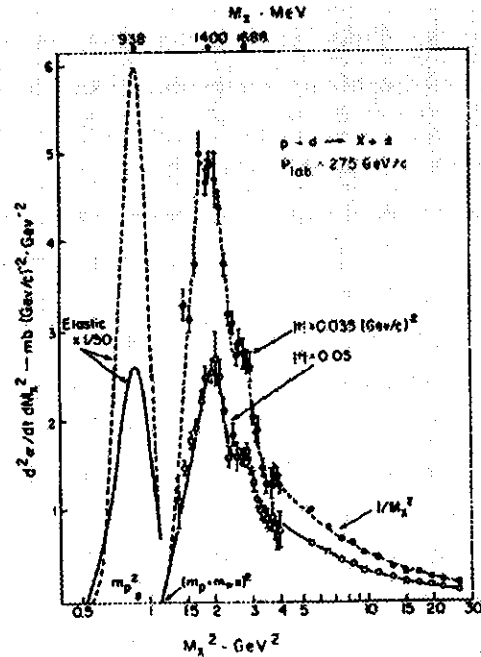
Figure 4.2: Differential cross section at fixed t versus M_X^2 for $pd \to Xd$ at $275 GeV/c$.

Some of the MC generators used to model $\gamma^* p \to Xp$ scattering cover different ranges for the diffractive mass M_X and are used in conjunction with each other. The generators for

both diffractive and non diffractive scattering are detailed below, together with their specific M_X region of validity.

The MC event samples used in the analysis of the 1993 and 1994 data were generated using versions of the detector simulation and reconstruction which reflected the status of the detector components and trigger during those periods. The event samples for the 1994(1993) analysis have been generated with a lower Q^2 cut of $\simeq 2(4) GeV^2$.

4.2.1 Diffractive dissociation of the photon

The diffractive dissociation of the virtual photon (Fig. 4.3a,c), was modeled using four MC generators based on pomeron exchange, the RAPGAP program, the POMPYT program, a generator based on the Nikolaev Zakharov model (EPDIFFR) and a generator for soft diffractive photon-proton collisions (EPSOFT).
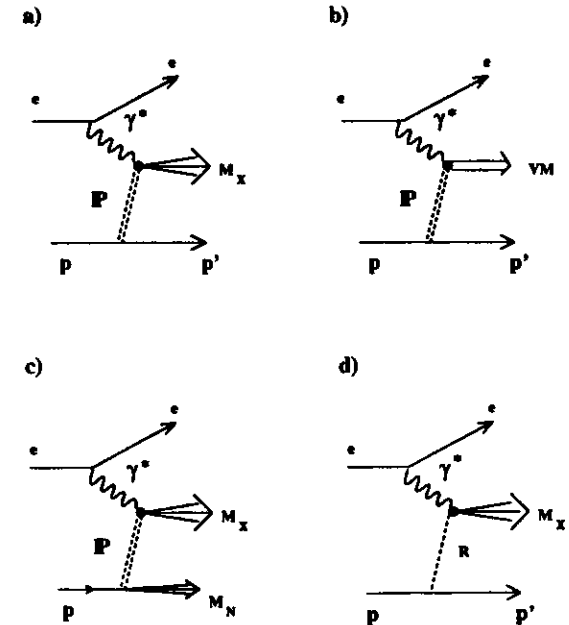
Figure 4.3: Diagrams for the processes modeled by the MC generators. a) Diffractive dissociation of the photon. b) Diffractive dissociation of the photon into a resonance state (vector meson). c) Diffractive dissociation of the photon and the proton. d) Reggeon exchange.

RAPGAP (high mass continuum)

The RAPGAP [53] program is based on the idea of Ingelman and Schlein [55] to treat the pomeron like a "particle" emitted by the proton whose constituents take part in the hard interaction. The diffractive structure function can thus be factorised in a flux of pomerons from the proton vertex (dependent on t and x_{IP}) and a pomeron structure function (dependent on β and Q^2). The RAPGAP generator was mainly used for the analysis of the 1994 data. For the flux the Streng [56] parametrisation was used:

$$f_{IP}(x_{IP}, t) = \frac{\beta_{IP}^2(t)}{16\pi} x_{IP}^{1-2\alpha_{IP}(t)}$$

$$= \frac{\beta_{IP}^2(0)}{16\pi} x_{IP}^{1-2\alpha_{IP}(t)} e^{-b_0|t|}$$

$$= \frac{\beta_{IP}^2(0)}{16\pi} x_{IP}^{1-2\alpha_{IP}(0)} e^{-b_{eff}|t|},$$

with

$$b_{eff} = b_0 + 2\alpha'_{IP} log(\frac{1}{x_{IP}}) = 4 GeV^{-2},$$

$$\alpha_{IP} = \alpha_{IP}(0) + \alpha'_{IP} t = 1.085 + 0.25 GeV^{-2} \cdot t,$$

while for the pomeron structure function the form fitted to the 1993 analysis (see chapter 9) was used, which contains a mixture of a "hard" ($\propto \beta(1-\beta)$) and a "soft" ($\propto (1-\beta)^2$) quark parton density. The program is interfaced to HERACLES [57] for the QED radiative corrections, the parton shower is simulated as implemented in the ARIADNE [58] colour dipole model and the fragmentation is carried out with the Lund string model as in JETSET [59]. The events were generated with an approximate lower M_X cut of $1 GeV$.

POMPYT (high mass continuum)

The philosophy of the POMPYT generator [60] is the same of the RAPGAP one, i.e. factorisation and pomeron partonic structure. Two POMPYT samples were generated for the analysis of the 1993 data, corresponding to a hard quarkonic structure function,

$$F_2^{IP}(\beta, Q^2) = \sum_{q_i} e_i^2 \beta f_q(\beta, Q^2) = \frac{5}{3} \cdot \beta(1-\beta),$$

and to a soft quarkonic structure function,

$$F_2^{IP}(\beta, Q^2) = \sum_{q_i} e_i^2 \beta f_q(\beta, Q^2) = \frac{5}{3} \cdot (1-\beta)^5.$$

The two samples are denoted in the following by "Hard Pomeron" (HP) and "Soft Pomeron" (SP) respectively. The normalisation constant 5/3 is based on the assumption that the momentum sum rule (MSR) is satisfied for two light quark flavours (u,d). If s quarks had

to be included the normalisation factor would be reduced from 5/3 to 4/3 [61]. The Q^2 dependence is expected to be weak and is neglected. The Ingelman-Schlein form of the flux is parametrised by a fit to UA4 data [60, 62]:

$$f_{IP}(x_{IP}, t) = \frac{1}{2} \frac{1}{2.3 \cdot x_{IP}} \cdot (6.38\ e^{8t} + 0.424\ e^{3t}).$$

A limit in the generation of the small masses was applied by requiring that $M_{X'} > 5$ GeV, where $M_{X'}$ includes the final state electron. The program is implemented in the PYTHIA framework, which simulates hard scattering processes and uses JETSET for the fragmentation. QED radiative corrections are not implemented.

EPDIFFR (high mass continuum)

The Nikolaev and Zakharov model pictures the diffractive dissociation as a fluctuation of the photon into a $q\bar{q}$ or $q\bar{q}g$ Fock state [63, 64]. The interaction with the proton proceeds via the exchange of a BFKL [15] type pomeron, starting in lowest-order from the exchange of a Low-Nussinov [65] pomeron which corresponds to two gluons in a colour-singlet state. The cross section can be approximated by a two-component structure function of the pomeron (see chapter 1), each component having its own flux factor and different t dependence. This corresponds to factorisation breaking which is caused by BFKL evolution effects. The "hard" component reflects the case where the photon fluctuates into a $q\bar{q}$ pair and leads to a β dependence of the form $\beta(1-\beta)$ and a slope of the t dependence close to that of the diffraction slope of elastic scattering B_{el} (i.e. $e^{B_{el}t}$ with $B_{el} = 10 GeV^{-2}$). The "soft" contribution, which reflects the case where the photon fluctuates into a $q\bar{q}g$ state, is assumed to be proportional to $(1-\beta)^2$ and the normalisation is fixed by the triple pomeron coupling. The t dependence slope for the triple pomeron regime is $B_{IP} \sim \frac{1}{2} B_{el}$ and is fixed in the Monte Carlo implementation to be $6 GeV^{-2}$. The relative size of these contributions and the overall normalisation are predicted with an uncertainty of about 30%. The Monte Carlo implementation of this model [66] (referred in the following as NZ) is based on the cross section described above (and in more detail in chapter 1) and is interfaced to the Lund fragmentation scheme (using JETSET). The generation is limited to $M_X > 1.7 GeV$. No QED radiative corrections are implemented.

Event weighting

Several MC generators within the ZDIS frame (e.g. EPDIFFR and EPSOFT) make use of weighting methods in order to generate efficiently events at extremes of phase space or where the predicted cross sections are small. For example the steeply falling distributions in Q^2 and t can be generated harder then what the model prescribes, thus allowing a substantial number of events to be produced at large Q^2 and t values. The model predictions are simply recovered by using the weight wt_i assigned to each event i [51]. The weight corresponds to the event cross section computed at the generated kinematic variables. The predicted total cross section σ is therefore given by the average weight in the generated sample:

$$\sigma = \frac{\sum_{all\ i} wt_i}{N_{gen}^{MC}} \pm \frac{\sqrt{\sum_{all\ i} wt_i^2}}{N_{gen}^{MC}}.$$

EPSOFT (resonances, low and high mass continuum)

EPSOFT [67] is a MC program for simulating non diffractive and soft diffractive photon-proton collisions at HERA, including elastic vector meson production ($\gamma p \to Vp$), photon dissociation ($\gamma p \to Xp$), proton dissociation ($\gamma p \to VN$), and double dissociation ($\gamma p \to XN$). Its use for the simulation of double dissociation will be discussed in the following section. The program is implemented in the framework of HERWIG [68]. The non diffractive photon-proton collisions as well as the pomeron-proton and pomeron-photon scattering in diffractive proton collisions are treated as soft hadron-hadron collisions. Since the model does not assume any dependence on the virtuality of the photon, it can be used either in photoproduction or in DIS, although it has been tuned on photoproduction data. The cross section for the $\gamma p \to Xp$ process is parametrised in the following way:

$$\frac{d^2\sigma(\gamma p \to Xp)}{dt dM_X^2} = \sigma_{ALLM}(\gamma p) \cdot C \cdot \frac{e^{b_d t}}{(M_X^2 + Q^2 - M_V^2)^{\alpha_{IP}(0)}},$$

where the constant term $C = 0.4$ results from a fit to the hadronic data, σ_{ALLM} is the total γp cross section calculated from the ALLM [69] parametrisation, $\alpha_{IP}(0) = 1.1$ is the Regge-type soft pomeron intercept and $b_d = 6 GeV^{-2}$ is an average diffractive slope observed in hadronic diffraction at comparable center of mass energy. A sample of low mass diffractive photon dissociation events was generated in order to study the mass region not covered by the previously described MCs. The mass of the dissociating photon, M_X, was generated in the range $(m_{\rho^0} + 2m_{\pi^0}) < M_X < 100 GeV$. EPSOFT is a weighted MC and does not include QED radiative corrections.

4.2.2 Diffractive dissociation of the photon and proton, Regge exchange

EPSOFT

The events where the proton dissociates into a state of mass M_N ($ep \to eXN$) (Fig. 4.3b) were generated with the EPSOFT program, where the generation of the process relies on the parametrisation of $pp \to pp$ and $pp \to pN$ data. The parametrisation used by EPSOFT to relate the $\gamma p \to XN$ to the $\gamma p \to Xp$ cross section is given by:

$$\frac{d^2\sigma(\gamma p \to XN)}{dt dM_X^2 dM_N^2} = \frac{d^2\sigma(\gamma p \to Xp)}{dt dM_X^2} \cdot \frac{1}{2} \cdot \frac{d^2\sigma(pp \to pN)/dt dM_N^2}{d\sigma(pp \to pp)/dt},$$

where the hadronic cross sections are evaluated at the centre of mass energy W. The mass of the nucleonic system, M_N, was generated in the range $1.25 GeV < M_N < 100 GeV$ with an effective spectrum proportional to $1/M_N^2$. Since EPSOFT is modelled on hadron data it does contain, together with the pomeron-mediated excitations of the proton, the contribution from all the Regge amplitudes, including the pion exchange mechanism, (Fig. 4.3d) and their interference terms.

PION

The one pion exchange mechanism was also simulated separately with a MC implemented in the HERWIG framework. The cross section is proportional to:

$$t \cdot (1 - x_L)^{1 - 2\alpha_\pi(t)} / (t - m_\pi^2)^2,$$

where $\alpha_\pi(t) = \alpha'_\pi(t - m_\pi^2)$ is the pion trajectory.

4.2.3 Specific MC for the diffractive dissociation of the photon in resonances (vector mesons)

DIPSI

Based on the model of Ryskin [70], it assumes that the exchanged photon fluctuates into a $q\bar{q}$ pair which then interacts with the pomeron emitted by the incident proton. A detailed description of the event generation is given in [71]. The pomeron is described in terms of a gluon ladder. The cross section is proportional to:

$$[\alpha_s(\bar{q}^2)]^2 \cdot [\bar{x}g(\bar{x}, \bar{q}^2)]^2,$$

where $\alpha_s(\bar{q}^2)$ is the strong coupling constant and $\bar{x}g(\bar{x}, \bar{q}^2)$ is the gluon momentum density in the proton. The quantity $\bar{x} = (Q^2 + M_\rho^2 + |t|)/W^2$ is the fraction of the proton's momentum carried by the gluon ladder and $2\bar{q}^2$, in the leading logarithm approximation, is the upper limit for the virtuality of the two t-channel gluons of the gluon ladder; here $\bar{q}^2 = (Q^2 + M_\rho^2 + |t|)/4$ and M_ρ is the ρ^0 mass. The region of validity of the calculation is restricted to $\bar{q}^2 > 2 GeV^2$ and $\bar{x} < 0.1$.

The samples used in the 1993 analysis were generated with a cross section $\propto \frac{1}{\bar{q}^2}$ (reweighted to $\propto \frac{1}{Q^2}$) and $\propto \frac{1}{t}$.

HERACLES

A sample of events for the diffractive dissociation of the photon in vector mesons was generated using HERACLES [72] in order to properly simulate the QED radiation. The parametrisation of the Q^2, W dependence, the helicity angle distribution and ratio of the longitudinal to the transverse cross section were taken from EMC, NMC and the 1993 ZEUS data. The sample was used in the analysis of the 1994 data.

4.2.4 Non diffractive proton fragmentation

Non diffractive DIS processes with first order electroweak corrections were generated using HERACLES. The hadronic final state was simulated using the colour-dipole model including boson-gluon fusion CDMBGF [73] as implemented in ARIADNE for the QCD cascade and JETSET for the hadronisation. Diffractive events are simulated in ARIADNE by assuming that the struck quark belongs to a colourless state having only a small fraction of the proton's momentum, with the parameters tuned to the 1993 results (see chapter 9). In order to estimate the background from non diffractive DIS processes to the diffractive sample these events were discarded. The MRSA [74] proton parton density parametrisation, modified at low Q^2 as described in [75] was used.

Chapter 5

LPS reconstruction, calibration and running

The operation of the LPS is undoubtly a delicate and challenging one. The detectors have to approach the beam at minimal distances and necessitate a continuous interplay between the knowledge of the device itself and of the physics and response of the machine. There are no such complicated objects as the tracking devices [76] and, specially in the case of the LPS, much work goes in the understanding of the alignment and calibration constants which allow the reconstruction algorithms to track particles over a distance of 100m, through 65 magnetic elements.

5.1 Data taking conditions in 1994

The 1994 data taking extended over a period of five months. For the first six weeks the machine operated with colliding proton and electron beams. However, consistently low electron beam lifetimes, caused by a poor vacuum, forced HERA to operate with colliding positrons on protons for the rest of 1994: the gated luminosity collected during the 1994 positron run is shown in Fig. 5.1 for both the ZEUS detector and the LPS (ZEUS gated $3.7pb^{-1}$ from a total of $6.2pb^{-1}$ delivered by HERA) of which $\sim 39\%$ ($1.3pb^{-1}$) was taken with the LPS fully operational.

Apart from three specific problems detailed below the principal cause of the difference between the ZEUS and LPS gated luminosities was the time taken to lower the pots into the beam and the poor beam quality (or position) preventing the insertion of the pots into the beam. There were three main periods of luminosity loss for the LPS [77], as indicated in Fig. 5.1. At first luminosity was lost due to a randomly occurring timing problem due to noise when the GFLT syncronisation clock signal (derived from the HERA clock) was sent. The second main loss (around run 10000) was due to a failure of the HERA beam position monitoring system (BPM) which surveys the position of the proton beam along the quadrant of the HERA ring in which the LPS stations are placed. Finally the last two weeks of data taking were affected by severe and little understood background problems which made it almost impossible for the LPS to be inserted in the beam line. Basically no data were collected during the initial electron run, since the LPS remained in a commissioning phase until the start of the positron run. During this time much effort was devoted in establishing a
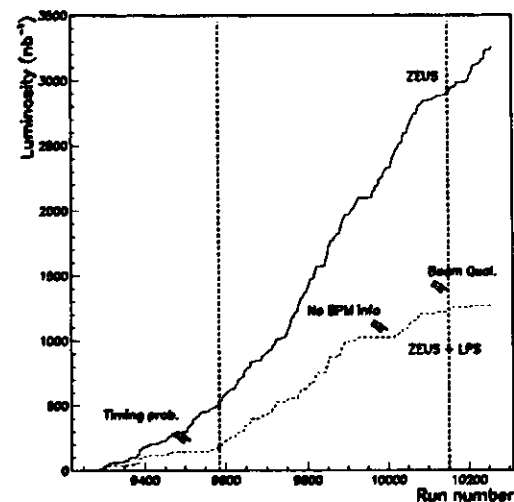
Figure 5.1: Integrated luminosity as a function of the run number. The solid line indicates the luminosity collected by the main ZEUS, the fraction with the LPS operating is represented by the dashed line. The periods corresponding to major luminosity losses for the LPS are indicated. The vertical dashed lines show the run range covered by this analysis.

safe and reliable procedure to insert the pots in the beam line as close as possible to the design position (which means in the closest case (S5) a distance of $\sim 3.5mm$ from the proton beam). The positioning of the detectors required a careful monitoring of the HERA proton collimator rates, the ZEUS background counters and the LPS trigger rates. The final positioning took place in steps of $100\mu m$ starting at $2mm$ from the final position.

During the 1994 data taking, only stations S4, S5 and S6 were equipped with detectors, not all of them completely functional. The configuration is illustrated schematically in Fig. 5.2 and summarised in more detail in Table 5.1. The stations S4, S5 and S6 consist of two Roman pots (up and down) approaching the proton beam from above and below. Only the down pots of stations S5 and S6 were equipped with planes with the three μ-strip orientations. The up pot of S4 had three of the planned six planes operational. The only pot which operated with six detector planes was S6 up following an installation in the latter part of August. In total the number of active readout channels was ~ 22000.

5.2 Data taking operation and performance of the spectrometer

The LPS zero suppressed raw data are stored (according to the format described in [78]) in a 16-bit word containing the address and the pattern of four consecutive strips including at least one hit strip (Fig. 5.3). This is the same hitcode which is contained in the SRC

Pot	Type	Planes installed	Planes readout	Channels readout
s4_up	x	-	-	-
	u	2	2	2048
	v	2	1	1024
s4_down	x	-	-	-
	u	2	2	2048
	v	2	2	1984
s5_up	x	-	-	-
	u	2	2	1856
	v	2	2	1920
s5_down	x	2	2	1152
	u	2	1	960
	v	2	2/1	1920/960
s6_up	x	-	-	-
	u	2	2	1472
	v	2	2	1920
s6_down	x	2	1/2	448/896
	u	2	2	1856
	v	2	2	1920
Total	min.	28	24	21568
	max.	28	26	22976

Table 5.1: Configuration of the spectrometer during the 1994 data taking period. The complete configuration for one pot corresponds to two planes for each of three μ-strip orientations: vertical strips (x), strips oriented at $+45°$ (v) and $-45°$ (u) in the ZEUS coordinates system. Not all the planes were available at the time of the installation. Moreover one of the u planes in S4up and in S5down had to be switched off during the entire data taking period due to a short in the power lines of the front end electronics. A problem in the address lines of the digital chips caused one of the u planes of S6up to be partially unreadable. The minimum and maximum total of readout channels is given
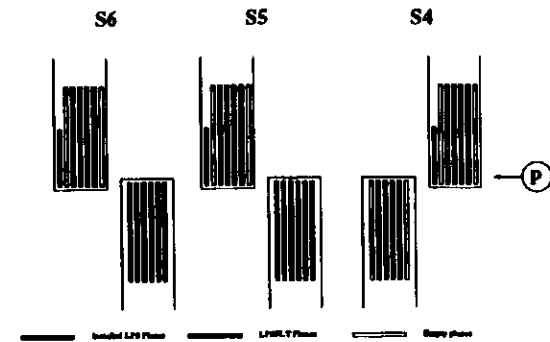
Figure 5.2: LPS silicon detector planes installed during 1994 data taking.

memories [79] (see chapter 3). The auxiliary information about the pot number and the various status registers (SRC and ROC [80]) is contained in a header table associated with every event which has a pointer to the raw data structure [81].
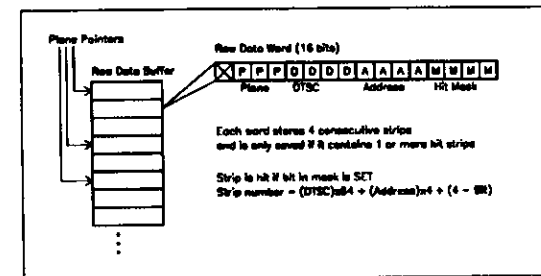
Figure 5.3: LPS raw data packing. Shown is the format for the LPS raw data, which is stored as four strips per 16 bit word.

The raw data are unpacked in preparation for the track finding. The counting rate as a function of the strip number is shown in Fig. 5.4a,b,c for three detector planes with different strip orientations. The event sample is selected by random triggers and the hit distribution shows the convolution of signal and noise. Since the main contribution to the noise of the front-end electronics is the input capacitance of the μ-strips and the latter is proportional, within an offset, to the strip length (as discussed in the following), the channel counting rate is largest for the longest strips on the detector. This effect is particularly evident on the u and v planes where the strip length varies from essentially zero up to a few cm (the

longest strip being the one which runs parallel to the elliptical detector cutout, as sketched in Fig. 5.4a,b,c).
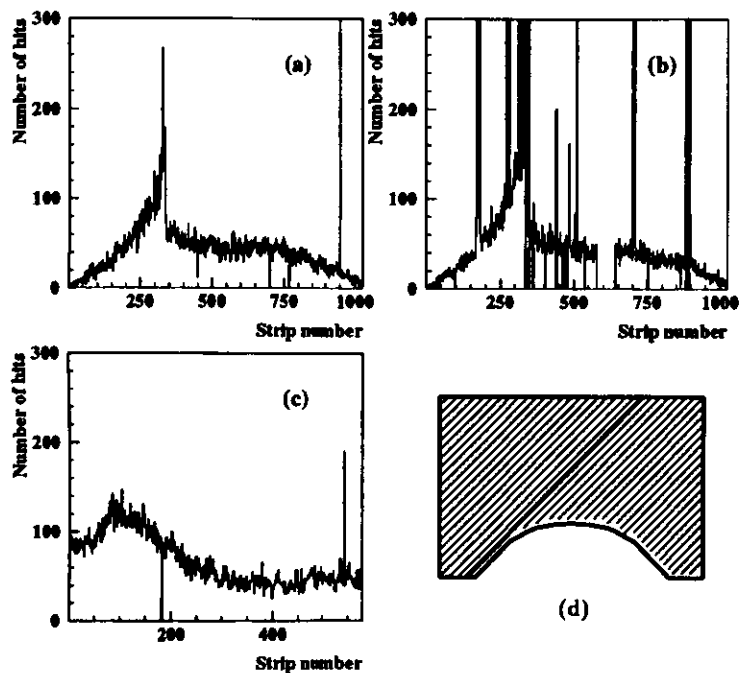
Figure 5.4: Channels counting rates for random trigger events on one of the u (a) and v (b) planes of $S4_{up}$ and one of the x (c) planes of $S5_{down}$. Dead, excessively noisy and stuck channels can be seen in each of the three views. The peak in the rates for the u and v planes correspond to the longest strip on the detector, which runs parallel to the elliptical cutout, as sketched in (d).

5.2.1 Non operational channels

Losses of efficiency were mostly identified through channel maps. After the removal of extended areas of contiguous non operable channels (mostly corresponding to non working chips), the ratio of the counting rate of each strip to the mean counting rate of its six neighbours facilitated the identification of dead, stuck and excessively noisy channels. The presence of dead channels was due either to failures of the analog chip or to defective (i.e. high leakage current) detector strips which were not bonded to the front-end electronics at assembly stage. There were also channels where the digital chip was stuck high and isolated channels with high noise. All of these effects can be seen in Fig. 5.4a,b,c. The total number

of non operational channels was of the order of 2% and rather stable. After unpacking, each hit is compared with the pre-identified list of bad channels and removed if it originated from a bad channel.

5.2.2 Calibration of the front-end electronics with no beams

Without beams colliding in the machine the basic performance of the front-end electronics was periodically checked. Through threshold scans (see chapter 3) the noise and gain of every amplifier channel was determined. Since, as mentioned above, the parasitic capacitance scales with the strip length and the amplifier noise, σ_n, depends linearly on the capacitance, an expression can be derived, which relates linearly the noise to the strip length [82]:

$$\sigma_n = 690 + 40 \cdot C(e^-) = 690 + 40 \cdot 1.2L(e^-),\qquad(5.1)$$

where C is the capacitance (in pF), L is the strip length (in cm) and the capacitance per unit length has been taken to be $1.2pF/cm$, a number which includes additional noise sources such as the amplifier noise due to coupling to the neighbouring channels. Fig. 5.5 shows the noise for one of the u planes of $S5_{down}$ as a function of the strip length together with the prediction of eq 5.1.
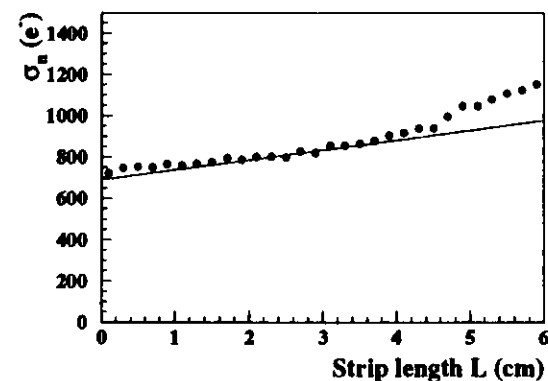
Figure 5.5: Noise σ as a function of the strip length for one of the u planes of $S5_{down}$. The line represents the relation $\sigma_n = 690 + 40 \cdot C(e^-) = 690 + 40 \cdot 1.2L(e^-)$.

An excess of noise can be observed at small lengths, due to the finite capacitance of the input pads, and at large lengths, where the leakage currents add to the noise. The leakage current for every detector plane was monitored during machine operations and data taking to study short term radiation damage, as discussed below.

5.2.3 Operation with colliding beams and radiation damage

The occupancy, defined as the number of times a strip is hit divided by the number of triggers, was measured for each channel in different operating conditions. Occupancies in the colliding beam mode are dominated by the passage of particles (leading particles from ep collisions, halo protons, synchrotron radiation from the positrons) and depend critically on both the beam conditions and the position of the inserted roman pots. Since the LPS detectors have been built and tested to withstand proton fluences up to $10^{13} p/cm^2$, where "type" inversion is known to occur, strip occupancies in excess of 1% have to be avoided. The pots were not inserted in the beam line whenever unstable beam conditions would cause the average occupancy to exceed a few % per plane. The average hit multiplicity per detector plane was also monitored and did not show large fluctuations. Fig. 5.6 shows the total number of hits per event summed over the 25 planes operating during a specific run. The average number of hits for 22k channels is 6.8 hits/event.
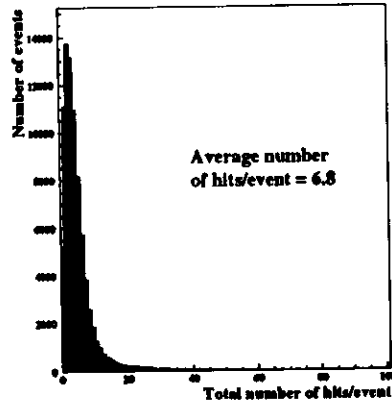
Figure 5.6: Total hit multiplicity for 25 LPS operating planes during a run with colliding proton and positron beams.

Short term radiation damage was observed through the increase of leakage current while the LPS was close to the beam, followed by exponential annealing over the time of a few hours as soon as the detectors were moved out or the beams removed from the machine.

5.3 Clustering and position reconstruction

After subtraction of noisy and dead channels, adjacent hit strips are clustered together. The result is called a hit *cluster* which is assigned a coordinate value at the center of its component

strips. Since hit clusters only supply information in one dimension (perpendicular to the strip length), they need to be combined with at least one cluster from a different orientation to get information in two dimensional coordinate space. The number of clusters per event for one plane of the spectrometer is shown in Fig. 5.7a for a selection of random triggers. The dominant component can be fitted to a Poisson distribution and represents the average noise in the detector. The mean value of less than one cluster per event indicates that the noise level is fairly low. The tail towards higher values belongs to showers generated by beam gas interactions or by the beam scraping against the beam pipe elements.
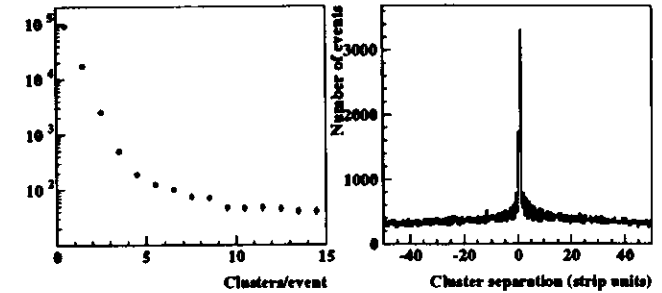
Figure 5.7: (a) Number of clusters per event for a selection of random triggers on one of the planes of $S4_{up}$. The dominant Poisson component is due to the detector noise while the tail can be attributed to showers originating from beam gas and beam scraping interactions. (b) Difference between the clusters position on two $S5_{up}$ planes with the same orientation. The narrow peak is associated with clusters belonging to the same track segment. The background is of a combinatorial nature. Pairs of clusters are matched if their distance in terms of strip units is less than 2.5 from the center of the peak. Misalignment effects between the detector planes can cause a shift of the peak position.

Coordinates are located in each pot, the first step is to combine matching clusters in different planes of the same orientation. Since a track crosses the six detectors in the pot at an angle perpendicular to the surface (the dispersion for tracks coming from the interaction vertex is estimated to be of the order of a few mrad) the signal will be recorded on the same strip for planes with identical strip orientation (modulo residual alignment uncertainties), as can be seen in Fig. 5.7b, where the difference between the position of clusters reconstructed in two planes of the same orientation is plotted against the strip number. If a match is found it replaces the pair of clusters it originates from. The coordinates are evaluated by iteration over matches and clusters in planes with different orientation. A quality code is assigned to each coordinate proportional to the number of planes involved in its reconstruction and all but the highest ten candidates per event are discarded. The remaining are fit using the strip equations (which identify the center of each strip in the space transverse to the beam direction) to produce position in x and y (in the ZEUS coordinate system) and, if there is enough information, the track direction dx/dz and dy/dz at the position, z, at the center of the pot. Moreover, since the up and down pots partially overlap, if two coordinates are found in these two pots one global fit is performed over the common clusters and the coordinate is assigned a z position corresponding to the center of the pots. The x and y position of

coordinates which pass the cut on the quality code is shown in Fig. 5.8, where the profile of the detectors is drawn to guide the eye. The two areas with highest concentration of hits in the corners of each detector correspond to $x_L \simeq 1$ tracks (which have a spatial distribution centered around the beam). Tracks with lower longitudinal momentum are deflected towards positive y values by the bending dipoles positioned between S4 and S5 (see chapter 3). The shrinkage in x of the hit distribution in S6 with respect to S5 is due to the focusing effects of quadrupoles on low x_L tracks.
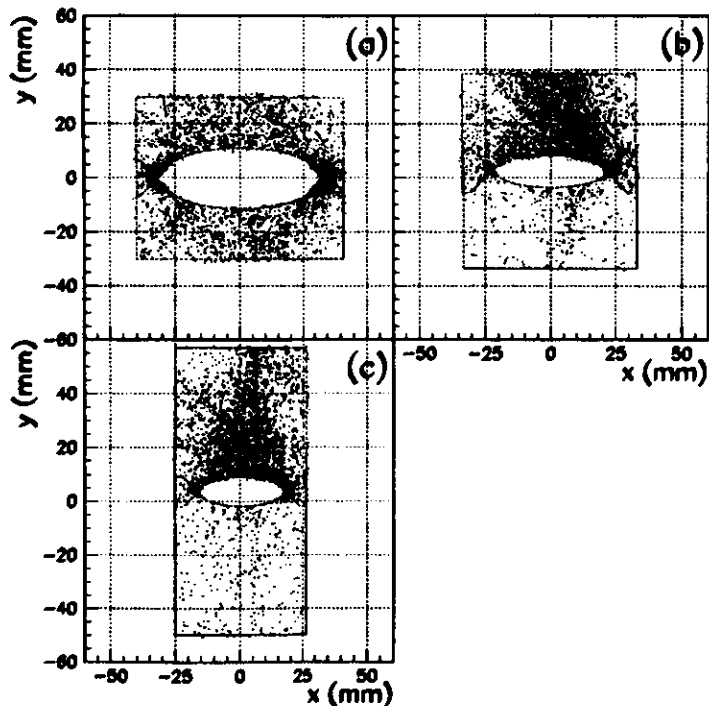
Figure 5.8: Position of reconstructed coordinates in stations S4 (a), S5 (b) and S6 (c) which pass the cut on the quality code and would therefore be used by the tracking algorithm. The profile of the detector's active area in the up and down pots is superimposed. The reference frame has the positive x direction pointing towards the centre of the HERA ring and the origin in the position of the nominal proton beam (i.e. the trajectory of a $820GeV$ proton with zero transverse momentum at the interaction vertex) at each station.

5.4 Two station correlations and momentum reconstruction

Two independent linear matrix equations (beam transport equations) can be written to relate the horizontal and vertical coordinates of the track at a given station to the positions and angles (ζ_0, ζ_0') of the track leaving the interaction point (at $z = 0$):

$$\begin{pmatrix} \zeta_k \\ \zeta_k' \end{pmatrix} = \begin{pmatrix} m_0 & m_1 \\ m_2 & m_3 \end{pmatrix} \begin{pmatrix} \zeta_0 \\ \zeta_0' \end{pmatrix} + \begin{pmatrix} b_0 \\ b_1 \end{pmatrix}, \tag{5.2}$$

where ζ_k is the horizontal or vertical coordinate of a track at station k and $\zeta_k' = d\zeta_k/dZ$ is its slope at that station relative to the nominal beam direction. The transport matrix elements m_i are known functions of x_L and describe the effect of all the quadrupoles and drift lengths. The vector $\mathbf{b}$, also a function of x_L, represents the deflection by all the dipoles (and of the quadrupoles when the magnetic axis does not coincide with the beam trajectory). Eq 5.2 is a linear equation, since the HERA magnets are designed to produce fields inside the beampipe that closely approximate ideal quadrupole and bending fields. By rewriting eq 5.2 for a pair of pots (a, b) and eliminating $\zeta_0' = 0$, it is possible to construct a set of linear equations that relate the intersection in x and y of a track in a and b:

$$x_b = A_x^{ab}(x_L)x_a + B_x^{ab}(x_L, x_0), \tag{5.3}$$

$$y_b = A_y^{ab}(x_L)y_a + B_y^{ab}(x_L, x_0), \tag{5.4}$$

where A_x^{ab} and A_y^{ab} depend on x_L through the matrix elements m^a and m^b while B_x^{ab} and B_y^{ab} are functions also of the vertex position. Except for their common x_L dependence the x and y solutions are independent. If drawn in the coordinates space (x_a, x_b) or (y_a, y_b) eqs. 5.4 form a line. Assuming that tracks originate from a common vertex (thus fixing (x_0, y_0)) each value of x_L produces a unique line in these coordinates plane. The correlation between the hit coordinates in S4 and S5 is shown as an example in the horizontal (Fig. 5.9) and vertical plane (Fig. 5.10) together with some of the x_L solutions. If the horizontal and vertical projections of one pair of coordinates measured in two pots rest on one of these lines the coordinates are consistent with being generated by a proton of that x_L. This correlation was used (see for example one of the momentum calibrations described below) in order to select samples of $x_L = 1$ (elastic and diffractive) tracks.

The LPS reconstruction code uses eqs. 5.4 to combine pairs of coordinates from different pots. A set of transport matrices for every pot at fixed intervals of x_L is built in the form of a look up table and the positions of coordinates are then checked to see if they sit between two adjacent lines. If so, the distance to the two lines is used in a linear extrapolation to predict the value of x_L (for a complete discussion see [83]).

Tracks that hit three pots are identified and a x_L solution is derived for each of the coordinates pairs which share the same hits. If the x_L solutions are compatible within errors the average x_L is used in eq. 5.2 to estimate the track transverse momentum components at the interaction vertex for each coordinate. If the transverse momenta of the three coordinates are compatible within errors then the coordinates are combined into a track. For tracks that hit two pots the transverse momentum components are extracted for the two coordinates in the pair and compared. If they agree within errors, the coordinates are combined into tracks. To produce the best estimate of the track parameters a formal track fitting method (χ^2 minimisation) was used ([85]).
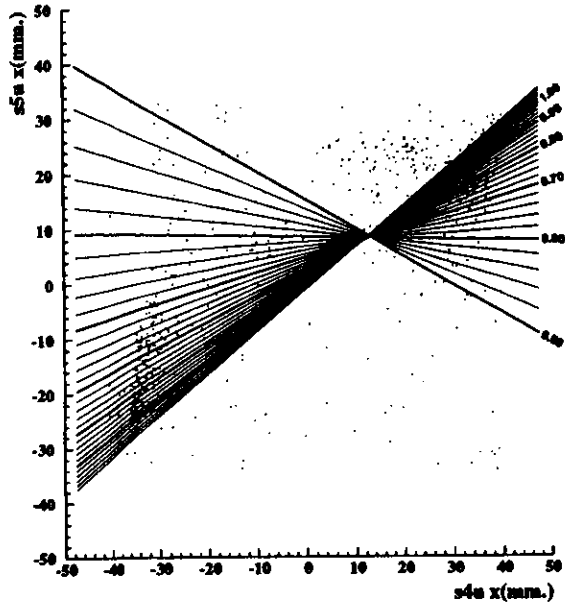
Figure 5.9: Horizontal correlation between the hit coordinates in S4 and S5. Each of the correlation lines drawn represents a value of x_L in the range (0.5,1.1). The lines are separated by 0.025 in x_L. The dots are the reconstructed horizontal hit positions in the two stations. Two dense regions appear along the $x_L = 1$ correlation line, corresponding to the enhancement of the elastic and diffractive cross section. The separation between these two populations of hits is due to the geometrical acceptance of the detectors, as can be seen in the previous figure, where they locate at the corners of the detector's elliptical cut-out. The resolution in the measurement of x_L becomes poor in the region where all the lines cross.

The obtained resolution, not including beam spread effects, in x_L and p_T is shown in Fig 5.11 and agrees well with the design specifications [44]. The x_L resolution value for $x_L = 1$ is in good agreement with the result of $\sigma_{x_L} = 0.0026$ obtained from the width of the x_L distribution for elastic (i.e. $x_L \approx 1$) photoproduced ρ^0s.

5.5 Alignment of the spectrometer

Two methods to align and to calibrate the spectrometer were developed and used at different stages of the analysis of the data collected with the LPS (for a detailed description see [85]).

5.5.1 Method I

The method described in this section to evaluate the alignment of the spectrometer is based on a careful geometrical survey of the detector installation. The geometrical alignment of
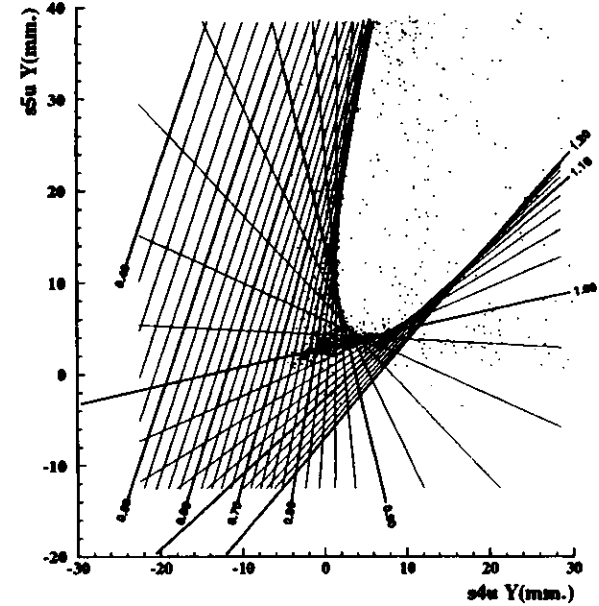
Figure 5.10: Vertical correlation between the hit coordinates in S4 and S5. The correlation lines are drawn at intervals of $x_L = 0.02$. The accumulation of points along the $x_L = 1$ line, corresponding to the elastic/diffractive peak, is clearly visible. The resolution around $x_L = 1$ it is better compared with the horizontal projection.

the strips in the reference frame of the mechanical supporting hand (which holds a packet of six detectors) was determined using a probe station with a $x - y$ precision measurement platform. This allowed the determination of the strip equations (which define the physical location of each strip) of each plane in the hand reference frame with a precision of $5\mu m$.

For each hand there are five degrees of freedom. Yaw (rotation about y axis) and pitch (rotation about x axis) do not contribute significantly due to the small angles at which tracks intersect the detectors, and the z location is fixed to survey positions. The remaining three degrees of freedom for each plane are translation in x and y of the detector packet and rotation about the z axis (roll). These three latter degrees of freedom (for the upper stations only) have been determined by the HERA surveyors in the HERA reference frame. Part of the measured values have been cross checked with an independent method which makes use of a dedicated laser system to align the three stations relatively to each other using a zone plate target and a CCD readout system [87]. The two methods were found to be in agreement within $300\mu m$.

Pitch and yaw have been measured by minimizing the χ^2 as a function of these two parameters for tracks reconstructed in two stations. Tracks are also used to align the down pots relative to the upper ones.
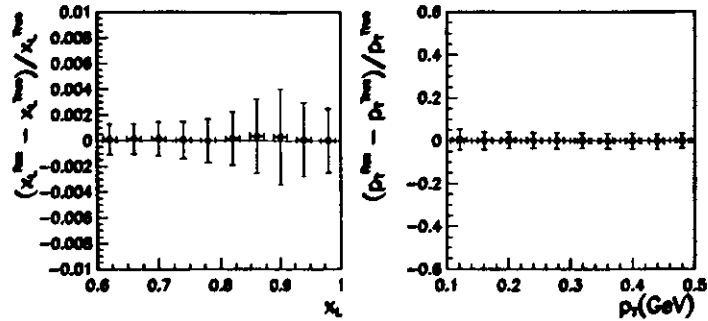
Figure 5.11: Resolution in x_L and p_T without the inclusion of the beam spread effects.

Since the LPS has a moving set-up, and it is moved in position at the beginning of each run, the alignment is sensitive to the precision of the positioning system of the pots. Pots were calibrated several times during data taking. A maximum calibration offset of $30\mu m$ in the y direction was found during 1994 data taking for all pots except for S6 down which was found on two occasions to be miscalibrated by $200\mu m$ [88].

Finally, one has to align the spectrometer relative to the ZEUS reference system, i.e. to calibrate the LPS in p_t with respect to ZEUS. This means that in order to determine the p_t of the track reconstructed in the LPS one has to know where the beam was located relative to the LPS. Once this position is determined, one can calculate the p_t of the track in the beam reference frame by using the beam transport equations, in conjunction with the measured vertex position.

Photoproduction of elastic ρ^0s offers a powerful tool for aligning the LPS with respect to the ZEUS reference system [90]. For exclusive production of vector mesons the fractional momentum x_L carried by the outgoing proton is related to the mass of the produced vector meson and to the virtuality, Q^2, by the relation:

$$1 - x_L = \frac{Q^2 + m_V^2 + p_T^2}{W^2}, \qquad (5.5)$$

where m_V is the vector meson mass, p_T is the transverse momentum of the outgoing proton and W is the $\gamma^* p$ center of mass energy. In photoproduction $Q^2 \approx 0$ such that for exclusive production of ρ^0s, $1 - x_L \approx 10^{-4}$. x_L is therefore known in such processes with an uncertainty less than the spectrometer resolution. In the limit $Q^2 \to 0$ the transverse momentum of the ρ^0 balances the transverse momentum of the proton and is therefore linearly correlated (eq 5.2) to the hit positions in the LPS pots. The ρ^0 transverse momentum is determined through the measurement of the two decay pions in the CTD with the cuts described in [89].

An example of the calibration procedure is given in Fig. 5.12, where p_x and p_y of the ρ^0 reconstructed in the CTD are plotted versus the hit positions of the proton detected in the LPS. The hatched band represents a two sigma cut around the median line of the points (the slope is fixed by the beam transport matrix) to reject multiple scattering and unphysical events. The selected points are then re-fitted and the beam position is determined from interpolation of the fitted line at $p_x = 0$ and $p_y = 0$ (see Fig. 5.13).
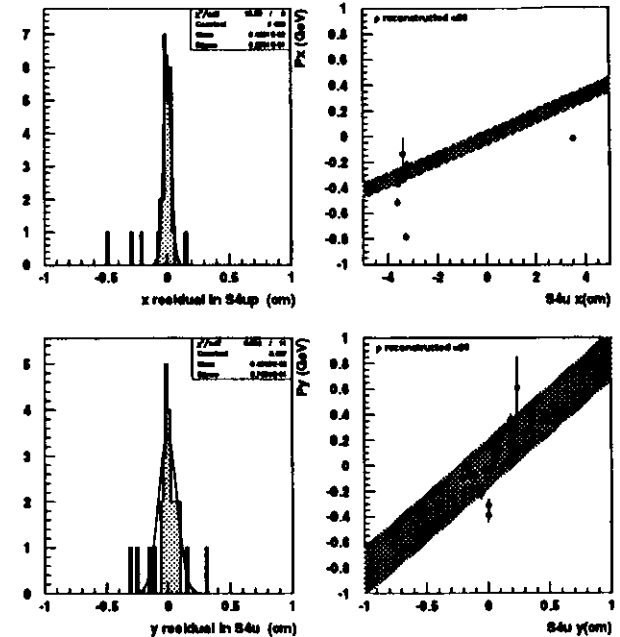
Figure 5.12: Correlation between the transverse momentum components of the ρ^0 as measured by the CTD and the x and y coordinates positions measured in $S4_{u,p}$. The width of the residual distribution around the hits median (as shown in the pictures on the left) is dominated by the emittance of the beam. The shaded band corresponds to a 2σ cut around the median.

The beam positions are recorded for every run and used for the transport equations by the reconstruction program.

5.5.2 Method II

Tracks are used in this method to align the pots relative to each other (and with the interaction vertex, thus fixing the momentum scale) and to align the spectrometer relative to the main ZEUS detector. The method proceeds as follows.

Tracks traversing the region in which the active areas of the detectors in the upper and lower pots of a station overlap are used to align the detectors inside a pot as well as to fix the relative positions of the upper and lower halves of a station. Since stations are rather compact (13 cm along the z axis), this alignment can be done quite precisely.

The relative alignment of the S4, S5 and S6 stations in the horizontal, non-bending plane

Figure 5.13: Final fit to the momentum and coordinates correlation in the horizontal and vertical plane of $S4_{xy}$. The slope of the line fit is fixed by the beam optics. The contribution due to the beam emittance ($\sigma_{p_x} = 20 MeV$ and $\sigma_{p_y} = 50 MeV$) has been added in quadrature to the errors on the data points.

is then carried out by exploiting the fact that in this plane all tracks are straight.

The dipole magnets between S4 and S5 bend the proton tracks upwards: a more complicated procedure is thus necessary to align the stations in y. The y-alignment was performed using a sample of tracks with known momentum, so that the amount of their bending can be predicted; if the bending is known, a procedure analogous to that adopted in the non-bending plane can be used. Events are selected in the ZEUS central apparatus which have an LPS track with $x_L > 0.99$. For these events x_L is evaluated using quantities measured in the central detector:

$$x_L = 1 - \frac{Q^2 + M_X^2 - t}{W^2} \approx 1 - (E + p_z)/(2E_p),\qquad(5.6)$$

where M_X is the invariant mass of the state X into which the photon has diffractively dissociated, y is the fraction of the positron energy transferred by the photon to the hadronic final state, measured in the proton rest frame, and $\sqrt{s}$ is the positron-proton centre-of-mass energy. The Jacquet-Blondel [91] technique can be used to estimate Q^2 and y; the mass M_X is determined as $M_X = E^2 - p_X^2 - p_Y^2 - p_Z^2$, where E is the sum of the energies measured in each calorimeter cell, and p_X, p_Y and p_Z are the sums of the transverse and longitudinal calorimeter energies respectively, all computed without including cells belonging to the electron. E_p is the incoming proton energy.

The relative alignment of the stations along y is then determined by the requirement that the average bend through the magnet between S4 and S5 corresponds to the fractional momentum measured with the calorimeter, $x_L = 1 - (E + p_z)/(2E_p)$. At this point the relative x, y, z position of stations S4, S5 and S6 is fixed.

In order to align S4, S5 and S6 with respect to the beam line, tracks traversing all three stations are extrapolated to the interaction region, taking into account the fields of all intervening magnetic elements (mostly quadrupoles). The positions of the detectors are adjusted with respect to the quadrupole axes such that the average position of the extrapolated vertex

is the same as that measured by the central tracking detectors, and independent of x_L. This ensures that the detectors are well aligned relative to ZEUS and the HERA quadrupole axes.

Finally events with elastic photoproduction of ρ^0 mesons are used to determine the average position of the proton beam with respect to the LPS detectors. For these events, the average value of p_T measured by the LPS plus that measured by the central tracking detectors is required to be zero, by adding a constant offset to the angle of the fitted track. This takes into account the fact that the beam is not centred along the quadrupole axes. Elastic ρ^0 events provide the best calibration for this offset, with an error of less than 10 μrad. The obtained value for the proton beam tilt is fed into the Monte Carlo simulation.

5.6 Monte Carlo simulation

The LPS Monte Carlo simulation reproduces the signal from particles entering the spectrometer by carefully describing the details of:

- The geometry of the beampipe apertures and the LPS detectors.

- The magnetic fields of the proton ring HERA magnets.

- The response and noise of the μ-strip silicon detectors.

- The description of the proton beam emittance and its related effects.

5.6.1 Geometry and magnetic fields

The LPS Monte Carlo code contains the simulation (which uses the GEANT [47] package) of the geometry of 85 meters of the HERA beam line, including 23 magnets with accessories. Developed over a span of five years [92, 93], the LPS simulation has been updated based on observations from the 1994 data. A schematic of the geometry is shown in Fig. 5.14.

Typical magnets are simulated as a box or cylinder made out of magnet material containing a volume of air to define the inside dimensions. For quadrupole magnets where the inside dimensions are more complicated, four 90° slices of cylinders of magnet material are used instead. A beampipe made out of iron and containing vacuum is placed inside the inner dimensions. Whereas the shape of the magnet are only approximately simulated, more attention has been placed on the exact shape of the beampipe because of its influence on the acceptance. Except for a small number of approximations, all beampipe inner dimensions match blueprint specifications.

The GEANT simulation of the silicon detector's active area has been accomplished by the use of overlapping trapezoidal and elliptical volumes.

The size of the dipole and quadrupole fields have been obtained with the help of the HERA machine group and implemented in the simulation. Extensive comparison between the particle trajectories in GEANT and in the LPS matrix ray tracing program BEAM9 [84] has been performed.

5.6.2 Detector response

The simulation of the silicon μ-strip detectors includes the effects of efficiency, noise, cluster size and dead channels. The single hit efficiency is simulated by randomly removing hits

produced by tracks according to the efficiency values determined from the 1994 data (details can be found in [85]). The efficiency as a function of plane number is shown in Fig. 5.15, where the run has been divided into 5 run periods. Plane 40 (S5 down) was operating well for the first two run periods, but had a digital failure during the third and was off during the last two periods. The lower bias voltage in S6 is expected to be the cause for their lower efficiency.

The noise is simulated by randomly generating for each plane in each event n noise hits according to a Poisson distribution with mean value determined by selecting and fitting FLT pass-through events in proportion to the LPS luminosity (after removal of beam halo tracks and showers). This produces noise in proportion to the strips area, which is consistent with both synchrotron radiation, because the sources are diffuse, and electron noise, which is proportional to the strip's capacitance.

The effect of clustering, where a track produces hits in more than one strip, can be caused by two sources: electronic cross-talk or charge sharing. The former effect degrades resolution and the latter enhances it. Both effects are described in the simulation by randomly adding one or two strips to either side of the cluster associated with the track (cross-talk) and by extending the cluster span by a uniform amount on both sides (charge sharing).

The simulation of the suppression of dead and noisy channels is performed in the reconstruction program, according to a channel list which is determined at the beginning of each run.

5.6.3 Beam simulation

Since the LPS measures track quantities with respect to the nominal proton beam direction accurate simulations of the vertex position, vertex size, proton beam tilt and proton emittance are essential. The parameters used by the beam simulation, determined from data, are:

- A mean vertex position of $x = 0.139$ cm and $y = -0.129$ cm for the positron running in 1994.

- A vertex Gaussian width of $\delta x = 0.033$ cm and $\delta y = 0.009$ cm (both vertex position and width are determined by the extrapolation to the vertex of those tracks which give a coincidence of three LPS stations).

- A proton beam tilt of $p_x = -16$ MeV and $p_y = -109$ MeV (if the beam is traveling at an angle through ZEUS, this produces an absolute p_T offset in the LPS).

- An emittance of Gaussian width $\delta p_x = 40$ MeV and $\delta p_y = 90$ MeV (large enough to dominate the p_T resolution of the LPS).

5.6.4 Comparison with data

An extensive comparison of deep inelastic diffractive data and Monte Carlo is presented in chapter 6. In particular the p_T and the vertex (the latter shown here in Fig 5.16) distributions are well reproduced confirming the integrity of the beam simulation.

The distribution of the distance of each fitted track to the closest beam aperture along its path is shown in Fig 5.17. The good agreement observed between data and Monte Carlo confirms the precision of the simulation of the beam apertures.

5.7 Data format

The LPS reconstructed data and the various constants used by both the reconstruction and the simulation program are stored in ADAMO [78] tables whose format is specified by the Data Definition Language (DDL) syntax, which is the source for the description of the the whole ZEUS data structure. The ADAMO structure, developed at CERN by the ALEPH collaboration, provides a simple framework for the management of data structures, their definition, storage and handling through a FORTAN program. Every structure can be syntesised into a group of entities, characterized by attributes and linked among themselves by relations.

The LPS data structure is subdivided in various entities which trace the different phases of the reconstruction algorithm:

- **Clusters (LPCLUS table)**: groups of adjacent strips giving a signal on a single plane. The attributes are the position of the center of the cluster in strip units (pos), the cluster width (width) and the plane number (nr).

- **Coordinates (LPCOOR table)**: groups of clusters in station sta which gives rise to a track segment. Other attributes are the position (hit) and orientation (slp) of the track segment and the number of planes involved (Npla). The attribute Mtch indicates if the coordinate has been obtained by matching two pots and in this case Chisq gives the χ^2 of the fit.

- **Tracks (LPTRAK table)**: the attributes are the momentum (p), the vertex position (vtx), the covariance matrix of the fit (cov), the χ^2 of the track (Chisq), the number of degrees of freedom (Ndof), the total number of hit planes (Nhit) and the number of planes the track should have hit (Ntot) on the basis of the fit result.

Two additional tables (LPCLO and LPCOTR) relate the above entities.

The constants used by the reconstruction program and by the simulation can be divided in two categories:

- **Condition constants**: contain information on the status of the detector and are overwritten in the occurence of a hardware change which could lead to a variation in the data taking efficiency or in the track reconstruction. There are two sets of constants, one for the data and one for the Monte Carlo.

- **Calibration constants**: contain the parameters which change on a run by run basis, or even within a run.

The condition constants for the data are stored in the following tables:

- **LPCONF** (detector configuration). This table contains the list of the DTSCs read out for each of the planes together with a pointer to the dead and noisy channels list.

- **LPNLST** (noisy channels list) with the channels encoded as for the online acquisition programs.

- **LPDLST** (dead channels list). Same as above.

- **LPSURV** (detector survey). It contains the position and orientation of each of the LPS silicon planes through a parametrisation which is called the "strip equation".

A mirror structure exists for the Monte Carlo:

- **LPCON** (detector configuration).

- **LPMNLS** (noisy channels list).

- **LPMDLS** (dead channels list).

- **LPMPOS** (motor positions). In this table are stored the motor positions for the simulation of the LPS stations.

- **LPDETC** (parameters for the simulation of the detector response). It contains the constants used to simulate the efficiency, charge sharing, cross talk and noise for each plane of the spectrometer.

The calibration constants are stored in the tables:

- **LPEVTR** (main index). This tables contains a run list and for each run the list of events subsamples. Each one is related with the three tables **LPMOTR**, **LPBEAM** and **LPCALB**.

- **LPMOTR** (motor positions). In this tables are stored all the positions of the motors (nine in/out movements and nine lateral movements) of the LPS pots.

- **LPBEAM** (HERA parameters). It contains a series of parameters connected to the machine status:

  1. Average current in the magnets used by the reconstruction.

  2. Average beam position at the 8 beam position monitors located along the proton beam in the quadrant of the ring occupied by the LPS.

  3. Horizontal and vertical alignment constants for the quadrupoles between the interaction point and the last of the LPS stations.

  4. Average vertex position obtained in the alignment and calibration of the spectrometer.

  5. Average horizontal and vertical angle of the proton beam at the interaction point.

- **LPCALB** (ρ^o calibration). Here are stored the results of the calibration described in section 5.5.1 with the relative errors.

In 1994 four condition configurations correspondent to major changes in the hardware status of the detector were defined together with 352 different sets of calibration constants.

Figure 5.14: Overview of the LPS GEANT Geometry. Drawn by GEANT is an y/z view of the HERA beamline from five to 90 meters starting at the lower right and continuing along the top. The geometry is drawn twice, both at the normal scale (under axis) and with the vertical scale exaggerated to show more detail. The six LPS stations and each magnet are labelled. The axis values are in meters from the interaction point.

Figure 5.15: Single hit efficiency as a function of plane number

Figure 5.16: Data (dots) and MC (solid line) distributions of the x and y vertex positions (in cm) as determined by the extrapolation of tracks corresponding to three stations coincidences. The data events correspond to run 9720, whose configuration is implemented in the Monte Carlo simulation.

Figure 5.17: The distribution of the distance of each fitted track to the closest beam aperture (in mm) for data (dots) and Monte Carlo (solid line).

Chapter 6

Event selection

In the following, the backgrounds to the selection of deep inelastic diffractive events are listed in decreasing order of importance, together with the identification and rejection methods [95, 96, 98]. Although the description will concentrate on the details of the 1994 data selection and background subtraction (with particular emphasis to the LPS) the basic features are common to the analysis of the 1993 data, which will be covered in chapter 9.

6.1 Background subtraction in the DIS sample

6.1.1 Non-ep backgrounds

- The majority of the events where the proton beam interacts with the residual gas in the beam pipe are removed by applying a cut on the calorimeter timing. As discussed in chapter 1, the plastic scintillator tiles used in calorimeter provide the time of the energy deposit with a resolution of 1 ns. Mean times are calculated, for each of the three parts of the calorimeter, FCAL BCAL and RCAL using the energy weighted average of all the photomultipliers (PMTs) belonging to that part of the calorimeter (the time for each individual cell is determined from the two PMTs reading the cell).
  The timing measurement is calibrated with respect to the HERA clock such that collisions occurring at the nominal interaction point, $z = 0$, correspond to t=0 ns both in FCAL and in RCAL, as illustrated in Fig 6.1a. Proton-beam gas events which occur upstream give rise to a shower of particles in the forward direction (Fig 6.1b). Since the interaction producing them takes place early (before the proton bunch reaches the interaction region) the time at which particles are deposited in RCAL peaks at negative values, around -10 ns.

- Electron gas interactions which do not deposit energy in the FCAL cannot be removed by the timing cuts, since the interaction products reach the RCAL in time with the electron. The contamination from both proton and electron gas events in the final sample can be evaluated by studying the unpaired bunches, respectively e-pilot and p-pilot bunches. A statistical estimate can be obtained by weighting the number of events originating from unpaired bunches surviving the selection cuts with the ratio of the current in the ep bunches to the pilot ones.
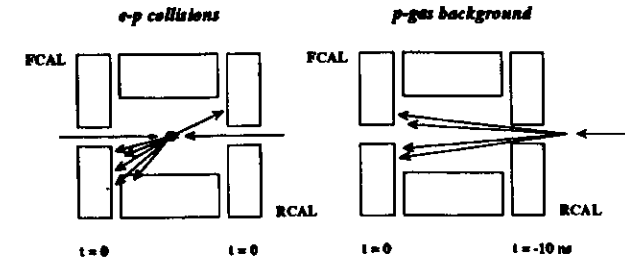
Figure 6.1: Use of the calorimeter timing for distinguishing between ep collisions at the nominal interaction region and upstream beam-gas interactions.

- Interactions of the proton beam halo with the beampipe walls or objects close to the beam line and halo muons originating from upstream proton beam interactions are rejected through their characteristic pattern of energy deposition in the calorimeter.

- Cosmic muons traversing the ZEUS detector usually behave like minimum ionizing particles and therefore deposit energy uniformly along a straight line through the calorimeter. There are cases however when the muon can radiate a photon via bremsstrahlung and leave an energy deposit in the EMC section of the calorimeter which are therefore not vetoed by such algorithm. Cosmic rejection algorithms [94] have been developed and applied at the trigger and the offline level. The basic principles of these algorithms are summarised below. An event is selected as a cosmic candidate if any one of the following conditions applies:

  1. If the majority of the calorimeter energy deposits and hit cells belongs to the candidate.

  2. If a straight line can be fitted through the hit cells and the reconstructed tracks match that line.

  3. If there is a timing mismatch between the upper and lower half of the calorimeter and if the cell position is strongly correlated with the cell time.

Cosmic radiation events can nevertheless remain unidentified, specially if they overlap with a physics event; their contribution to the final sample is estimated by scaling the observed number of events occurring in empty bunches with the ratio of paired to empty bunches.

6.1.2 Photoproduction background

The quantity δ, defined as the total energy of the event minus the total longitudinal momentum of the event,

$$\delta = (E - p_z)_{tot} \simeq \sum_i E_i (1 - \cos\theta_i)$$

(where i runs over the measured calorimeter cells and the cell's polar angle θ is measured from the event vertex) is a conserved quantity. For a fully contained event, with an electron scattered inside the calorimeter volume, δ is equal to twice the incoming electron energy, i.e. 55 GeV:

$$(E_{tot} - P_{z\,tot})_{final} = (E_{tot} - P_{z\,tot})_{initial} = (E_p + E_e) - (E_p - E_e) = 2E_e.$$

A cut on this quantity can therefore be used to remove proton beam-gas and photoproduction events and to reduce the fraction of initial state radiation (ISR) events in the DIS sample. The characteristic δ values for these processes are listed below:

- Proton beam-gas events which originate inside the detector leave energy deposit predominantly in the forward region, resulting in low values of δ ($\delta < 20$ GeV) since $E \simeq p_z$.

- In photoproduction events the electron is scattered through a small angle and remains inside the beampipe. The hadronic activity in the calorimeter is wrongly identified as an electron. The value of δ for these events will be also small and therefore rejected by the same method:

$$\delta = (E_p + E_e - E_e') - (E_p - E_e + E_e') = 2E_e(1 - y).$$

- In ISR events the electron has radiated a photon before interacting with the proton and enters the vertex with lower energy. The photon, emitted predominantly collinear to the incoming electron, disappears in the beam pipe depositing no energy in the calorimeter. For such events, δ will be equal to twice the reduced electron energy $(E_e - E_\gamma)$, giving rise to a long tail in the spectrum towards lower values, therefore a cut requiring a minimum δ value will reduce the number of ISR events in the DIS selection.

$$\delta = (E_p + E_e - E_\gamma) - (E_p - E_e + E_\gamma) = 2E_e - 2E_\gamma.$$

6.2 Electron finding

The signature for DIS events is the presence of a scattered electron in the detector. Electron finding algorithms have been developed to single out the energy depositions associated with the final state electron. The pattern recognition is primarly based on the difference in shower profile between electrons and hadrons: an electron initiated shower is expected to deposit most of its energy in the electromagnetic section of the calorimeter and, in addition, not to spread significantly in a direction transverse to the incoming particle direction. This simple picture is however modified for example if the scattered electron interacts with inactive material and starts showering before entering the calorimeter; once the electron is correctly identified its energy can be corrected through the use of presampling devices such as the SRTD. In some regions of x and Q^2 the scattered electron direction is very close to the current jet direction and it has to be identified within the hadronic shower. Finally electromagnetic showers from π^0 decays in the calorimeter can be mistaken for low energy electrons. For this analysis the *Sinistra* electron finder [99] has been used and the systematic checks performed with a second finder, *Eexotic* [103].

Sinistra uses the idea of *islands* for clustering calorimeter cells. An arrow is drawn from each cell pointing to its immediately adjacent cell with the highest energy. If around one cell there is no other cell with higher energy, the arrow points to the same cell that it starts from. In this way all the cells in an area pointing to the highest energy cell are collected into an island. The identified islands which are "electromagnetic-like" are selected and submitted to a neural network for classification. The neural net was trained on MC, for both electron and hadronic clusters. *Eexotic* uses a cone algorithm to build clusters and physical considerations (such as energy spread around the seed cell, ratio of electromagnetic to hadronic deposition and isolation) to pick up the best candidate.

The quality of a particular algorithm can be estimated through the quantities efficiency and purity which are defined as:

$$\text{efficiency} = \frac{\text{Number of found electrons}}{\text{Number of generated electrons}},$$

$$\text{purity} = \frac{\text{Number of correctly found electrons}}{\text{Number of found electrons}}.$$

The quantities are determined from MC simulation. While the efficiency rises slowly with energy and reaches values of $\sim 100\%$ around 20 GeV for both electron finders, the purity has a sudden drop below 5 GeV, due to low energy electromagnetic clusters produced by π^0s being falsely identified as electrons. A cut on the scattered electron energy is therefore imposed ($E_e > 8$ GeV) on both data and MC.

6.3 DIS event selection

The data used in the LPS analysis correspond to an integrated luminosity of 908.8 nb^{-1}. The DIS events are selected online by a three level trigger and subsequently by a set of offline cuts [102].

6.3.1 Trigger

At the first level (FLT) the three main triggers for 1994 data taking were:

- RCAL Isolated electron trigger (ISoe): selects isolated electrons in RCAL. It was put in coincidence with a REMC threshold of 3.75 GeV after run 9693.

- REMC trigger: selects electrons in RCAL above a certain threshold excluding the towers around the beam pipe. Threshold of 2 GeV or 3.4 GeV were used depending on the run range.

- BEMC trigger: selects electrons in the BCAL with a threshold of 4.8 GeV.

The thresholds have been tuned to give a reasonable efficiency for scattered electrons with calorimeter energies ≥ 5 GeV.
At the second level (SLT) the main DIS branch was an .OR. of the first level triggers. A second branch was designed to keep very high Q^2 events where the electron is scattered in the FCAL

and is therefore not selected by the above mentioned triggers, in this case the SLT required also an .OR. together with the condition $E_T > 25$ GeV, where E_T is the total transverse energy of the event. A third branch was kept separate and prescaled for photoproduction background studies (lower $E - p_z$ cut, at 15 GeV, for fitting the $E - p_z$ distribution). Common to all branches were loose calorimeter timing cuts and *spark* rejection algorithms. A *spark* results from the sudden discharge between a calorimeter PMT and its shielding. The resulting signal appears in only one of the two PMTs reading the cell, thereby giving rise to a large imbalance between the two PMTs which can be used for their removal. *Spark* algorithms with tighter cuts were also applied at the TLT level and in the offline selection.

At the third level trigger (TLT) the main branch used in the following analysis was:

- An .OR. of the FLTs mentioned above together with an $E - p_z > 35$ GeV and an electron (.OR. of the Local and Elec5 electron finders) with an energy greater than 4 GeV.

For a certain period of data-taking the RCAL-box trigger was not working in one of the towers (module 11) around the beam-pipe. This resulted in a reduced efficiency for triggering an electron in this tower, although the event could still be triggered by the hadrons in the event. A cut on the impact point of the electron [100] on the RCAL face was made to exclude the affected region, as shown in Fig 6.2. With the same procedure the area corresponding to a dead photomultiplier below the beam pipe was excluded from the entire run range. The run dependence of this cut is reproduced in the Monte Carlo by weighting the events with the relative luminosity with which the problem occured in real data. Runs where a second photomultiplier (above the beam pipe) failed to work were excluded from this analysis.
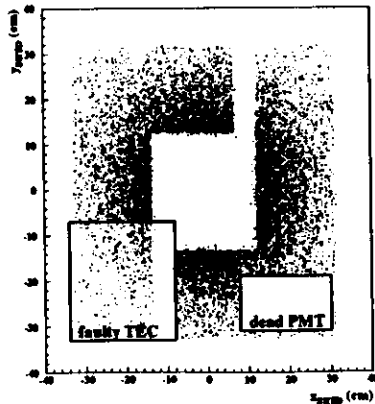
Figure 6.2: Scattered electron impact position as reconstructed for events selected by the SRTD fiducial cuts described above.

6.3.2 Uranium noise

A cut on the energy of isolated cells is applied in order to contain the effect of uranium induced noise on the reconstruction of the kinematic variables [104, 105]. The energy threshold was determined by looking at random triggers with no colliding beams. The calorimeter energy will be centered at around 0 GeV with some spread, with values varying for the electromagnetic and hadronic sectors. The thresholds applied were 80 MeV for electromagnetic and 120 MeV for hadronic cells together with an imbalance cut for cells with energy less then 700 MeV. The noisy cells were eliminated before reconstructing the kinematic variables.

6.3.3 Selection cuts

The DIS selection cuts are the standard cuts used for the structure function analysis in 1994 [106]:

- DST bit 21 is required to be set, corresponding to the trigger selection described above together with stricter timing cuts to reject beam-gas background, cosmics and halo muons and a $E - p_z + 2 * E_{lumi\gamma}$ cut of 35 GeV.

- An electron was required to be found by the *Sinistra* electron finder with a probability cut above 0.9.

- The electron energy was corrected using the SRTD information inside the area covered by the SRTD [101] ($|x + 1| < 32cm$, $|y| < 32cm$), outside energy corrections were used for the calorimeter. A cut on the corrected energy of 8 GeV was then applied.

- The electron position was reconstructed using the SRTD.
  The position reconstruction is reliable in the square $|x + 1| < 32cm$, $|y| < 32cm$.
  A shift of the CAL/SRTD position was observed by comparing data and Monte Carlo (6 mm for the right side, 4 mm for the left side). A correction was therefore applied to the data.
  The measurements of the scattered electron energy and angle are affected by the position of the electromagnetic cluster in the calorimeter. In particular at the edges of the calorimeter around the RCAL beampipe the electron shower is not fully contained, such that energy leakage inside the beampipe will result in a biased reconstruction of both the electron energy and angle. Therefore a box cut around the beam pipe region of $|x_{elec} - x_{vtx} + 1| > 13cm$ .OR. $|y_{elec} - y_{vtx} + 0.3| > 13cm$ was applied. An extra space of 1cm from the two SRTD gaps was excluded.
  In regions outside the SRTD the calorimeter was used to reconstruct the electron position. Approximately 85% of the data have a SRTD reconstructed electron.

- In the event that no vertex was reconstructed, the vertex was set to the average value of $x_{vtx} = 0.15 cm$, $y_{vtx} = -0.15 cm$ and $z_{vtx} = 3 cm$. No cut was applied on the vertex position.

- The $E - p_z$ of the event was required to be between 35 and 60 GeV.

- y_{JB} cut: although the Jacquet-Blondel method (JB) is not used for reconstructing directly the kinematics of the event (for the reconstruction of the kinematical variables

refer to the following chapter), the calculation of the hadron scattering angle γ used in the double angle method (DA) is based on the JB variables, i.e. $(E - p_z)_A$, p_{TA}. Events with low values of γ have a poor resolution in γ and are strongly affected by uranium induced noise in the calorimeter. Consequently in the analysis a cut $y_{JB} > 0.03$ was applied. The y_{JB} in the Monte Carlo was properly smeared with additional noise to reproduce the data distribution.

- A cut on $y_e < 0.8$ was applied to remove two classes of events:

  1. Firstly, photoproduction events, where a low energy hadronic deposit in the calorimeter is falsely identified as an electron leading to large y ($y > 0.9$) values.

  2. Secondly, ISR events, the cross section for which is peaked at high y_e.

- A cut on Q^2 greater then $4 GeV^2$ for both the electron and the double-angle method was applied.

- A tight timing cut on the absolute RCAL and FCAL time and on the absolute difference of the average FCAL and RCAL times was applied to suppress proton beam-gas background. The cut was placed at 6 ns i.e.:

$$|t_{FCAL} - t_{RCAL}| < 6ns \, and \, |t_{RCAL}| < 6ns, \, |t_{FCAL}| < 6ns.$$

6.4 LPS diffractive event selection and background

In order to select a clean sample of diffractive deep inelastic events, the following cuts were applied on the LPS detected proton:

- If more then one track per event is reconstructed, the one which crosses the highest number of planes is selected. If two tracks cross an equal number of planes, the one with the lowest χ^2/dof is chosen.

- The fractional longitudinal momentum of the proton $x_L > 0.95$ in order to adequately separate the diffractive peak. Non diffractive deep inelastic events with a high momentum leading particle in the proton fragmentation cone are exponentially suppressed, as shown in Section 4.2. Moreover a cut at 0.95 restricts the measurement to a region of flat LPS acceptance in the (x_L, p_T) plane and ensures that, after integration over t, the resultant acceptance in x_L is largely independent of the t distribution (Fig 6.3). This condition is essential for the determination of any t-integrated measurement, such as $F_2^{D(3)}$. An upper cut on x_L of 1.02 (corresponding to 5 σ assuming $\sigma_{x_L} = 0.4\%$) was applied to reject unphysical events.

- For each track a minimum distance of approach to the beam pipe of $500\mu m$ was required to reject events where the proton could have hit any the beam pipe wall and showered. This cut will be referred to as the Δ_{Pipe} cut (see Fig. 5.17).

- The χ^2/dof of the track was required to be less then 10.

- A cut on the total $E + 2*p_z$ of the event (> 1655 GeV) was performed to eliminate halo protons reconstructed by the LPS in coincidence with DIS events triggered by ZEUS (this cut is described in detail in the section below).
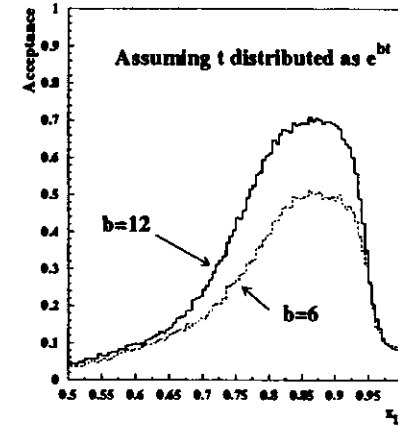
6.4.1 Halo protons

Halo protons represent one of the main sources of background in the spectrometer, originating principally from the interaction of beam protons with either the residual gas inside the beam pipe or the proton beam collimators. These tracks have energy close to the proton beam energy and can give a spurious $x_L = 1$ signal in the LPS in coincidence with an ep interaction triggered by the central detectors. Since there is no correlation (for these events) between the LPS and the ZEUS triggered physics event, the total hadronic energy measured in the event is not necessarily conserved. An equivalent of the $E - p_z$ variable in the forward direction i.e. $E + p_z + 2*p_z^{LPS}$ where E and p_z are measured by the calorimeter and p_z^{LPS} is associated with the proton can be used to cut out such events. If the event is fully contained this quantity should be equal to $2 * E_p$, i.e. 1640 GeV, whereas proton beam halo events tracked by the LPS could exceed this value. A tail of high $E + p_z + 2*p_z^{LPS}$ events is indeed observed in the data (Fig 6.4) and an upper cut of 1655 GeV (accounting for the resolution of the measured p_z^{LPS}) is applied. The number and distribution of halo events with $E + p_z + 2*p_z^{LPS} < 1655$ GeV is estimated in the following way:

- The p_z^{LPS} distribution for unphysical events ($E + p_z + 2*p_z^{LPS} > 1655$) and the calorimeter $E + p_z$ distribution for general DIS events are sampled randomly to create a $E + p_z + 2*p_z^{LPS}$ distribution for random DIS halo coincidences.

- The observed data distribution is fitted as a weighted sum of a diffractive MC (RAP-GAP) and the random coincidences $E + p_z + 2*p_z^{LPS}$ distributions whose absolute normalisation is kept as a free parameter (Fig 6.5). Given the weight of the latter, the percentage of random coincidences below 1655 GeV is estimated to be $3.5 \pm 0.6\%$.
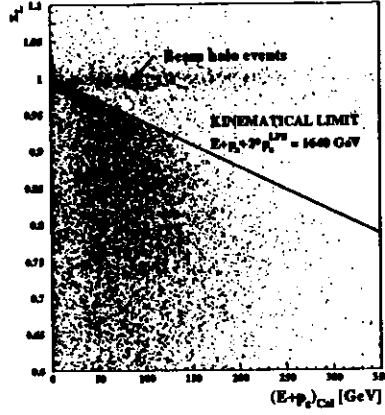
Figure 6.4: $E + p_z$ vs z_L for the data which shows a clear band of events at $z_L = 1$ uncorrelated with the value of $E + p_z$ as measured by the calorimeter.

These events can then be used as a sample of beam halo events and be statistically subtracted from any physics distribution.

6.4.2 DIS non diffractive background

Since in the measured x, Q^2 range the total deep inelastic cross section is estimated to be about ten times larger then the diffractive one, it is important that the background from non diffractive "normal" deep inelastic events is kept small. In deep inelastic $\gamma^* - p$ scattering the struck parton is deflected and it emerges from the proton remnant at an angle θ. The difference in pseudorapidity η between the struck parton and the proton remnant is given by:

$$\Delta\eta = \eta_{proton\ remnant} - \eta_{parton} \sim ln(\frac{W}{m_p}) - ln(\frac{xW}{m_p}) \sim ln(\frac{1}{x}),$$

where $\eta_{parton} = -ln(tan(\frac{\theta}{2}))$. Due to the colour string connecting the struck parton and the proton remnant the rapidity gap will be filled with particles in the hadronization process. The multiplicity of these hadrons $< n_h >$ increases faster then the longitudinal size of the gap,

$$< n_h > \geq \Delta\eta \sim ln(\frac{1}{x}).$$

If we assume a Poisson distribution, the probability w_{DIS} of having no particles in the gap will be very small,

$$w_{DIS} \sim e^{-<n_h>} < x,$$

in contrast with the same probability for diffractive events which is almost x independent. It is possible to estimate the survival probability for deep inelastic non diffractive events to
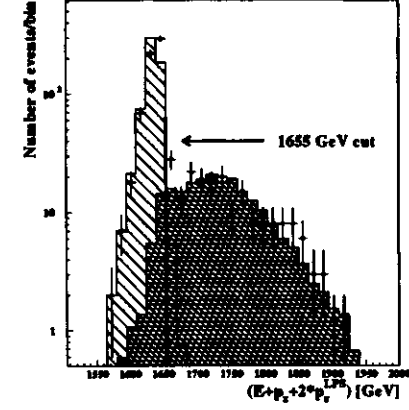
Figure 6.5: The $E + p_z + 2 * p_z^{LPS}$ distribution of data (dots) as a sum of diffractive MC (RAPGAP in light grey) and randomly sampled halo events (dark grey).

the requirement of a LPS high x_L proton by studying the x_L spectra of DIS MC events. Fig 6.6 shows the reconstructed x_L distribution for non diffractive DIS events generated with ARIADNE (described in chapter 4) after the DIS and all but the x_L LPS cuts. The distribution is centered at $x_L \sim 0.7$ and the contamination to the region of proton momentum $0.95 < x_L < 1.02$ is negligible.

6.4.3 Double dissociation diffractive contamination

The contribution from diffractive processes where the nucleon dissociates into a state of mass M_N:

$$ep \to e' + X + N$$

can be estimated by Monte Carlo simulation. In this analysis the EPSOFT MC has been used (see chapter 4 for a detailed description). The generation is based on a parametrization of the hadronic cross section $\sigma(pp \to pN)$ at the centre of mass energy W and incorporates a nucleonic mass spectrum of the form $1/M_N^2$. In Fig. 6.6 the four components, single dissociation, double dissociation, pion exchange and DIS non diffractive, are fitted to the observed data x_L distribution and their relative weights are established. An upper bound to the double dissociative cross section has been imposed from the pp scattering estimated ratio of single to double cross section ($\sigma_{SD}/\sigma_{DD} \simeq 1.3$ at $< W > \sim$ 100GeV, upper bound for the fit $\sigma_{SD}/\sigma_{DD} = 2$). The contamination fraction is given by:

$$C = \frac{N_{DD}(0.95 \leq x_L \leq 1.02)}{N_{Tot}(0.95 \leq x_L \leq 1.02)} \approx 5\%, \tag{6.1}$$

Figure 6.7: (a) x_L spectrum of $\eta_{max} < 1.5$ data events. (b) fraction of $\eta_{max} < 1.5$ events for a double dissociative MC (EPSOFT) as a function of x_L.

6.4.4 Pion exchange

At a first glance the main contribution to the $x_L < 1$ spectrum can be attributed to secondary reggeons exchange. The pion exchange MC, with small corrections due to ρ exchange (whose cross section is ten times smaller) gives by itself an accurate description of the observed data distribution below $x_L = 0.9$. Estimates for the f-exchange admixture to the cross section exist only in hadron-hadron scattering [107] and there is no reason to expect this term to be the same in deep inelastic scattering. The f structure function could be β-dependent and its intercept up to $\alpha_f \approx 0.76$, leading to a noticeable contribution in the high x_L region. The relevant diagrams for pion exchange are shown in Fig. 6.8 where the second process, known as Deck effect, accounts for those events which have a large rapidity gap in the final state. It must be noted that these large rapidity gap events at low x_L constitute a non negligible and kinematically biased source of background to the analysis based on the large rapidity gap requirement rather than the proton tagging. The contamination to the $x_L > 0.95$ region for pion exchange is determined by the combined fit in the same way as for the double dissociation and the result is of the order of 6%. ρ exchange has not been included in the fit and could lead to small variations in the final result.

6.4.5 Beam gas

The beam gas contamination has been estimated by looking at the number of events which passed the selection cuts from the p-pilot bunches, and by rescaling this number with the ratio $N p - pilot\ bunches / N\ ep\ bunches$ (see section 6.1.1). This contribution has been found to be negligible.

6.4.6 Effect of the cuts

The reduction factor on the data sample for each of the cuts applied is given in Table 6.1. There is however an overlap between some of the cuts as shown in the second column, for example photoproduction fake electrons are removed either by the low electron energy cut or by the δ-cut, unphysical protons in the LPS fail both the $E + p_z + 2 * p_z^{LPS}$ and the upper

---

Figure 6.6: Reconstructed (and therefore strongly shaped by the LPS acceptance) x_L distribution. a) data (dots) are fitted as a weighted sum of a DIS non diffractive MC (ARIADNE), a double dissociative MC (EPSOFT), a pion exchange MC (HERWIG) and a diffractive MC (RAPGAP). b) the sum of the four abovesaid MC is plotted (hatched area) against the data (dots).

where $N_{DD}(0.95 \leq x_L \leq 1.02)$ is the number of double dissociative events in the distribution shown in Fig. 6.6 with $x_L > 0.95$ and $N_{Tot}(0.95 \leq x_L \leq 1.02)$ is the total number of events in the sample. The value for the absolute normalisation of the double dissociative cross section obtained from the fit indicates that double diffractive dissociation is indeed a small component of the total cross section at $x_L < 1$. This is confirmed by the observation that the x_L data distribution presents a dip (Fig. 6.7a) in the interval (0.9-0.95) whenever the η_{max} of the events is required to be < 1.5, while the ratio of events with $\eta_{max} < 1.5$ is essentially flat as a function of x_L for a double dissociative MC (Fig. 6.7b), thus allowing little room for a double dissociative contribution to the whole spectrum.

Figure 6.8: (a) Pion exchange and (b) Deck effect.

x_L cut.

The x, Q^2 regions most affected by the DIS cuts are shown in Fig. 6.9 (where the kinematical variables have been reconstructed with the electron method, see chapter 7). Assuming the proton kinematics can be factorized out, the LPS cuts influence uniformly the x, Q^2 plane and their effect on the proton phase space x_L, p_T are shown in Fig. 6.10. After the application of all the cuts 626 events remain for the analysis.

Cut	Reduction after this cut	Reduction after all previous cuts	Events after all previous cuts
DST and LPS activity	100%	100%	16831
box cut	53.3%	53.3%	8978
δ cut	92.9%	52%	8752
E_e cut	77.5%	51.7%	8694
y_e cut	77.6%	51.5%	8671
timing cut	98.3%	50.8%	8551
y_{JB} cut	78.3%	37.7%	6350
Q^2 cut	60.2%	33.6%	5650
upper x_L cut	98.2%	33.1%	5574
lower x_L cut	21.5%	6.5%	1104
Δ_{Pipe} cut	87.2%	5.2%	870
χ^2/dof cut	78.5%	4.8%	808
$E + p_z + 2 * p_z^{LPS}$ cut	72%	3.7%	626

Table 6.1: Summary of the final selection
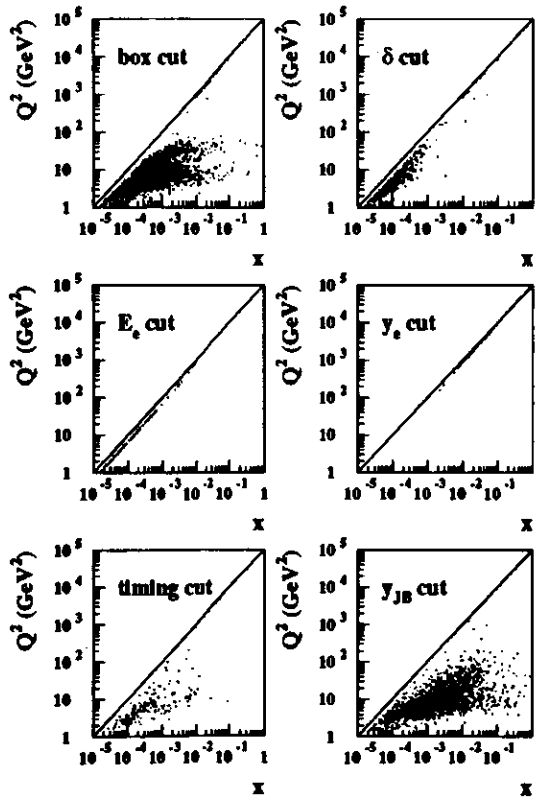
Figure 6.9: The x, Q^2 distribution of events removed by the various DIS cuts. Two bands can be observed in the x, Q^2 distribution of events rejected by the box cut, corresponding to the events rejected by either the inner SRTD or the inner calorimeter box cut.
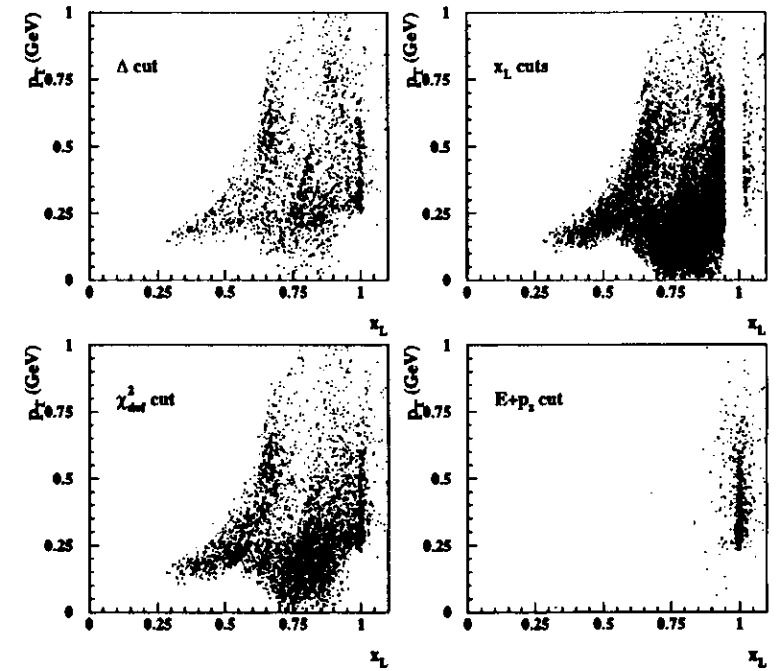
Figure 6.10: The x_L, p_T distribution of events removed by the various LPS cuts.

Chapter 7

Reconstruction of kinematics

The measurement of the deep inelastic diffractive cross sections relies on the accurate reconstruction of the kinematical variables characterizing the deep inelastic interaction, namely x and Q^2, as well as on the reconstruction of the kinematic variables describing the emission of a pomeron by the proton. While x and Q^2 are reconstructed from the scattered electron and the hadronic deposition in the ZEUS calorimeter, the proton kinematics (x_L and t) is measured by the ZEUS leading proton spectrometer. The variables x, Q^2, x_L and t are then combined to determine the quantities characterizing the diffractive scattering. The reconstruction methods and the accuracies obtained are described in the following sections.

7.1 Reconstruction of DIS kinematic variables

The deep inelastic scattering variables x and Q^2 can be determined either by measuring the angle (θ_e) and the energy of the scattered electron (E_e') (see Fig. 7.1) as done in fixed target experiments, or, since at HERA the hadronic system is detected, by measuring the energy (F) of the current jet (i.e. the struck quark in the quark-parton model) and its direction (γ), or by using any combination of these four quantities [96]. In the following sections the formula and experimental details for the reconstruction of the kinematical variables are presented.

7.1.1 Electron method

From the energy and the angle of the scattered electron the kinematics is determined by the equations,

$$y_e = 1 - \frac{E_e'}{2E_e}(1 - \cos\theta_e), \tag{7.1}$$

$$Q_e^2 = 2E_e E_e'(1 + \cos\theta_e), \tag{7.2}$$

$$x_e = \frac{E_e E_e' \cos^2(\theta_e/2)}{E_p(E_e - E_e' \sin^2(\theta_e/2))}. \tag{7.3}$$

Substituting θ_e or E_e from eq. 7.3 into eq. 7.1 the equations of contours of constant scattered electron energy and angle are obtained as:

$$Q^2(x, E) = \frac{sx\left(1 - \frac{E_e'}{E_e}\right)}{1 - \frac{xE_p}{E_e}}, \tag{7.4}$$
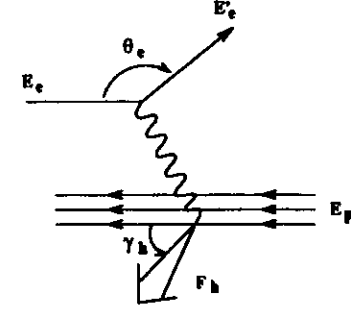
$$Q^2(x, \theta) = \frac{sx}{1 + \frac{xE_p}{E_e}\tan^2\frac{\theta_e}{2}}. \tag{7.5}$$

The scattered electron energy and angle isolines in the (x, Q^2) phase space are shown in Fig. 7.2a,b. The resolution in x and Q^2 is in general good in regions of phase space where the E_e' and θ_e isolines are close toghether, whereas for isolines far apart, small errors in the measurement of E_e' and θ_e produce large uncertainties in x and Q^2 so that very high energy resolution is needed. The dependence of the reconstructed x_e and Q_e^2 on the relative errors of the scattered electron energy and angle is given by:

$$\frac{\sigma_{x_e}}{x_e} = \sqrt{\left(\frac{1}{y_e}\right)^2\left(\frac{\sigma_{E_e'}}{E_e'}\right)^2 + \left[-\tan\frac{\theta_e}{2} + \left(\frac{1}{y_e} - 1\right)\cot\frac{\theta_e}{2}\right]^2 (\sigma_{\theta_e})^2}, \tag{7.6}$$

$$\frac{\sigma_{Q_e^2}}{Q_e^2} = \sqrt{\left(\frac{\sigma_{E_e'}}{E_e'}\right)^2 + \tan^2\frac{\theta_e}{2}(\sigma_{\theta_e})^2}. \tag{7.7}$$

As can be seen from Fig. 7.2a, the resolution of the electron method is good for low values of x. At high x the energy and angle isolines are almost parallel to the x axis, so their measurement does not constrain the value of x. Fig. 7.3a shows the fractional deviations of the measured x and Q^2 from their true values as a function of x, Q^2 and y. The distance of each point from zero gives the average bias whereas the error bar shows the mean spread of the measured points. The resolution in x is overall worse than the one in Q^2, due to the $1/y$ factor that amplifies the error on the energy measurement (particularly at low values of y) and it is indeed deteriorating with increasing x. At high y (i.e. large electron scattering angles θ_e) both the x and the Q^2 measurement are dominated by the angle measurement. The resolution in x is typically of the order of 40% but can reach 100% values in the above mentioned regions. The Q^2 resolution is below 20% over the all range. The use of the SRTD for the event by event correction of the scattered electron energy improves the resolution on the energy measurement $\frac{\sigma_{E_e'}}{E_e'}$ and therefore the reconstruction of the kinematics with the electron method.
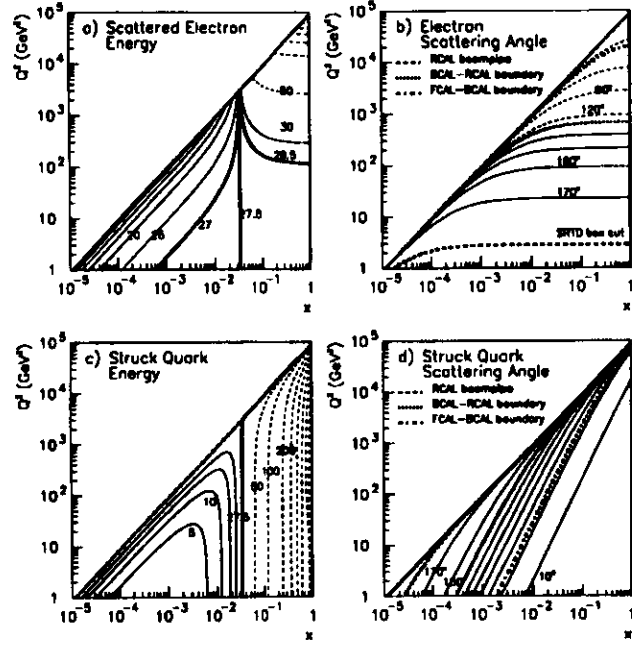
Figure 7.2: Isolines in energy and scattering angle of the electron and struck quark in the x, Q^2 plane. Intrinsic good resolution is achieved if the isolines are close together since measurement error in E'_e, θ_e, F and γ lead to small uncertainties on x and Q^2. The diagonal straight line represents the kinematical limit $y = 1$.

7.1.2 Jacquet-Blondel method

The event kinematics could be in principle be reconstructed from the current jet energy (F) and direction (γ). However, in order to avoid any dependence of the extracted variables from the final state fragmentation, separation between the current and remnant jets and sensitivity to particle losses along the forward beam direction, the transverse momentum of the hadronic system p_{TA} and the difference between the energy and the z component of the hadron flow $(E - p_z)_h$ are used. The remnant jet gives a small contribution to the above variables as it is mostly lost in the forward beam pipe. The reconstruction method based on the above quantities (JB) was developed by Jacquet and Blondel [91] and it has to be used when the scattered lepton is not detected, e.g. in charged current deep inelastic events or photoproduction events where the electron is not detected in the LUMI. Since the remnant jet is lost in the beam pipe, the transverse momentum p_{TA} and the difference $(E - p_z)_h$ of the hadron flow are approximately equal to those of the current jet, p_{Tj} and $(E - p_z)_j$. The
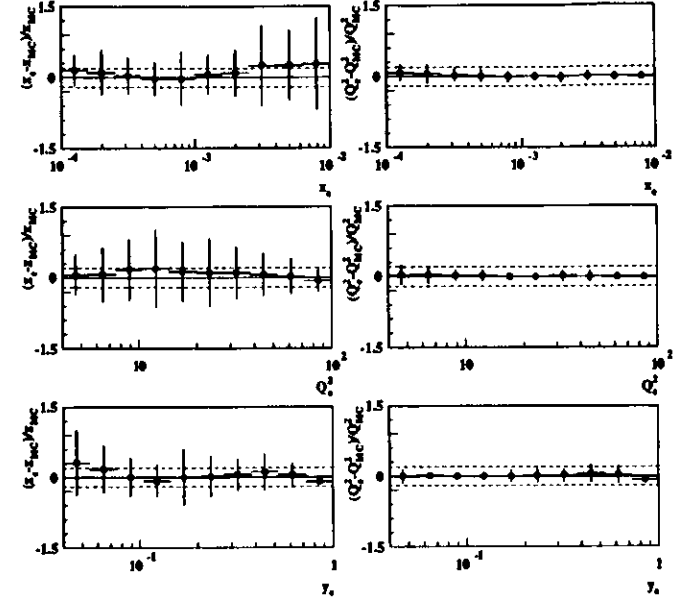
Figure 7.3: Fractional resolutions of x and Q^2 as a function of x, Q^2 and y for the electron method. The dashed horizontal lines indicate deviations of $\pm 20\%$ from zero.

current jet energy (F) and angle (γ) can be reconstructed from p_{TA} and $(E - p_z)_h$ as follows:

$$p_{TA} \sim p_{Tj} = F\sin\gamma, \tag{7.8}$$

$$\sum_h (E - p_z)_h \sim (E - p_z)_j = F(1 - \cos\gamma), \tag{7.9}$$

where:

$$p_{TA} = (\sum_k p_{x_k})^2 + (\sum_k p_{y_k})^2$$

and the sums over h run over all final state hadrons.
The defining formulae for the kinematical variables are:

$$y_{JB} = \frac{\sum_h (E_h - p_{z_h})}{2E} = \frac{F(1 - \cos\gamma)}{2E_e}, \tag{7.10}$$

$$Q^2_{JB} = \frac{(\sum_i p_{x_i})^2 + (\sum_i p_{y_i})^2}{1 - y_{JB}} = \frac{F^2\sin^2\gamma}{1 - y_{JB}}, \tag{7.11}$$

$$x_{JB} = \frac{Q_{JB}^2}{sy_{JB}}. \tag{7.12}$$

The contours of constant scattered jet energy and angle for the Jacquet-Blondel method are given by:

$$Q^2(x, F) = \frac{sx\left(1 - \frac{F}{xE_p}\right)}{1 - \frac{F}{xE_p}}, \tag{7.13}$$

$$Q^2(x, \gamma) = \frac{sx}{1 + \frac{E_e}{xE_p}\tan^2\frac{\gamma}{2}}. \tag{7.14}$$

The scattered jet energy and angle isolines are shown in Fig. 7.2c,d. In contrast to the electron method, resolution in x, as determined from the scattered jet energy, is good at high values of x while it deteriorates at lower x. The dependence of x_{JB} and Q_{JB}^2 on the measurement errors of the scattered jet energy F and angle γ is given by:

$$\frac{\sigma_{x_{JB}}}{x_{JB}} = \sqrt{\left(\frac{1}{1-y_{JB}}\right)^2 \left(\frac{\sigma_F}{F}\right)^2 + \left[-\tan\frac{\gamma}{2} + \left(\frac{y_{JB}}{1-y_{JB}}\right)\cot\frac{\gamma}{2}\right]^2 (\sigma_\gamma)^2}, \tag{7.15}$$

$$\frac{\sigma_{Q_{JB}^2}}{Q_{JB}^2} = \sqrt{\left(\frac{2-y_{JB}}{1-y_{JB}}\right)^2 \left(\frac{\sigma_F}{F}\right)^2 + \left[2\cot\gamma + \left(\frac{y_{JB}}{1-y_{JB}}\right)\cot\frac{\gamma}{2}\right]^2 (\sigma_\gamma)^2}. \tag{7.16}$$

The resolution in x for low y values depends only on the scattered jet energy measurement. At high y, the resolution in x becomes poor, due to the $1/(1-y)$ term, in contrast with the electron method. The Q^2 resolution also deteriorates with increasing y. The resolution in x is poor at both low and high values of γ, while the resolution in Q^2 is affected by the error on the scattered jet angle only at low values of γ.

7.1.3 Double-Angle method

The double angle (DA) method uses the angles θ_e and γ of the final state electron and final state hadron flow, respectively. The direction of the hadronic energy flow can be defined, in terms of p_{Th} and $(E - p_z)_h$, as:

$$\cos\gamma = \frac{(\sum_h p_{x_h})^2 + (\sum_h p_{y_h})^2 - (E - p_z)_h}{(\sum_h p_{x_h})^2 + (\sum_h p_{y_h})^2 + (E - p_z)_h}. \tag{7.17}$$

As eq. 7.17 shows, particles with small p_T moving along the proton direction give negligible contribution and therefore there is no need, in the reconstruction of γ, to remove particles belonging to the proton remnant fragmentation[1]. Since $\cos\gamma$ is constructed as the ratio of the quantities characterizing the hadron flow, it is consequently independent of fluctuations in the energy measurement of the hadron flow. The equations for the DA kinematics are:

$$Q_{DA}^2 = 4E^2 \frac{\sin\gamma(1 + \cos\theta_e)}{\sin\gamma + \sin\theta_e - \sin(\theta_e + \gamma)}. \tag{7.18}$$

---

[1] The contribution is in fact negligible with respect to other sources of uncertainty, such as the calorimeter noise, after applying a lower cut on y_{JB} (i.e. $y_{JB} > 0.03$) which excludes the kinematical region with maximum sensitivity to the proton fragmentation.

$$x_{DA} = \frac{E(\sin\gamma + \sin\theta_e + (\sin(\theta_e + \gamma))}{P_s\sin\gamma + \sin\theta_e - (\sin(\theta_e + \gamma))}. \tag{7.19}$$

Since the DA formulae do not contain energy explicitly they are at first order independent of errors in energy measurements. The resolution and bias for x and Q^2 measured with the DA method are shown in Fig. 7.4. A feature common to both the electron and the double angle
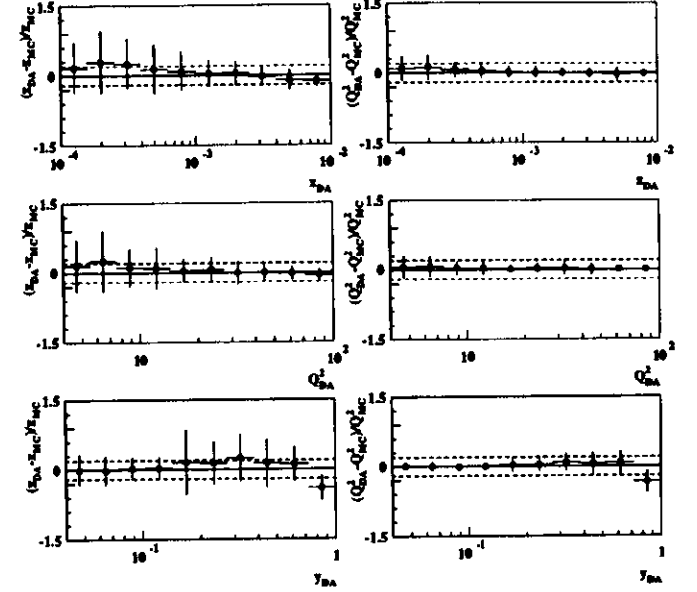
Figure 7.4: Fractional resolutions of x and Q^2 as a function of x, Q^2 and y for the double angle method. The dashed horizontal lines indicate deviations of $\pm 20\%$ from zero.

methods is that both the resolution and bias in x is larger than for Q^2. In particular regions the resolution in x reaches values above 50% while the Q^2 resolution is lower than 20% over the entire range of the measurement. The electron method has been chosen as the primary reconstruction method for this analysis.

7.2 The kinematic distributions in Data and MC

The distribution of the z position of the primary vertex is used to set the absolute normalization of the MC. The MC vertex distribution has been reweighted in order to correctly sample

the data distribution for the limited range of runs used in the LPS analysis. The diffractive MC used for the comparison are NZ and RAPGAP. By normalizing the MC sample to the same luminosity of the data the absolute normalization predicted by NZ appears to be 30% larger[2], which is compatible with the errors estimated by the authors (chapter 4). A cut on the reconstructed hadronic mass M_X is applied ($M_X^2 > 10 GeV^2$) above the generation limit of the NZ MC ($M_X^2 > 3 GeV^2$) in order to take into account migration effects in the reconstruction. Fig. 7.5 shows the distributions for the z vertex position, the corrected energy and the angle of the scattered electron and y_{JB}. The W distribution (data and MC) is shown in Fig. 7.15.
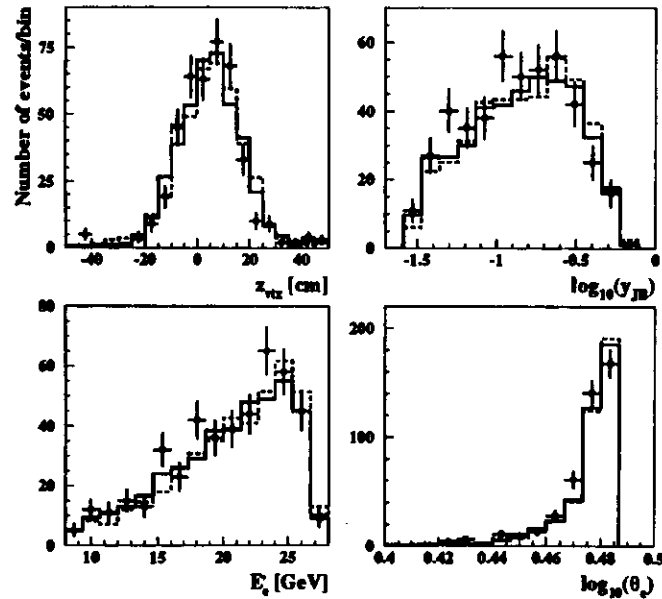
Figure 7.5: Data (dots) and MC (solid line for RAPGAP and dashed line for NZ) distributions of the z vertex position, the corrected energy and the angle of the scattered electron and y_{JB}

The δ distribution for data and MC is shown in Fig. 7.6. Although the electron energy has been corrected, the difference between the inactive material configuration in ZEUS and

---

[2]This does not take in account the contribution of background events, such as halo protons or double dissociative events, which can be overall of the order of 15 − 20%, thus decreasing the disagreement between data and the single dissociation NZ MC

---

its simulation program affects the hadrons which give a big contribution to $E - p_z$ at high y thus resulting in all the energies being shifted towards lower values in the data compared to the MC. The stronger disagreement between the data and the NZ MC is due to the absence of radiative corrections, which are not included in the simulation of the NZ model. The tail to lower values of δ present in the data and not in the NZ MC corresponds to ISR events. A δ-cut therefore affects differently the data and MC. The sensitivity to the choice of the cut and these differences are treated in the systematic error.
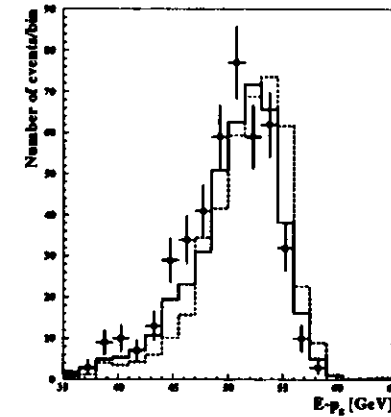
Figure 7.6: The $E - p_z$ distribution for data (dots) and MC (solid line for RAPGAP and dashed line for NZ). a stronger disagreement can be observed for the NZ MC which does not contain ISR events. For both MCs differences exist as a result of the hadrons response to the disagreement on the inactive material configuration between the detector and its simulation.

The x and Q^2 determined with the electron method are shown in Fig. 7.7.

7.3 Reconstruction of DIS diffractive variables

7.3.1 x_L and t

From the cartesian components of the proton momentum measured by the LPS the fraction of longitudinal momentum carried by the scattered proton can be calculated (in the approximation that p_x and p_y are small compared to p_z) as :

$$x_L = p_z/820. \tag{7.20}$$

P_x and p_y give the proton transverse momentum, $p_T = \sqrt{p_x^2 + p_y^2}$, from which t is reconstructed as:

$$t = -\frac{1}{x_L}p_T^2 \left[1 + (M_p^2/p_T^2)(x_L - 1)^2\right]. \tag{7.21}$$
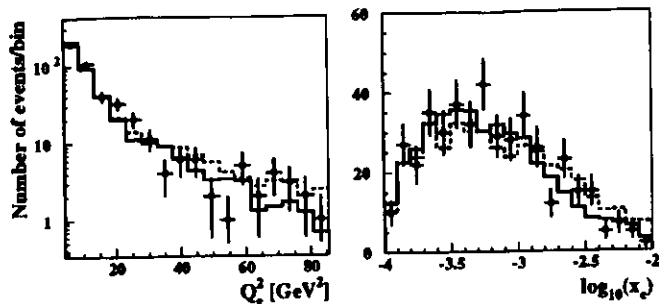
Figure 7.7: The Q^2 and x data distributions (dots) in comparison with the MC (solid line for RAPGAP and dashed line for NZ) prediction

The p_T and x_L resolutions have already been discussed in the previous chapter while the resolution and acceptance in t will be discussed in detail in chapter 8. Fig. 7.8 shows the t and x_L data distributions compared to the MC. The x_L scale was corrected for the systematic shift (0.09%) introduced by aligning the tracks in the vertical plane with diffractive photo-production data where the calorimeter was used to determine x_L (see chapter 5). Due to uncertainty in the motor positioning ($\sim 50\mu m$) the data x_L spectrum is broader then the MC one. Additional smearing ($\sim 40\%$) was added to the MC to match the resolution determined from the data of photoproduction ρ's at $x_L = 1$.
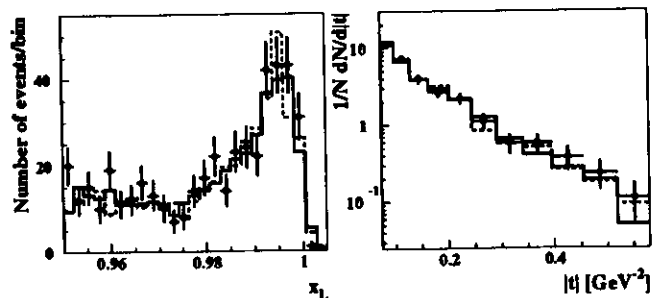
Figure 7.8: The t and x_L data distributions (dots) are compared with the MC (solid line for RAPGAP and dashed line for NZ) prediction

7.3.2 The hadronic mass M_X

All the variables characterizing diffractive scattering (Fig. 7.9) can be determined either from the hadronic energy deposited in the calorimeter and the scattered electron kinematics or from the LPS detected proton and the electron. The event is selected if it has a reconstructed track in the LPS according to the quality requirements described in the previous chapter and the hadronic mass M_X is reconstructed using either one of the two following reconstruction methods.
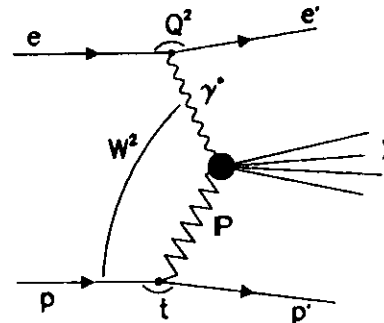
Figure 7.9: Diagram of a deep inelastic diffractive event

Method one (TA)

When the system X is fully contained, its invariant mass, M_X, can be determined from the calorimeter cell information as follows. If the energy, momentum and polar angle of the final hadronic system are denoted by E_H, p_H and θ_H, respectively and $\vec{p_i}$ as the vector constructed from the energy E_i, the polar angle, θ_i, and the azimuthal angle, ϕ_i, of cell i; then:

$$\cos\theta_H = \frac{\sum_i p_{zi}}{|\sum_i \vec{p_i}|}, \tag{7.22}$$

$$p_H^2 = \frac{Q_e^2(1 - y_e)}{\sin^2\theta_H},$$

$$E_H = p_H \cos\theta_H + 2E_e y_e,$$

from which M_X is determined by the definition $M^2_{X\,TA} = E^2_H - p^2_H$. This method is hereafter referred as "triple angle" method, since it relies on the measurement of θ_H, θ_e and γ (defined in eqn. 7.17). The "triple angle" M_X resolution is approximately 40% and independent of M_X. The reconstruction of M_X with this method is affected both by energy loss in inactive material in front of the calorimeter and by errors in the position determination of the hadrons. Monte Carlo studies show that (Fig. 7.10) M_X is systematically shifted by 10% to lower values. In order to compensate for this shift, a correction factor of 1.1 is applied to the measured mass whenever the TA reconstruction is used.

χ^2/ndf	5995. / 57
Constant	198.4
Mean	-0.1059
Sigma	0.3703
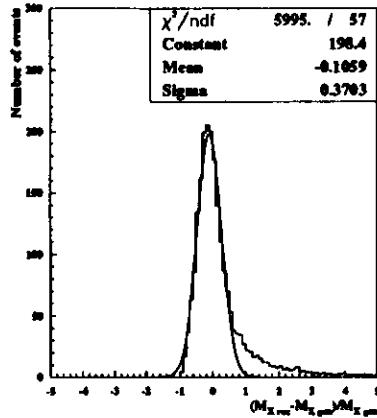
Figure 7.10: M_X reconstruction with the TA method. The width of the distribution gives the resolution on the measured M_X while its mean value shows the systematical shift.

Method two (LPS)

M_X can be completely reconstructed from the proton and electron kinematics using:

$$M^2_X = (1 - x_L)(W^2 + Q^2 - m^2_p) - Q^2 + t, \qquad (7.23)$$

where, in this analysis, x and Q^2 have been determined from the electron method. It is therefore independent of the calorimeter hadronic energy scale.

From the above formula one can see that:

$$\frac{\sigma_{M^2_X}}{M^2_X} \sim \frac{\sigma_{x_L}}{(1 - x_L)}, \qquad (7.24)$$

such that the error on the mass reconstruction method becomes large as $x_L \to 1$ (region of low masses).

It is therefore convenient to use either one of the two reconstruction methods by checking the relative error on the mass reconstruction on an event by event basis. Neglecting m^2_p and assuming t is small (the latter is a good approximation since t has to be less then 1 GeV in order to be within the LPS acceptance, for values of the mass above few GeV) eq. 7.23 can be rewritten as:

$$M^2_X = sy(1 - x - x_L), \qquad (7.25)$$

leading to an error on the M^2_X determination of:

$$\sigma_{M^2_X\,LPS} = \sqrt{(s(1 - x_L))^2 \sigma^2_y + (sy)^2 \sigma^2_{x_L}}, \qquad (7.26)$$

where:

$$\sigma^2_y = \frac{1}{E_e}[(\sigma^2_{E_e}\sqrt{E'_e})^2 (\frac{1 - cos\theta_e}{2})^2 + \sigma^2_{\theta_e}(\frac{E'_e sin\theta_e}{2})^2)]$$

is the error on y coming from the measurement of the scattered electron energy and angle with errors σ_{E_e} and σ_{θ_e} respectively. $\sigma^2_{x_L}$ at $x_L = 1$ has been estimated to be 0.4% from the width of photoproduction ρ^o. σ_{E_e} and σ_{θ_e} are measured by the SRTD and their average values are, respectively, $0.26\sqrt{E'_e}$ and $2mrad$. No corrections are applied to M_X as determined by the LPS.

Criteria for the combined M_X reconstruction method

The criteria to select the mass reconstruction method on an event by event basis are the following:

- If $\frac{\sigma_{M^2_X}}{M^2_X}$ is less than 50% and $\frac{|M_{X\,TA} - M_{X\,LPS}|}{M_{X\,TA}} < 1$: $M_{X\,Rec} = M_{X\,LPS}$.

- If $M^2_{X\,LPS}$ is bigger then $10GeV^2$: $M_{X\,Rec} = M_{X\,LPS}$.

- If the previous two conditions do not occur: $M_{X\,Rec} = M_{X\,TA}$.

Fig. 7.11 shows the regions of mass covered by the two reconstruction methods if one applies the above selection conditions to the MC. The mass resolution as a function of the mass value is shown in Fig. 7.12. The resolution, given by the error bars, is below 20% over the entire M_X range. In the region where the LPS gives a reliable measurement (towards high M_X) the mean value of the reconstructed mass agrees well with the generated one. The resolution in M_X using the LPS alone (eq. 7.25) varies from 25% at $M_X = 5GeV$ to 6% at $M_X = 80GeV$. The M_X distribution for data and MC is shown in Fig. 7.15.

Fig. 7.13 illustrates the range in M_X and W covered by the diffractive events selected by this analysis compared with the region populated by the DIS non diffractive events. Diffractive events are distributed rather uniformly in W. DIS non diffractive events extend to larger hadronic masses, due to the large hadronic energy associated with the proton fragmentation in the forward direction.

7.3.3 β and x_{IP}

From M_X, Q^2 and x the variables β and x_{IP} are determined as follows (neglecting t):

$$\beta = \frac{Q^2}{Q^2 + M^2_X}, \qquad (7.27)$$
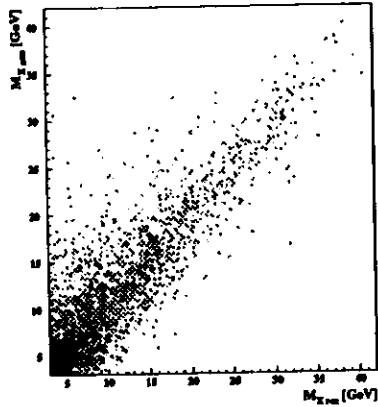
Figure 7.11: Generated versus reconstructed M_X, the black dots are events where the mass is reconstructed from the triple angle formula while the grey dots correspond to events with a LPS reconstructed mass. The general trend is that low masses are better reconstructed by the TA method and high masses by the LPS method.

$$x_{IP} = \frac{x}{\beta}. \qquad (7.28)$$

The fraction of the generated events which pass the selection cuts as a function of β is shown in Fig. 7.14 where a distinction is made for events with a TA (solid line) or a LPS (dashed line) reconstructed mass. The TA method tends to cover the low M_X region (therefore high β values) while the LPS method populates the high M_X (low β) region. Fig. 7.15 shows that the β and x_{IP} data distributions are in very good agreement with the MC predictions. The resolution of these variables will be considered in detail in chapter 9.

7.3.4 η_{max}: the maximum pseudorapidity

The maximum pseudorapity of an event, η_{max}, is defined as the maximum value of pseudorapidity of all calorimeter condensates (i.e. the pseudorapidity of the hadronic deposit closest to the outgoing proton direction) with energy greater than 400 MeV or alternatively of a track with momentum $> 400 MeV/c$. The presence of events with a rapidity gap between the hadronic final state and the outgoing proton is a signature of a diffractive interaction. A cut on η_{max} was used in the analysis of 1993 data (as discussed in chapter 9), when the LPS was not available, to isolate diffractive events. Fig. 7.16a shows the η_{max} distribution for data and the NZ MC while in Fig. 7.16b the data are compared with the sum of a single (NZ) and a double (EPSOFT) dissociation MC, with the relative weights as determined by the fit to the x_L distribution described in chapter 6.

The disagreement, which still exists after taking into account background contributions, such as double dissociation events, might be explained if one considers that the current MC
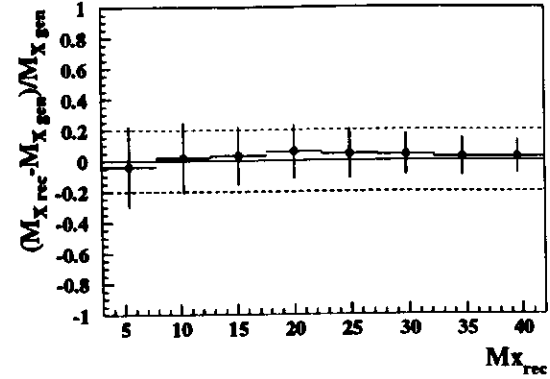
Figure 7.12: The mean value of the difference between measured and generated M_X as a function of M_X. The vertical error bars represent the RMS.

implementation of the Nikolaev Zakharov model does not contain the fragmentation of the $q\bar{q}g$ fluctuations of the photon although it contains the appropriate parametrisation for the cross section and it is therefore missing a class of events present in the data. Similar conclusions can be drawn from the comparison of the data with the RAPGAP MC (see Fig. 7.17a,b).

The distribution of DIS events in the η_{max}, x_L plane (Fig. 7.18) clearly shows a band of diffractive events at high values of x_L extended over a wide η_{max} range, well separated from the main bulk of proton fragmentation events which populate the region at low x_L and high η_{max} values.
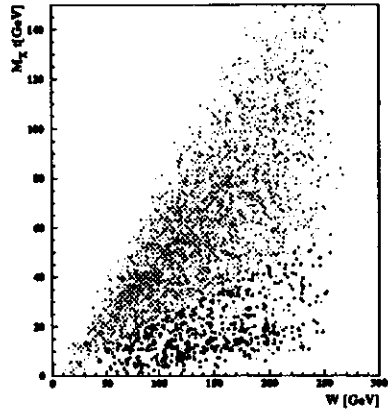
Figure 7.13: M_X vs W. The gray dots are DIS non diffractive events while the black dots represent the events selected in the diffractive analysis.
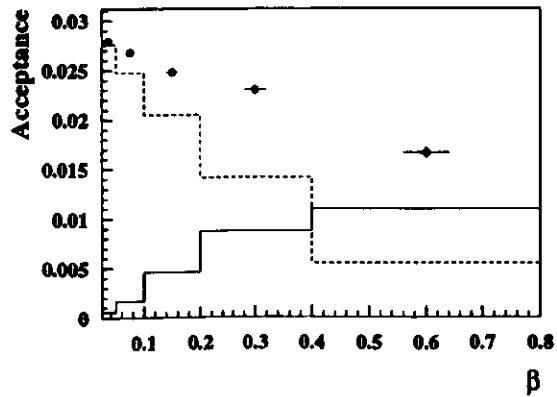
Figure 7.14: Acceptance of the selection cuts as a function of β. The acceptance for events with a TA reconstructed M_X is shown as a solid line while the acceptance for events with a LPS reconstructed M_X is shown by the dashed line
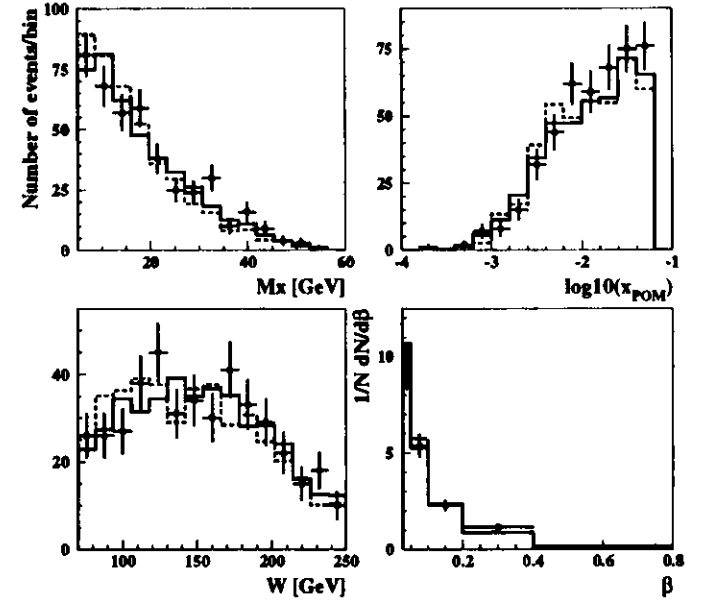
Figure 7.15: The M_X, W, β and x_{IP} data distributions (dots) in comparison with the MC (solid line for RAPGAP and dashed line for NZ).
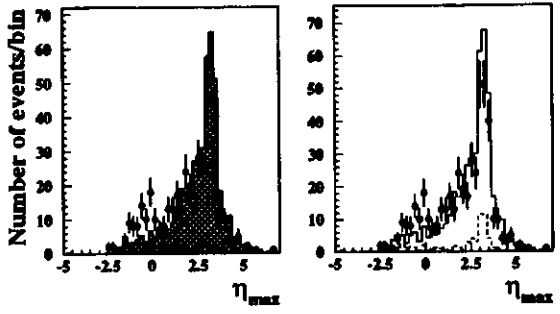
Figure 7.16: The η_{max} data distribution (dots) in comparison a) with the NZ MC (solid) prediction, b) with a sum of the NZ and EPSOFT (contribution shown as a dashed line) MC, relative weights as determined by the fit to the x_L distribution in chapter 6.
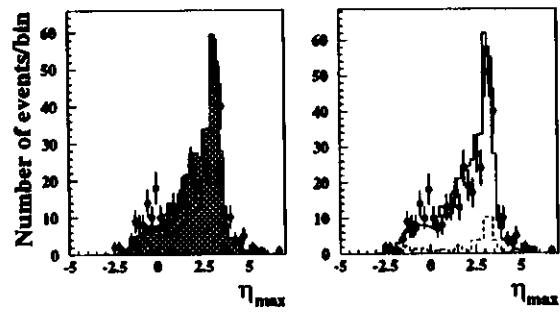
Figure 7.17: The η_{max} data distribution (dots) in comparison a) with the RAPGAP MC (solid) prediction, b) with a sum of the RAPGAP and EPSOFT (contribution shown as a dashed line) MC, relative weights as determined by the fit to the x_L distribution in chapter 6.
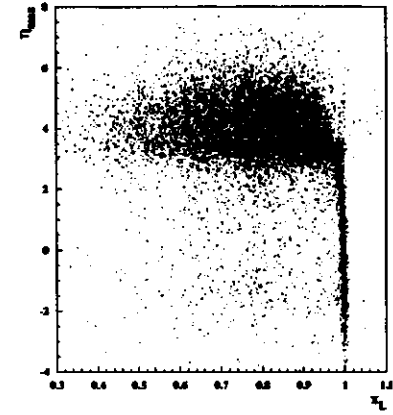
Figure 7.18: η_{max} vs x_L for DIS events, the band at high x_L values which runs over the whole range of η_{max} values correspond to diffractive events.

Chapter 8

Measurement of $d\sigma/d|t|$

The first measurement of the t dependence of the deep inelastic diffractive cross section is presented here. The detection of the forward scattered proton with the LPS allows to select a sample of events with a low estimated fraction of background processes, both from diffractive excitations of the forward proton and from other Reggeon exchanges rather than pomeron exchange.

8.1 Acceptance

The acceptance in transverse momentum p_T and therefore t is limited by the geometrical acceptance of the LPS [44, 83]. The LPS acceptance is determined by the geometry of the beam pipe and by the shape (principally the elliptical cut) of the silicon μ-strip detectors. Since the detector planes cannot be positioned in the beam, the acceptance vanishes towards $p_x = p_y = 0$ (i.e. small values of p_T and t). For 100% efficient detectors, $x_l = 1$ tracks, no beam emittance and no vertex spread, the acceptance is either 0% or 100% depending on the values of p_x and p_y. The real situation of course it is not so well defined, nevertheless, at fixed x_L, there are ostensibly two large regions in the p_x, p_y phase space where the acceptance is above 50%, as shown in Fig. 8.1a,b for $x_L = 0.97$ and $x_L = 1$, respectively.

The p_T acceptance is obtained by performing an integral over the polar angle in the p_x, p_y plane. Since the integration spans over unmeasurable regions the resulting acceptance in p_T is rather low ($\simeq 6\%$ at high x_L). The region of geometric acceptance larger than 95% for both $p_X > 0$ and $p_X < 0$ maps into that of $0.25 \lesssim p_T \lesssim 0.65$ GeV and is not used in the present analysis. As mentioned in chapter 7, a lower cut on x_L is applied to isolate diffractive events thus restricting the measurement to a x_L, p_T region of reasonably flat acceptance, see Fig. 8.2. For the diffractive events selected with $x_L > 0.95$, p_T varies from $0.2 GeV^2$ to $0.8 GeV^2$.

The p_x and p_y distributions of the events which pass the selection cuts described in chapter 7 are shown in Fig.8.3 compared to the predictions of two diffractive MCs. The agreement between data and MC simulation shows to be reasonably good in both variables.

8.1.1 Run dependence

The LPS acceptance depends on the position of the detectors during data taking (see chapter 5). Consequently run-by-run correction factors were applied to correct the data back to the
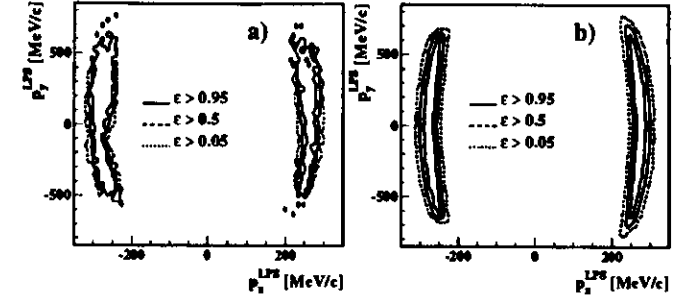
Figure 8.1: Geometrical LPS acceptance for tracks with a) $x_L = 0.97$ and b) $x_L = 1$ in the p_x, p_y plane. There are two distinct regions where the acceptance goes from zero to values above 95%. The plot has been obtained with the use of the standalone program BEAM9, which includes the effects of multiple scattering and the vertex spread.

fixed detector configuration simulated in the MC. In the LPS simulation program the stations have been positioned according to the values of a particular run which corresponds to the closest position to the beam (highest acceptance) ever reached by the LPS during the year. Assuming that the spectrometer acceptance is factorizable into the product of two terms, the first representing the geometrical acceptance and the second the efficiency of the track reconstruction algorithm, and that the latter is independent of geometry variations such as the detectors positioning, then a correction factor can be extracted [108] by comparing the geometrical acceptance of every run configuration with the one simulated in the Monte Carlo. This has been done with the use of the standalone program BEAM9 [84] and a weight was assigned to each event as a function of the kinematical variables x_L and p_T and the run number. The mean value of the weights as a function of p_T and x_L is shown in Fig. 8.4 and Fig. 8.5. There is not a significant dependence on p_T or x_L and the values are above unity, since the simulated run corresponds to farthest insertion position of the detectors into the beam and therefore to the maximum acceptance ever reached during the 1994 data taking. To evaluate to the systematic error on the determination of $d\sigma/d|t|$ arising from the uncertainty in the evaluation of the acceptance for each individual run, an event by event weighting factor was also applied to the data before the acceptance corrections.

8.1.2 Resolution and bin selection

The resolution on the t measurement is dominated by the intrinsic transverse momentum spread of the incoming proton beam and is therefore proportional to the square root of the beam emittance. An estimate of this dispersion can be derived from a class of processes, namely elastically photoproduced ρ^0 (see chapter 5), where the x and y components of the scattered proton momentum can be measured either directly from the LPS or indirectly by reconstructing the vector meson transverse momentum in the CTD (which in the limit $Q^2 \approx 0$ balances the outgoing proton momentum). A gaussian fit to the distribution of the final state total momenta, obtained as a sum of the x and y momentum components as measured by
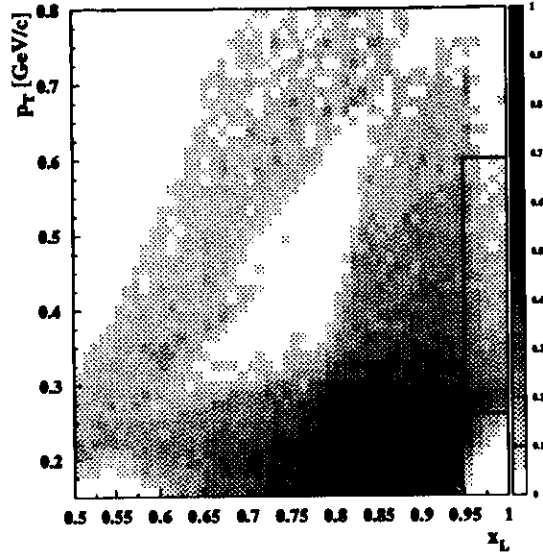
Figure 8.2: Geometrical LPS acceptance in the x_L, p_T plane for two or three stations coincidences. The solid line encloses the kinematical region used for the comparison of the kinematic distributions in chapter 6.

the LPS and the CTD (Fig. 8.6), gives a RMS which is consistent with the estimate for the emittance of the proton beam given by HERA [109] ($\sigma_{p_x} \simeq 40 MeV/c$ and $\sigma_{p_y} \simeq 90 MeV/c$).

The bin width in $|t|$ has been chosen such that the width is larger than the resolution in $|t|$:

$$\Delta|t| \geq \sigma(|t|). \qquad (8.1)$$

The effect of the intrinsic beam spread is approximately constant over the measured p_T range and is of the order of $90 MeV/c$. Since the t resolution is proportional to $1/\sqrt{(|t|)}$ (see eq. 8.21) the bin sizes have been chosen proportional to $\sqrt{(|t|)}$. In order to avoid regions where the acceptance varies rapidly, values of $|t| < 0.07 GeV^{-2}$ have been excluded from the fit. A minimum requirement on the population of each bin fixes an upper limit of $0.4 GeV^{-2}$. The resolution values range from 20% to 30% for the selected bins (Fig. 8.7a). The purity of each bin, evaluated by means of the MC simulation and defined as the fraction of the events reconstructed in one bin which were generated in the same bin, is plotted in Fig. 8.7b and gives an estimate of the migration effects present in the measurement of t. The purity decreases with $|t|$ due to the stronger migration of events from the higher populated bins towards the lower ones.
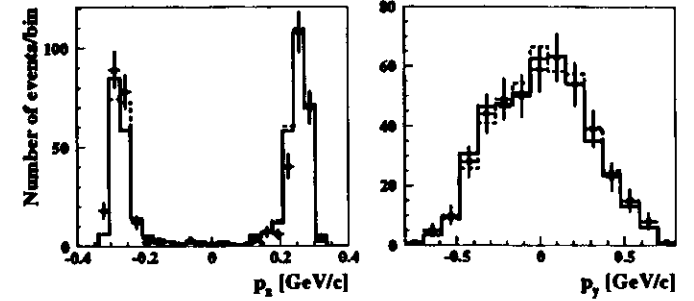
Figure 8.3: Data (dots) and MC (solid line for RAPGAP and dashed line for NZ) distributions of the proton p_x and p_y.

8.2 t dependence of background events

For the extraction of $d\sigma/d|t|$ the analysed range in x_L has been restricted to values of x_L in the range $0.97 < x_L < 1.02$ in order to keep the contamination of background events from double dissociation or pion exchange below a 5% level. The t dependence of proton beam halo events is discussed below.

Halo Events

In order to have a rough estimate of the dependence upon t of the cross section for beam gas and beam halo interactions it is possible to use directly the CERN ISR data on inclusive proton spectra in $p - p$ collisions [110], due to the fact that the centre of mass energy for HERA protons colliding with a gas nucleon is in the range covered by the ISR. Fig. 8.8 shows the t dependence of ISR events classified as elastic and events classified as inelastic. Assuming a single exponential behaviour, the slope of the total inclusive cross section in proximity to the elastic peak is $\approx 6 GeV^{-2}$, compatible with the range of predictions for $\gamma^* - p$ diffractive events.

This ansatz can be validated by comparing the t dependence of beam halo events with that of physics events. For this purpose the data sample of unphysical events which are rejected by the cut on $E + p_z + 2 * p_t^{LPS}$ is used (see chapter 7). The ratio of the observed t distributions for events with $E + p_z + 2 * p_t^{LPS} > 1655 GeV$ and $E + p_z + 2 * p_t^{LPS} < 1655 GeV$ is shown if Fig 8.9 and indicates, with the caveat that the acceptance in x_L and p_T for physics and background processes is similar and therefore cancels out, that the t slope for beam halo events is reasonably close to that of DIS diffractive events. The absolute value of the cross section is therefore affected by this source of background but no significant influence is expected on the t-slope.
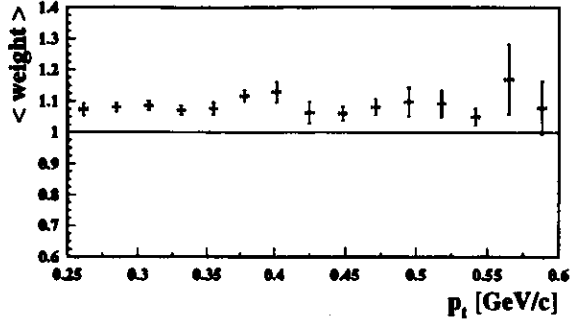
Figure 8.4: Mean weight of the events as a function of p_T. This factor has been applied to the data to correct for the run by run dependence of the acceptance due to the positioning of the LPS detectors. The value is constantly above unity, since the simulation is based on the highest acceptance conditions reached during the 1994 data taking
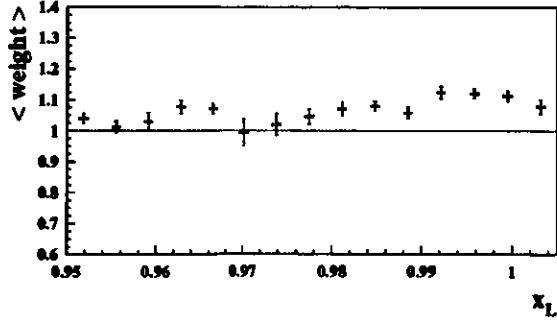
Figure 8.5: Mean weight of the events as a function of x_L.

8.3 The differential cross section $d\sigma/d|t|$

Fig. 8.10 shows the differential cross section $d\sigma/d|t|$ for $4GeV^2 < Q^2 < 30GeV^2$, $70GeV < W < 210GeV$, $0.02 < \beta < 0.4$ and $x_L > 0.97$. The upper cut on β was chosen in order to remove the region where the cross section for exclusive vector meson production is enhanced[1]. Moreover the diffractive MCs used to calculate the acceptance corrections (both NZ and RAPGAP) have a generation limit of $M_X \gtrsim 1GeV$, which excludes the region of small masses (equivalent according to eq. 8.27 to the region of high β values). The data selected within the above mentioned kinematical range were subdivided into bins of t and the cross section was evaluated using:

---
[1]Using 1993 data [111], the p_T^2 dependence of the cross section for exclusive ρ^0 production in deep inelastic scattering was fitted to an exponential form, yielding a result for the slope parameter of $5.1^{+1.2}_{-0.9}(stat.) \pm 1.0(syst.)$

114
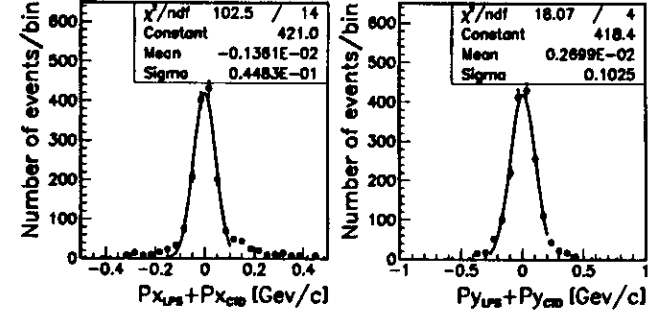
Figure 8.6: Intrinsic momentum spread of the proton beam. A gaussian fit to the data distributions gives a RMS consistent with the emittance values quoted by the HERA machine group ($\sigma_{p_x} \simeq 40MeV/c$ and $\sigma_{p_y} \simeq 90MeV/c$). The transverse momentum resolution of the CTD for this class of events is $\sigma(p_T)/p_T \simeq 0.03$ while the intrinsic resolution of the LPS apparatus (as shown in chapter 5) is $\sigma(p_T)/p_T \simeq 0.02$. The dominant effect in the above distributions is therefore due to the beam spread.

$$\sigma_i(\gamma^*p \rightarrow Xp) = \frac{N_i}{L\epsilon_i}, \tag{8.2}$$

where N_i is the number of observed events in bin i, L is the total integrated luminosity and ϵ_i is the MC estimated acceptance[2]. A fit of the form:

$$d\sigma/d|t| = A \cdot e^{bt} = A \cdot e^{-b|t|} \tag{8.3}$$

was performed, giving for the parameters A and b the following result:

$$A = 38 \pm 8^{+5}_{-3}\, nb \cdot (GeV)^{-2}, \tag{8.4}$$

$$b = 5.9 \pm 1.3^{+0.54}_{-0.68}\, (GeV)^{-2}, \tag{8.5}$$

where the first error is statistical from the fit and the second error is systematic and it was evaluated according to the prescription described in the following section. The values of the cross section in each of the fitted bins, together with the average t values, the statistical and systematic error, the number of observed events, and the MC estimated acceptance ϵ with the relative error $\delta\epsilon$, are given in Table 8.1.

In a Regge-type description, the slope of the exponential t distribution in single diffractive interactions is predicted to be given by the relation $b \simeq b_0 + 2\alpha' \ln(W^2/M_X^2 + Q^2)$. The value of b_0 has been fitted from hadron-hadron data to be $\simeq 4.5GeV^{-2}$; the value of α' is equal to 0.25 for a soft pomeron. The measured value is compatible with the predicted value for a soft pomeron exchange.

The measured differential cross section was integrated over the range $0.073 < |t| < 0.36GeV^2$, yielding:

$$\sigma = 3.5 \pm 0.6^{+0.9}_{-0.8}\, nb \tag{8.6}$$

---
[2]The RAPGAP Monte Carlo event sample has been used for determining the acceptance

114

114
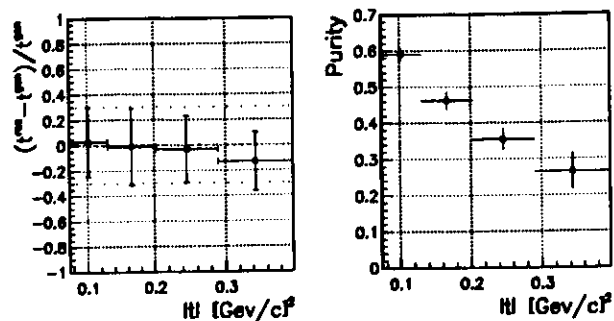
Figure 8.7: (a) Fractional deviation of the measured $|t|$ from its true value as a function of $|t|$. The distance of each point from zero gives the average bias whereas the error bar shows the mean spread of the measured points. The dashed horizontal lines indicate deviations of $\pm 30\%$ from zero. (b) Estimated purity in each bin.

$<|t|>$	$d\sigma/d|t|$	$stat.$	$sys.$	N_{obs}	$\epsilon \pm \delta\epsilon$
0.098	21.6	2.2	$+1.3$ -1.2	100	0.076 ± 0.003
0.161	14.9	2.1	$+1.1$ -1.6	50	0.044 ± 0.003
0.228	9.1	1.9	$+3.9$ -0.2	23	0.032 ± 0.003
0.319	6.8	2	$+0.3$ -0.9	11	0.013 ± 0.002

Table 8.1: Summary of the $d\sigma/d|t|$ results.

for $4GeV^2 < Q^2 < 30GeV^2$, $70GeV < W < 210GeV$, $0.02 < \beta < 0.4$ and $x_L > 0.97$. The total DIS cross section integrated over the same Q^2 and W range, using as input structure function the ZEUS fit to the 1994 F_2 data, amounts to 95nb. The cross section predicted by the Nikolaev and Zakharov model, as implemented in the NZ MC, for the measured region of Q^2, W, β, t and x_L is of the order of $\simeq 5nb$.

8.3.1 Systematic checks

The systematic checks are summarized in Table 8.2. They can be subdivided into three groups: selection and reconstruction of a deep inelastic event in ZEUS, selection and reconstruction of a diffractive proton in the LPS, and stability of the fit with regard to the choice of the binning, unfolding procedure, MC input to the acceptance corrections and run to run variations in the LPS acceptance. The estimate of some of the systematic uncertainties (which entail for example a tighter selection cut) is strongly affected by the statistics limitation of the data sample. The biggest contribution to the systematic error to the slope parameter b comes from a variation of the lower x_L cut which increases its value of about half a unit. This can be understood in terms of background processes such as π, ρ and f exchange which yield a slope parameter $b \sim 10GeV^{-2}$ and have cross sections comparable to that of single diffraction in the region $0.95 < x_L < 0.97$. As mentioned in chapter 7 there are no models
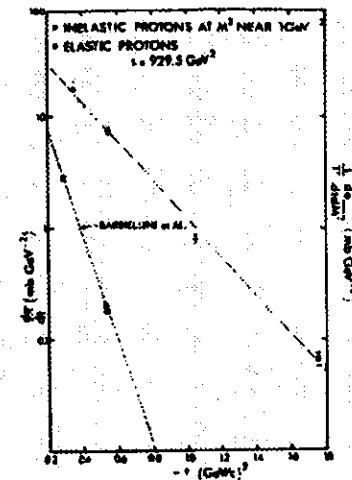
Figure 8.8: Closed circles: differential cross section versus t for elastically produced protons in pp collisions at the CERN ISR. Open circles: invariant differential cross section versus t at values of the missing mass squared $M^2 \approx 1.0 GeV^2$. Solid line: elastic scattering data at $s = 929.5 GeV^2$ (Barbiellini et al.) .The dotted line is drawn to guide the eye.

to predict the entity of the f exchange cross section and structure function in deep inelastic scattering. Unlike the π exchange, depending on the value of the intercept, the contribution from f and the other reggeons increases with x_L. Moreover, if the f and $I\!P$ structure functions have different β-dependence, the fraction of secondary reggeon exchange in the selected sample will be a function of β. Overall most of the checks yield results which agree with the standard method within the statistical errors. The estimate of the systematic error on the cross section normalisation parameter A does not include the checks which require a variation of the kinematical boundaries. The biggest contribution to the uncertainty on the determination of A comes from the run to run variations of the LPS acceptance due to the detectors positioning. As mentioned beforehand, the detectors configuration implemented in the MC used for the acceptance corrections corresponds to the highest geometric acceptance achieved during 1994 data taking (run 9720). The value of A is therefore underestimated unless the run to run acceptance corrections are applied. The total systematic on the fit parameters was obtained by summing in quadrature errors of the same sign.

In addition to the above errors, there is an overall normalisation uncertainty (therefore affecting the parameter A) of 3% due to the uncertainty in the first level trigger efficiency and to the uncertainty on the determination of the luminosity.

8.4 Systematic error due to the beam spread

The choice of the bin size in the dN/dt distribution is made requiring that the bin size is not smaller than the resolution in each bin. It has been described how this resolution is strongly affected by the beam momentum spread at the interaction point, and therefore, how

Description	Effect on A	Effect on b
$E - p_Z > 40GeV$	−4.7%	−5%
$E_e' > 8GeV$	−1.5%	−1.6%
$Q^2 > 5GeV^2$	−	−6.6%
box cut at 12 × 12 cm	−4%	+2.2%
no y_{JB} cut	+0.1%	−5.8%
$\beta < 0.3$	−	+2.8%
$\beta < 0.65$	−	−1.6%
$x_L > 0.96$	−	+6.2%
$\chi^2_{ndof} < 6$	*0%	0%
$\Delta_{Pipe} > 0.1cm$	+7%	+2.5%
$E + p_z + 2 * p_z^{LPS} < 1670GeV$	+2.5%	+0.05%
$0.25 \le p_z \le 0.3GeV$	−2.9%	−3.3%
NZ MC for corrections	+2%	+1.5%
W MC dependence reweighted to $W^{1.5}$	+3.8%	+3.3%
t MC dependence reweighted to one unit up	+2.9%	+3.3%
t MC dependence reweighted to one unit down	−0.03%	−3.8%
Bayes [112] unfolding	+9%	+1.5%
no run-by-run acceptance corrections	−14%	−2.4%

Table 8.2: Systematic checks and their effect on the fit parameters A and b, where $d\sigma/d|t| = A \cdot e^{-b|t|}$.
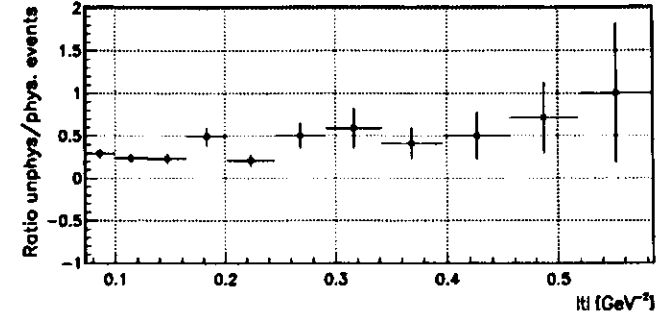
Figure 8.9: Ratio of number of unphysical events ($E + p_z + 2 * p_z^{LPS} > 1655GeV$) associated to beam halo interactions within the selection cuts to the number physical events ($E + p_z + 2 * p_z^{LPS} < 1655GeV$) as a function of t.

the number of bins used is constrained to be four. Alternatively, it is possible to calculate the slope of the dN/dt distribution not by unfolding the data taking into account the initial beam momentum spread, but rather correcting the *observed* dN/dt slope with a calculated systematic rescale. This has the advantage of reducing the smearing in each bin due to migration and therefore allows a fitting with a larger number of bins.

The t distribution of the scattered proton relative to the incident proton is a two dimensional gaussian in transverse momentum space. Also the transverse momentum of the incident beam has a two dimensional distribution and so the resultant distribution is their convolution which is also a gaussian. A fit to the data gives the slope parameter of this resultant distribution and the physically relevant parameters must then be extracted using independent information of the beam emittance. The actual situation is somewhat more complicated because the horizontal and vertical emittances differ.

Figure 8.11 shows the combination of transverse momentum vectors, with the following notation:

p_x, p_y the transverse momentum vector, p_T of the scattered proton relative to the incident beam particle.

b_x, b_y the position of the incident proton in transverse momentum phase space.

σ_x, σ_y the standard deviations of the distributions in transverse momentum phase space.

r_x, r_y the (apparent) transverse momentum of the scattered proton relative to the mean beam direction.

t the Mandelstam t parameter, $= -(p_x^2 + p_y^2)$ at the value of $x_L = 1$ which will be assumed in the following.

b the true logarithmic slope of the scattered proton t distribution.
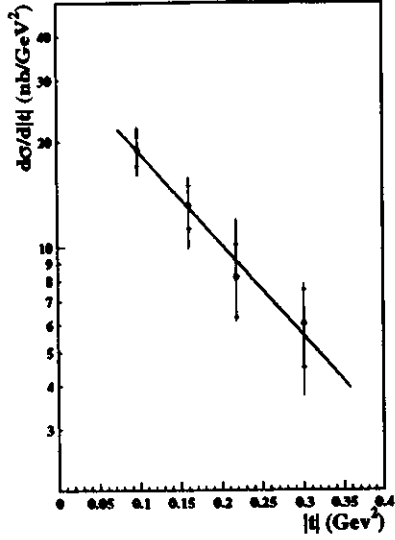
Figure 8.10: The differential cross section $d\sigma/d|t|$ for deep inelastic diffractive events in the range $4GeV^2 < Q^2 < 30Gev^2$, $70GeV < W < 210GeV$, $0.02 < \beta < 0.4$ and $x_L > 0.97$. The inner error bars are the statistical errors while the outer error bars are the statistical and systematic errors summed in quadrature.

t_{app} the apparent value of t, given by $-(r_x^2 + r_y^2)$

σ_{tot} total scattering cross section.

The normalized distribution of particles in a beam with a Gaussian spatial distribution is given by:

$$\frac{d^2 P}{db_x db_y} = \frac{1}{2\pi\sigma_x\sigma_y} \exp\left(-\frac{b_x^2}{2\sigma_x^2} - \frac{b_y^2}{2\sigma_y^2}\right). \qquad (8.7)$$

If the cross section is parametrized as:

$$\frac{d\sigma}{d|t|} = A \cdot \exp(bt), \qquad (8.8)$$

and introducing azimuthal symmetry:

$$\frac{d^2\sigma}{d\phi d|t|} = \frac{A}{2\pi} \cdot \exp(bt). \qquad (8.9)$$
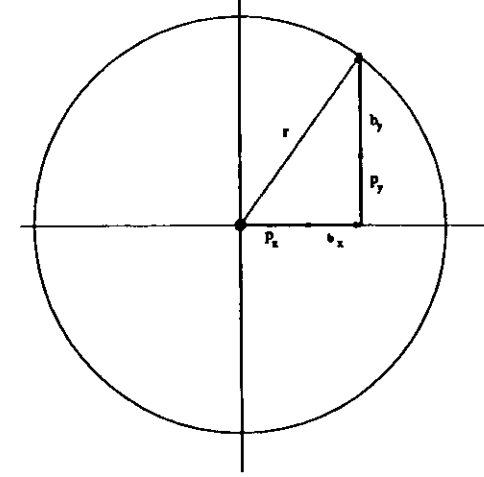
Figure 8.11: Notation and momentum vectors in the transverse plane.

Since $d\phi dt = d\phi dp_T^2 = p_T d\phi dp_T$ is the element of transverse phase space area, so can be written as $dp_x dp_y$. So the cross section can be written in its gaussian form:

$$\frac{d^2\sigma}{dp_x dp_y} = \frac{A}{\pi} \cdot \exp\left(-b(p_x^2 + p_y^2)\right). \qquad (8.10)$$

With Fig.8.11 in mind, the combined (cross section × probability) for a proton at b_x, b_y in transverse plane scattering with a change in the transverse momentum p_x, p_y is:

$$\frac{d^4\sigma}{dp_x dp_y db_x db_y} = A' \cdot \exp\left(-bp_x^2 - \frac{b_x^2}{2\sigma_x^2}\right) \cdot \exp\left(-bp_y^2 - \frac{b_y^2}{2\sigma_y^2}\right), \qquad (8.11)$$

where

$$A' = \left(\frac{\sigma_{tot} b}{2\pi^2 \sigma_x \sigma_y}\right). \qquad (8.12)$$

Changing variables such that r_x replaces b_x as the independent variable, and similarly in y, one has:

$$\frac{d^4\sigma}{dp_x dp_y dr_x dr_y} = A' \cdot \exp\left(-bp_x^2 - \frac{(r_x - p_x)^2}{2\sigma_x^2}\right) \cdot \exp\left(-bp_y^2 - \frac{(r_y - p_y)^2}{2\sigma_y^2}\right). \qquad (8.13)$$

When integrating over p_x and p_y to obtain the apparent distribution in r, the p_x and p_y parts factorize so, for the p_x factor there is an integral:

$$\int \exp\left(-bp_x^2\right) \cdot \exp\left(-\frac{(r_x - p_x)^2}{2\sigma_x^2}\right) dp_x. \qquad (8.14)$$

This is just the convolution of two gaussians with standard deviations: $\sigma_1 = \frac{1}{2b}$ and $\sigma_2 = \sigma_x$, and the result is a new gaussian with standard deviation

$$\sigma^2 = \sigma_1^2 + \sigma_2^2 = \sigma_x^2 + \frac{1}{2b}. \qquad (8.15)$$

The observed transverse momentum distribution is then:

$$\frac{d^2\sigma}{dr_x dr_y} = B \exp\left(-\frac{r_x^2}{2(\sigma_x^2 + \frac{1}{2b})} - \frac{r_y^2}{2(\sigma_y^2 + \frac{1}{2b})}\right), \qquad (8.16)$$

where

$$B = \frac{A}{\pi} \cdot \frac{1}{\sqrt{1 + 2b\sigma_x^2}} \cdot \frac{1}{\sqrt{1 + 2b\sigma_y^2}}. \qquad (8.17)$$

The $\frac{1}{2b}$ terms are at least a factor of ten greater than the σ^2 terms, it is therefore possible to write the exponent as:

$$\frac{r_x^2}{2(\sigma_x^2 + \frac{1}{2b})} \simeq b(1 - 2b\sigma_x^2)r_x^2, \qquad (8.18)$$

giving

$$\frac{d^2\sigma}{dr_x dr_y} = B \exp\left(-b(1 - 2b\sigma_x^2)r_x^2 - b(1 - 2b\sigma_y^2)r_y^2\right), \qquad (8.19)$$

or alternatively:

$$\frac{d^2\sigma}{d\phi d|t|_{app}} = \frac{1}{2} B \exp\left[bt_{app} - 2b^2 t_{app}(\sigma_x^2 \cos^2\phi + \sigma_y^2 \sin^2\phi)\right]. \qquad (8.20)$$

This equation can be rewritten in terms of t_{app} and ϕ and integrated over ϕ to obtain:

$$\frac{d\sigma}{d|t|_{app}} = \pi B \exp\left\{b[1 - (\sigma_x^2 + \sigma_y^2)b]|t_{app}\right\} \cdot I_0\left[(\sigma_y^2 - \sigma_x^2)b^2 t_{app}\right], \qquad (8.21)$$

where I_0 is the first order modified Bessel function. The properties of the Bessel polynomials, i.e. $I_0(0) = 1$ and $I_0(-x) = I_0(x)$ (for x real), indicate that the contribution of the I_0 term in eq 8.21 becomes negligible for $\sigma_x^2 \simeq \sigma_y^2$ and that there is symmetry between the x and y components. The $d\sigma/d|t|_{app}$ distribution after acceptance corrections is shown in Fig. 8.12b.

The interval $0.07 GeV^2 < |t|_{app} < 0.4 GeV^2$ has been subdivided in 6 bins of width proportional to $\sqrt{|t|_{app}}$. The purity is very high even in bins with low statistics, as shown in Fig. 8.12a. A fit to $d\sigma/d|t|_{app}$ with the functional form of eq. 8.21 has been performed, assuming that $\sigma_x = 0.04 GeV$ and $\sigma_y = 0.09 GeV$. The results for the parameters A and b are shown in Table 8.4 together with the results obtained by varying the beam emittance of $\pm 50\%$. This method gives an estimate by the systematic error due to the beam spread of 18% and 8% on the fit parameters A and b.
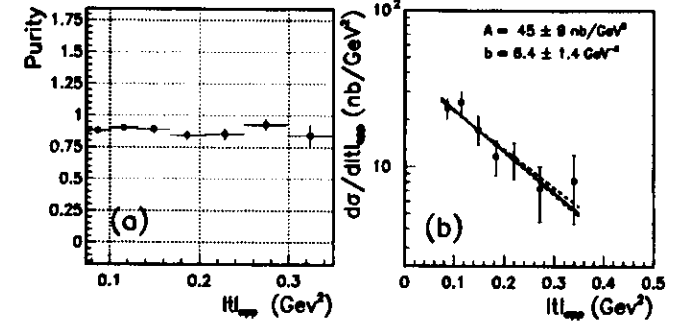
Figure 8.12: The $d\sigma/d|t|_{app}$ distribution. The purity in each bin (a) is high as a result of the good measurement resolution (see chapter 5). The fit obtained is shown in (b) as a continuous line, while the two dashed lines define the fits obtained when the beam emittance is varied by a factor ×2 (×½).

Emittance	A (nb/GeV^2)	b (GeV^{-2})
nominal	45 ± 9	6.4 ± 1.4
×2	47 ± 11	7 ± 1.7
×½	42 ± 9	6.2 ± 1.4

Table 8.3: Results of the fit to the $d\sigma/d|t|_{app}$ distribution using nominal values for the beam emittance and values varied of ±50%.

Chapter 9

Analysis of deep inelastic diffractive events and measurement of the diffractive structure function $F_2^{D(3)}$ from 1993 data

The analysis of the 1993 data is presented, based on the selection which has made the observation of diffraction scattering feasable at HERA. The gross points of the analysis, the method and the achievements are discussed here as a necessary prologue to the measurement performed in 1994 with the proton tagging.

9.1 Observation of diffractive scattering

Without the tagging of an intact proton emerging from the interaction, the measurement of diffraction at HERA has been based [114, 115, 116, 117] on the identification of a particular diffraction topology in the final state (i.e. the presence of a large rapidity gap between the outgoing proton direction and the remaining hadronic final state, Fig. 9.1) which shows to be consistent with the exchange of a colourless object in the $\gamma^* - p$ system.

The presence of a rapidity gap, which on the contrary is suppressed[1] in non diffractive DIS events, where colour is transferred between the scattered quark and the proton remnant, has been used as a selection criterium in the following analysis.

The maximum pseudorapidity, η_{max}, of an event is defined as the pseudorapidity of the object (either a calorimeter cluster or a track, as explained in chapter 7) lying most closely to the outgoing proton direction. Small values of η_{max} correspond to large angles between the produced calorimeter deposit and the outgoing proton. When the distribution of η_{max} for the data selected with a DIS trigger is compared with the prediction of a DIS Monte Carlo (Fig. 9.2), a clear excess of data is observed below $\eta_{max} = 1.5$, corresponding to the large rapidity gap events. As a consequence of this observation, an effort has been made to include such processes in the DIS generators (ARIADNE and LEPTO).

---

[1]The probability of producing an event with a rapidity gap of greater than 2 units by effects in perturbative QCD has been estimated for quark antiquark pair production at LEP energies to be below 10^{-3}, consistent with measurements at lower energies.
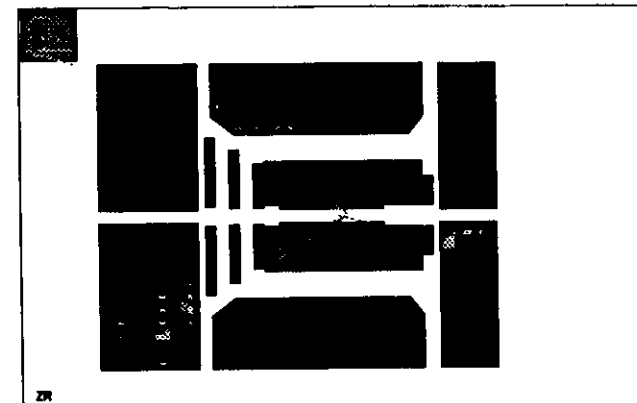
Figure 9.1: Layout of a DIS large rapidity gap event in the ZEUS detector. The scattered electron is detected in the rear direction (RCAL).

The properties of the events selected to have $\eta_{max} < 1.5$ indicate that the underlying mechanism is of leading twist (same dependence on Q^2 of all DIS events) and diffractive nature (the fraction of DIS events with a large rapidity gap does not decrease rapidly with increasing W, as expected for a Regge trajectory with intercept ≥ 1, the so called pomeron). The hypothesis of pomeron exchange can also be inferred from the flatness of the η_{max} distribution below 1.5 if one considers that, according to Regge theory, the behaviour of the total cross section as a function of energy is of the form: $\sigma_{TOT} \propto s^{\alpha(0)-1}$ which leads, since $s \sim e^{2\Delta\eta}$, to a constant cross section as a function of the pseudorapidity η for the case where the exchanged object has an intercept $\alpha(0) \simeq 1$.

An improved criterium (w.r.t. a simple cut on η_{max}) to separate diffractive from non-diffractive events is presented here, which uses the direction of the total hadronic energy flow of the event, determined from all the detected particles in the final state.

The DIS event selection in 1993 was similar to that described in chapter 6, the DA variables were used to reconstruct the kinematics and the following offline cuts were applied:

- $E'_e \geq 5 GeV$, to ensure good electron identification;

- $Q^2_{DA} \geq 8 GeV^2$;

- $y_{JB} \geq 0.04$, to give sufficient accuracy for the DA reconstruction;

- $\delta \geq 35$ GeV (with respect to the measured interaction point), to reduce radiative corrections and photoproduction background;

- $y_e \leq 0.95$, to reduce photoproduction background;

- the impact point of the electron on the face of the RCAL was required to lie outside a square of side 32 cm centred on the beam axis (box cut), to ensure that the

124

125
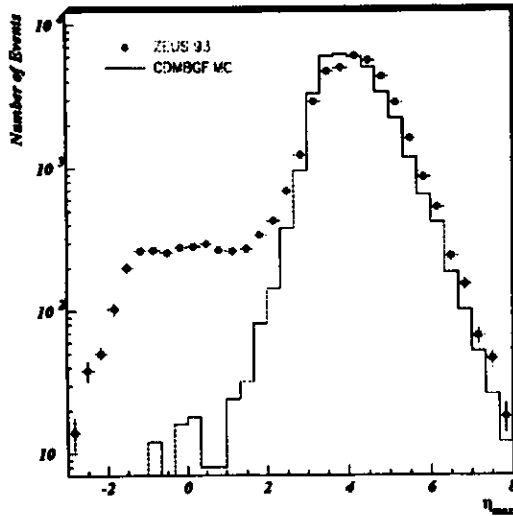
Figure 9.2: The η_{max} distribution for DIS events (dots) compared with the prediction of a DIS Monte Carlo (solid line) which does not contain the simulation of DIS diffractive events.

electron shower was fully contained within the calorimeter and its position could be reconstructed with sufficient accuracy. The SRTD was not implemented during 1993;

- a vertex, as reconstructed from VXD+CTD tracks, was required with $|Z_{vtx}| \leq 40$ cm.

A total of 31,083 events was selected in this way corresponding to an integrated luminosity of $0.54 pb^{-1}$ (with an estimated error of $\pm 3.5\%$). Using the number of events produced by unpaired electron and proton bunches, the contamination from beam gas background and from cosmic-ray muons were estimated to be less than 1% each. The background in the total DIS sample due to photoproduction was estimated to be $(2.5 \pm 1\%)$ from a fit to the shape of the δ distribution before the above cut on δ was applied [118].

9.2 Selection criterium for diffractive events based on a combined $\eta_{max}-\theta_h$ cut.

For values of η_{max} (defined as in chapter 6) up to 1–1.5 (as it can be seen in Fig. 9.2) the non-diffractive DIS background is a negligible background to the diffractive sample, which

increases for values of η_{max} above 1.5–2. In previous analysis of the ZEUS data (published as [113, 114]) diffractive events were selected by cutting on $\eta_{max} < 1.5$. This cut selects a rather pure sample of diffractive events, useful to establish a signal but it limits acceptance for events with large M_X.

The η_{max}-cut is dependent on the most forward condensate but does not use the information from the full energy flow. Larger acceptance can be achieved by including more information from the hadronic energy flow. Since in diffractive scattering the proton remains intact or, in the case of double dissociative events, dissociates independently from the photon, the hadronic activity in the detector in general will not follow the proton direction. The hadronic angle θ_h, defined as:

$$\cos\theta_h = \frac{\sum_i p_{zi}}{|\sum_i \vec{p_i}|},\qquad(9.1)$$

(where $\vec{p_i}$ is the vector constructed from the energy E_i, polar angle θ_i and azimuthal angle ϕ_i of the calorimeter cell i), represents the average direction of the hadronic activity. Non-diffractive DIS events have mostly $\cos\theta_h$ close to 1 because of the colour flow between the struck quark and the outgoing proton system, while a substantial fraction of diffractive events is found at $\cos\theta_h$ less than 1. Fig. 9.3a, b show scatter plots of η_{max} versus θ_h for the diffractive and non-diffractive DIS Monte Carlo samples. A cut $\cos\theta_h < 0.75$ combined with $\eta_{max} < 2.5$ allows a larger acceptance of diffractive events than the $\eta_{max} < 1.5$ cut, at the price of a slightly higher background which has to be subtracted. This combined cut, used to select the diffractive sample, is called in the following the $\eta_{max} - \theta_h$ cut.

In order to estimate the fraction of events where both the photon and the proton dissociate and the proton system is not detected, the ratio of double to single dissociative events in the measured W range is taken, from proton proton measurements, to be approximately 0.76. As shown in Fig. 9.4, it is found that excited proton states with mass $M_N \leq 4GeV$ would pass the diffractive selection cuts. Beyond this range the energy deposition in the forward calorimeter is typically above 400 MeV. The overall acceptance for double dissociative events is 23%. The estimated double dissociative contribution is therefore $\simeq (15 \pm 10)\%$ which is expected to be independent of β and Q^2 and not vary significantly with x_{IP}. This result assumes factorisation in Regge theory, i.e. that the nucleon mass spectrum and the ratio of double to single dissociative events is similar to that measured in proton-proton collisions at similar energies.

9.2.1 Estimation of the diffractive component

In this section, only the shapes of the distributions and not the absolute normalisations of the diffractive models are considered. The η_{max} and θ_h distributions are used to determine the fraction of diffractive events passing the DIS selection criteria. A linear combination of diffractive DIS (either the NZ or the POMPYT[2] Monte Carlo) and non-diffractive DIS Monte Carlo events are fitted to the data.

The η_{max} and θ_h distributions were first fitted separately to check consistency between the results and then together to obtain a global result. Fig. 9.5 shows the fits to these distributions. The part of each distribution that corresponds to the forward region of the detector (high values of η_{max} and low values of θ_h) was put into one single bin to reduce

---

[2] Two samples were generated corresponding to two different pomeron structure functions, a hard quarkonic structure function (HP) and a soft quarkonic structure function (SP), as described in chapter 4.
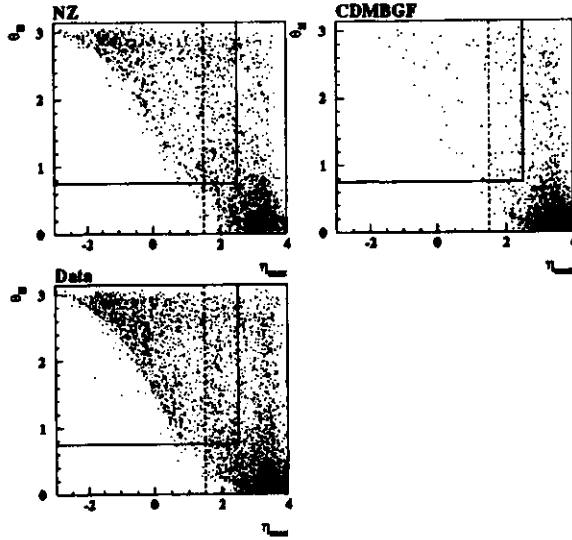
NZ   CDMBGF

Data

Figure 9.3: θ_h versus η_{max} distribution for diffractive (NZ) and non-diffractive (CDMBGF) Monte Carlo events and for the selected DIS data. The full line indicates the η_{max}-θ_h cut used to select diffractive events. The dotted line corresponds to $\eta_{max} = 1.5$.

problems associated with a detailed description of the hadronisation of the proton remnant. For each distribution a variety of different binnings was tried and the results were found to be stable.

The results are summarised in Table 9.1, where the default parameters have been used for the models (without any particular tuning to the data). Since neither NZ nor POMPYT describes diffractive vector meson production a simulation of exclusive ρ^o production (where the DIPSI generator was used) was added in order to incorporate the effect of low-mass (both the resonant and the continuum part of the spectrum) states. This contribution was estimated to be typically $\sim$ 7% of the diffractive sample from a fit to the observed M_X spectrum in different Q^2 intervals. For each model, a reduction of χ^2_{dof} by 1–2 was found when ρ^o production was included, with consistent results obtained for the fraction of diffractive events.

The SP model was also extensively tested. In fits to the η_{max} and θ_h distributions, SP does not reproduce the shapes correctly. Its very soft β distribution tends to populate large η_{max} bins and, consequently, the fits do not describe the data. In order to reproduce the low η_{max} behavior seen in the data, SP would predict $\sim$ 35% of all DIS to be diffractive. The
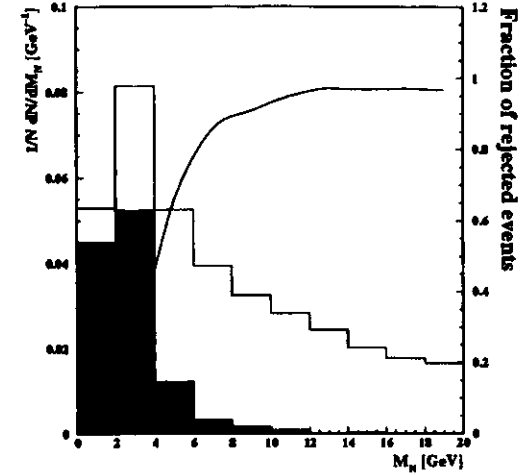
Figure 9.4: Acceptance for double dissociative events. The mass of the nucleon system, M_N, for double dissociative events generated by the PYTHIA Monte Carlo is indicated by the full line histogram. The shaded area indicates those events which are selected by the $\eta_{max} - \theta_h$ cut. The fraction of double dissociative events rejected by this cut, as a function of M_N, is indicated by the line.

inconsistency of the results obtained by the fits to the η_{max} and the θ_h distributions shown in Table 9.1 indicate that a pure soft β distribution cannot describe the data. For these reasons the SP model alone was not considered any further. Results obtained with the combined HP+SP model, discussed in the following section, are also given in Table 9.1. The fractions obtained with the HP+SP model are similar to those determined using the NZ model.

9.2.2 Inclusive distributions

In the following, the shapes of the observed distributions in W, Q^2, x, M_X, x_{IP} and β are considered. The relative normalisation of the models is obtained from the above fits. It should be noted that the normalisation of the non diffractive component, which is relevant for the background subtraction, is independent of the diffractive model used to fit the data to within 5%.

In order to confine the analysis to regions of acceptance above $\simeq$ 80%, the following (M_X, y) intervals were considered:

$$M_X < 10 \text{ GeV} \quad \text{for} \quad 0.08 < y < 0.2,$$
$$M_X < 16 \text{ GeV} \quad \text{for} \quad 0.2 < y < 0.3,$$
$$M_X < 20 \text{ GeV} \quad \text{for} \quad 0.3 < y < 0.8.$$
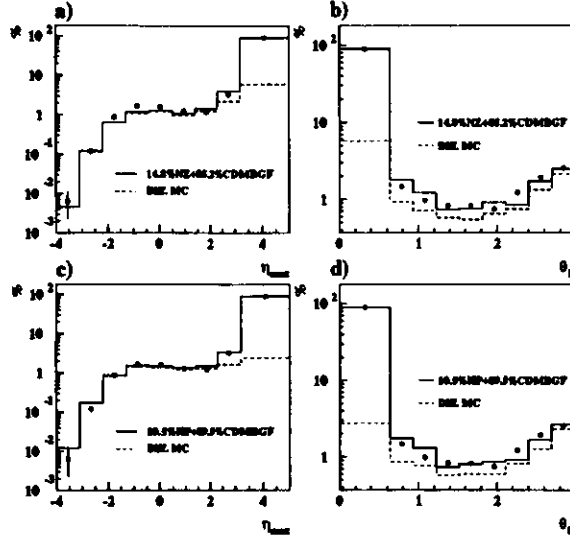
Figure 9.5: Percentage of DIS data as a function of η_{max} and θ_h. The data are described by the sum of the diffractive and non-diffractive contributions obtained from Monte Carlo simulation, with relative fractions determined by a fit to the data. The dashed line corresponds to the diffractive contribution and the sum of the diffractive and non-diffractive Monte Carlo models is indicated by the full line.

According to Monte Carlo studies, the $\eta_{max} - \theta_h$ cut reduces the non diffractive DIS component by $\simeq 60\%$ and the diffractive component by $\simeq 20\%$, giving a contamination from non diffractive DIS of less than 15% in these (M_X, y) intervals. This background is subtracted from the data before comparison with the diffractive Monte Carlo predictions.

Fig. 9.6 shows the x, Q^2, W, $x_{I\!P}$, M_X and β distributions after applying the $\eta_{max} - \theta_h$ cut, requiring the data to be in the accepted ranges of (M_X, y) and subtracting the DIS background indicated in the figure. The errors on the data points are calculated by summing in quadrature the statistical error (which is the dominant error) and 50% of the total subtracted DIS background (which is taken as an upper limit estimate of the uncertainty due to the DIS background). In addition, the predictions from the two diffractive models (NZ and HP) are shown.

In general, both models describe the data. Differences are observed in the M_X and β distributions, where the HP model underestimates the observed number of events at low β values and does not reproduce the observed M_X distribution at large M_X. The NZ model, incorporating a soft component, describes the observed β and M_X distributions.

A pure "hard" β distribution cannot account for the data, therefore, the observed β spectrum was fitted as a sum of a "hard + soft" contribution from the POMPYT Monte

Model	η_{max}		θ_h		$\eta_{max} + \theta_h$	
	% of diffr.	χ^2_{dof}	% of diffr.	χ^2_{dof}	% of diffr.	χ^2_{dof}
NZ	14.2 ± 2.5	4.7	15.3 ± 2.5	4.0	14.8 ± 3.0	4.3
SP	35.9 ± 7.0	10.5	15.4 ± 2.6	5.0	33.0 ± 6.0	24
HP	10.3 ± 2.0	2.2	10.8 ± 2.0	4.1	10.5 ± 2.7	3.0
HP+SP	15.6 ± 1.3	3.7	13.4 ± 1.3	5.4	14.6 ± 1.4	4.6

Table 9.1: Fraction of diffractive events and χ^2 per degree of freedom (χ^2_{dof}) values obtained from fits using NZ, SP, HP or HP+SP.

Carlo. This resulted in a contribution of $\simeq 60\%$ and $\simeq 40\%$ from HP and SP, respectively. This HP+SP model is also shown in Fig. 9.6. Comparison with the data indicates that such a model also describes the observed β behaviour.

To investigate the β distribution in more detail, each (M_X, y) interval was divided into two Q^2 bins:

$$Q^2 = 8 - 20, \ 20 - 160 \ GeV^2.$$

The results, together with the predictions from the diffractive models are shown in Fig. 9.7. In the low y intervals (Fig. 9.7e and f) the Monte Carlo models reproduce the shape of the data reasonably well. In the high-y and low-Q^2 intervals where the mass extends to larger values (Fig. 9.7a and c) and the soft contribution is important, the NZ model best describes the data. The HP+SP model reasonably describes the data and gives an improved description compared to the HP model in each (M_X, y) interval.

Using the NZ model, the combined fit to the η_{max} and θ_h distributions was performed in bins of W and x respectively, separately for the two Q^2 intervals indicated above, to extract the fraction of diffractive events as a function of these variables. Fig. 9.8 shows the diffractive fraction as a function of the observed W and x for different values of Q^2, corrected for the acceptance of the cuts to select diffractive events, which is however model dependent. The results obtained using the HP+SP model agree within statistical errors. The results extracted using the HP model give a normalisation which is $\simeq 30\%$ lower, but with the same dependence on x, W and Q^2. The fits are mainly sensitive to the hard component: a large uncertainty on the diffractive contribution to the DIS sample comes from the soft part in the pomeron structure function, which is suppressed by the applied cuts, especially at small values of W. In all cases, no strong dependence of this ratio is observed as a function of x, W or Q^2.

9.3   Measurement of the diffractive structure function

As described in chapter 1, the differential cross section can be expressed in terms of the diffractive structure function $F_2^{D(3)}$ as a function of β, $x_{I\!P}$ and Q^2 in the following way:

$$\frac{d^3\sigma_{diff}}{d\beta dQ^2 dx_{I\!P}} = \frac{2\pi\alpha^2}{\beta Q^4}\left(1 + (1-y)^2\right) F_2^{D(3)}(\beta, Q^2, x_{I\!P}). \tag{9.2}$$

Details on the extraction procedure of the cross section and the structure function from the observed number of data events can be found in chapter 10. According to Monte Carlo studies,

the resolution of M_X, reconstructed with the triple angle method described in chapter 6, is approximately 27%, independent of M_X. The M_X reconstruction is affected by energy loss in inactive material in front of the calorimeter and the position determination of hadrons. In order to reduce migrations at small masses, the cell energy thresholds for isolated cells were increased. Monte Carlo studies show that, except for very small masses ($< 3GeV$) where calorimeter noise becomes important, M_X is systematically shifted by 10% to smaller values, independent of y and Q^2. In order to compensate for this shift, a correction factor of 1.10 was applied to the measured M_X values for the determination of the diffractive structure function. The resolution of $x_{I\!P}$ is approximately 25%. The resolution of β varies smoothly with β from 40% at $\beta = 0.1$ to 20% at $\beta = 0.8$.

The statistics of the 1993 data allows four ranges in Q^2 to be selected above a lower limit of $8GeV^2$. The overall acceptance due to the DIS and diffractive cuts in the selected bins given in Table 9.2 is always greater than 50% and typically $\simeq$ 80%.

In order to control the influence of photoproduction background, radiative corrections (which were not implemented in the MCs used for the 1993 data analysis) and F_L contributions, the analysis is restricted to $y < 0.5$. As a consequence the minimum scattered electron energy requirement is raised to $10GeV$. It was checked that the sensitivity to F_L is smaller than the quoted errors in all bins. Furthermore, the region $\beta < 0.8$ is selected to exclude the region of low masses where vector meson production is dominant.

The level of photoproduction background is estimated in bins of $x_{I\!P}$ and Q^2 by fits to the δ distributions (see [118] for details).

The bins are selected to have $x_{I\!P} < 0.01$ and $\beta > 0.1$ where the non-diffractive component can be safely estimated. In each of the bins the number of events is then evaluated by subtraction of the estimated number of DIS background events, based on the ARIADNE Monte Carlo program with the normalisation described in the previous sections. The contribution of the DIS background is given in Table 9.2. To unfold the effects of acceptance and event migration the NZ Monte Carlo has been used.

9.3.1 Systematic errors

Several systematic checks were performed to estimate the uncertainties due to the selection cuts, background estimate and the unfolding. Systematic errors due to the DIS event selection were evaluated in the following way (see chapter 10 for a detailed discussion):

- different algorithms were used to identify the scattered electron which differ in purity and efficiency. The changes to $F_2^{D(3)}$ were below 10%;

- the cut on E'_e was decreased from 10 to $5GeV$. The change of $F_2^{D(3)}$ was less than 5% in each bin;

- the box-cut was changed by $2cm$ from the nominal values. This resulted in changes which were always less than 15%;

- the δ-cut was raised from $35GeV$ to $40GeV$, to study the effect of radiative corrections, which were not included in the simulations. This resulted in a general shift of $\simeq$ 10% towards smaller $F_2^{D(3)}$ values;

- the $y_{J\!B}$-cut was changed from 0.04 to 0.02 and to 0.06. This affected the region of large $x_{I\!P}$ where $F_2^{D(3)}$ changes by about 10%.

Systematic errors due to the diffractive event selection were evaluated in the following way:

- the effect of a possible mismatch between the hadronic energy scale in the Monte Carlo and the data was investigated by shifting the hadron energy scale by 7% in the Monte Carlo simulation. The use of the DA variables resulted in changes on $F_2^{D(3)}$ which were always smaller than 2%;

- the fraction of low mass events was reduced by 50%. Due to migrations from $\beta > 0.8$, this change influences the small Q^2, high β bin, where the values were shifted upwards by $\simeq$ 10%;

- the HP model was used instead of the NZ simulation for unfolding the data. Some effect was seen in the small β region, where the pomeron structure functions differ. The changes to $F_2^{D(3)}$ were typically $\simeq$ 10%;

- as a systematic check for the estimate of the DIS background the η_{max} cut was reduced from 2.5 to 2.0 resulting in changes of up to 20% in the highest $x_{I\!P}$ bins. The η_{max} cut was also increased from 2.5 to 3.0 resulting in changes of up to 10%;

- the cells with $\eta > 2.5$ were removed to check the dependence on the double-dissociative contribution, resulting in changes which were up to 5%.

Overall most of these checks yielded results which agree with the standard method within statistical errors. The differences of the DIS and diffractive systematic checks compared to the standard method were combined in quadrature to yield the quoted systematic errors.

9.3.2 Results and discussion

Table 9.2 summarises the results for $F_2^{D(3)}$. The corresponding diffractive cross section, σ_{diff}, is also given. The statistical errors include statistical uncertainties from the Monte Carlo models used for the unfolding. The $F_2^{D(3)}$ results are displayed in Fig. 9.9. The data are observed to fall rapidly with $x_{I\!P}$, while the dependence on β and Q^2 appears to be weak.

Dependence on $x_{I\!P}$

It has been investigated whether the $x_{I\!P}$ dependence of $F_2^{D(3)}$ is the same in each β, Q^2 interval, as expected if factorisation holds (see chapter 2). For this purpose a fit of the form:

$$b_i \cdot (1/x_{I\!P})^a$$

has been performed, where the normalisation constants b_i are allowed to vary while the exponent a is the same in each β, Q^2 interval. The result of the fit is:

$$a = 1.30 \pm 0.08 \ (stat) \ ^{+\ 0.08}_{-\ 0.14} \ (sys).$$

The systematic errors are calculated by refitting the $F_2^{D(3)}$ values according to the variations listed in the section above and combining the positive or negative deviations from the central value of a in quadrature. The overall χ^2 values of these fits are in the range 8.2–14.0 for 23 degrees of freedom depending on the systematic check. The χ^2 values for each of the β,Q^2 intervals are in the range 0.1–1.1 per degree of freedom. Within the accuracy, these data are therefore consistent with the assumption of factorisation in the measured kinematic range.

The observed dependence on $x_{I\!P}$ is compatible with a Donnachie-Landshoff type of flux factor which yields $a \simeq 1.09$ and which is based on a phenomenological description of "soft hadronic" diffractive interactions.

In the model of Buchmüller discussed in chapter 1, the value of a is related to the dependence of the total structure function with respect to x. In [118], a parametrisation of the measurement of F_2 yielded an x-dependence at small-x of $F_2 \propto (1/x)^{0.35+0.16 \log_{10} Q^2}$. The observed dependence of the diffractive contribution of the proton structure function on $x_{I\!P}$ is compatible with such a dependence, as it can be seen in Fig 9.10, where the measurements of $F_2^{D(3)}$ for different β are included toghether with the measurements of F_2/x scaled by a relative normalisation factor.

Dependence on β and Q^2

In order to illustrate the β and Q^2 dependence of $F_2^{D(3)}(\beta, Q^2, x_{I\!P})$, $F_2^{D(3)}$ was integrated over the measured range of $x_{I\!P}$, $6.3 \cdot 10^{-4} < x_{I\!P} < 10^{-2}$, using the fitted $x_{I\!P}$ dependence. The resulting values of $\tilde{F}_2^D(\beta, Q^2)$ are shown in Fig. 9.11 as a function of β and Q^2. It should be noted that these results assume that a universal $x_{I\!P}$ dependence holds in *all* regions of β and Q^2. In particular, there is a contribution due to regions of $x_{I\!P}$ which are not measured and where the hypothesis of a universal $x_{I\!P}$ dependence has not been tested experimentally.

Assuming factorisation and no Q^2 dependence, the β dependence of $F_2^{D(3)}$ is fitted to a form:

$$F_2^{D(3)} = (1/x_{I\!P})^a \cdot b \cdot (\beta(1-\beta) + \frac{c}{2} \cdot (1-\beta)^2), \qquad (9.3)$$

with $a = 1.30$. The soft contribution to the structure function is given by the $(1-\beta)^2$ term. The multiplicative factor of $\frac{c}{2}$ is chosen such that the integral over β of the soft contribution is equal to that of the hard contribution when $c = 1$, while the power of 2 is adopted from the NZ model. The results of the fit are:

$$b = 0.018 \pm 0.001 \ (stat.) \pm 0.005 \ (sys.),$$

$$c = 0.57 \pm 0.12 \ (stat.) \pm 0.22 \ (sys.),$$

with a χ^2 in the range 15–23 for 33 degrees of freedom depending on the systematic check. A fit without the $(1-\beta)^2$ soft contribution resulted in χ^2 values in the range 56–81 for 34 degrees of freedom. This increased χ^2 value indicates that a soft component is required in the pomeron structure function. The $F_2^{D(3)}$ results are compared with the obtained parametrisation, indicated by the solid line, and the $\beta(1-\beta)$ hard contribution, indicated by the dashed line, in Fig. 9.11.

As a function of Q^2 for fixed β, the $\tilde{F}_2^D(\beta, Q^2)$ values are approximately independent of Q^2 for all β values, which is consistent with a picture where the underlying interaction is the scattering of a virtual photon with point-like quarks within the pomeron. Further investigation on the presence of scaling violations which could disentangle a predominant gluonic or quarkonic nature of the pomeron will necessitate an improved statistics.

Models comparison

Finally the absolute predictions of the models for the cross section are compared with the $F_2^{D(3)}$ values. Fig. 9.12 shows the comparison between data and the predictions of several models of single diffractive dissociation for which the momentum sum rule for quarks is not satisfied (refer to chapter 2). The estimated 15% fraction of double dissociative events has been subtracted in order to compare with these models.

At high β values the predictions of Nikolaev-Zakharov, Donnachie-Landshoff and Capella et al. underestimate the observed values slightly, but are generally in reasonable agreement. At smaller β values, the Donnachie-Landshoff parametrisation, which includes only a hard component of the pomeron structure function, underestimates the observed $F_2^{D(3)}$. The Capella et al. and Nikolaev-Zakharov predictions, which also include a soft component, are able to give a fair description at smaller β values. The factorisation-breaking effects in the model of Nikolaev-Zakharov, which occur at small β values, are too small to be observable in this analysis.

In Fig. 10.11 the data are compared with a model for which the momentum sum rule for the pomeron structure function is assumed for the light quark flavours (u,d) and the β dependence is taken from the parametrisation, discussed above. Adopting the Donnachie-Landshoff flux factor, the observed $F_2^{D(3)}$ is about a factor three to four below the expectation if the momentum sum rule is assumed to be fulfilled only by quarks. An uncertainty arises from the choice of the pomeron flux factor: if the Ingelman-Schlein form for the flux factor is adopted then the prediction is reduced by approximately 30%. These comparisons indicate that in an Ingelman-Schlein type model the quarks alone inside the pomeron do not satisfy the momentum sum rule.

9.3.3 Summary

The analysis of the 1993 diffractive events selected by a large rapidity gap events has started the investigation of the properties of diffraction in deep inelastic scattering.

The relative contribution of diffractive events to the total deep inelastic cross section is found to have no strong dependence on W or Q^2, being compatible with the predictions of Regge theory (developed in the framework of hadron hadron scattering) and not ascribable to higher twist corrections.

A diffractive cross section has been determined, allowing a direct comparison with the hadron hadron data and the existing models for picturing diffraction in deep inelastic scattering.

Within the experimental errors, the measurement is consistent with models where diffraction is described by the exchange of a particle-like pomeron where the structure function factorises into a pomeron flux factor, which depends on $x_{I\!P}$ and a pomeron structure function, which is independent of $x_{I\!P}$.

The diffractive structure function is also well described by the Nikolaev-Zakharov model, which does not require the concept of a particle-like pomeron, in terms of overall normalisation and dependence on the kinematic variables, $x_{I\!P}$, β and Q^2.

The obtained parametrisation for the $x_{I\!P}$ dependence in this particular kinematical range $(M_X \geq 3 GeV)$ is still compatible with that obtained from hadron hadron interactions.

In the measured Q^2 range, the pomeron structure function is approximately independent of Q^2 at fixed β consistent with an underlying interaction where the virtual photon scatters

off point-like quarks within the pomeron.

The β-dependence of the pomeron structure function requires a soft component in addition to the hard one found by the UA4 experiment.

Finally, in an Ingelman-Schlein type model, where commonly used pomeron flux factor normalisations are assumed, it is found that the quarks within the pomeron do not saturate the momentum sum rule.
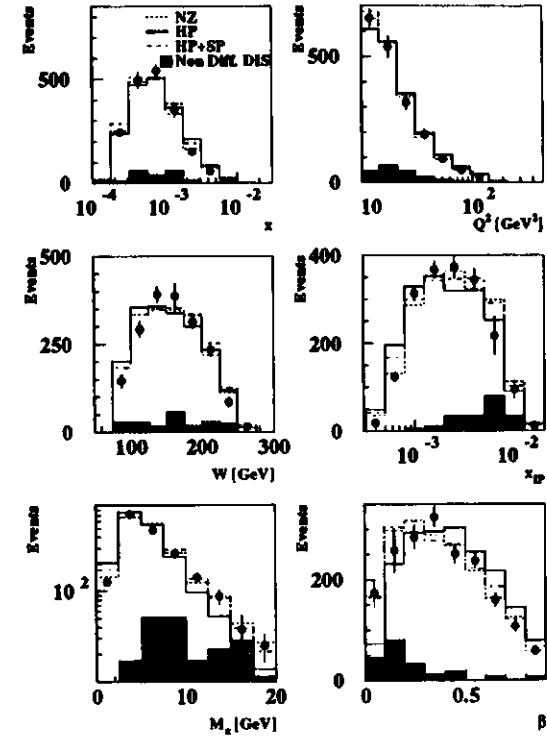
Figure 9.6: Observed distributions of x, Q^2, W, x_{IP}, M_X and β for the selected (M_X, y) intervals. Uncorrected data are indicated by the dots. The errors are the statistical errors combined in quadrature with 50% of the non-diffractive DIS background. The predictions from HP (full line), HP+SP (dashed line) and NZ (dotted line) models are shown. The non-diffractive DIS background which has been subtracted from the data is indicated by the shaded area.
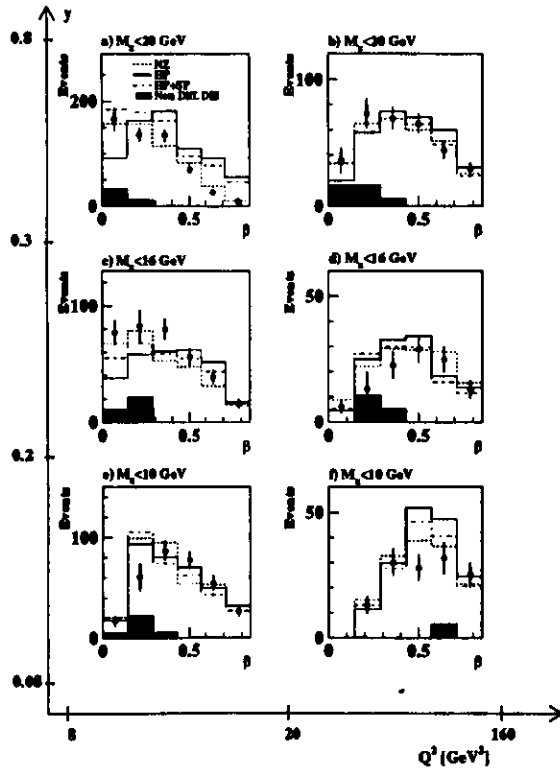
Figure 9.7: Observed β distribution as a function of (y, Q^2, M_X). The Q^2 intervals are 8-20 and 20-160 GeV^2, the y intervals are 0.08-0.2, 0.2-0.3 and 0.3-0.8, and the M_X intervals are (a,b) 0-20, (c,d) 0-16 and (e,f) 0-10 GeV. Uncorrected data are indicated by the dots. The errors are the statistical errors combined in quadrature with 50% of the non-diffractive DIS background. The predictions from HP (full line), HP+SP (dashed line) and NZ (dotted line) models are shown. The non-diffractive DIS background which has been subtracted from the data is indicated by the shaded area.
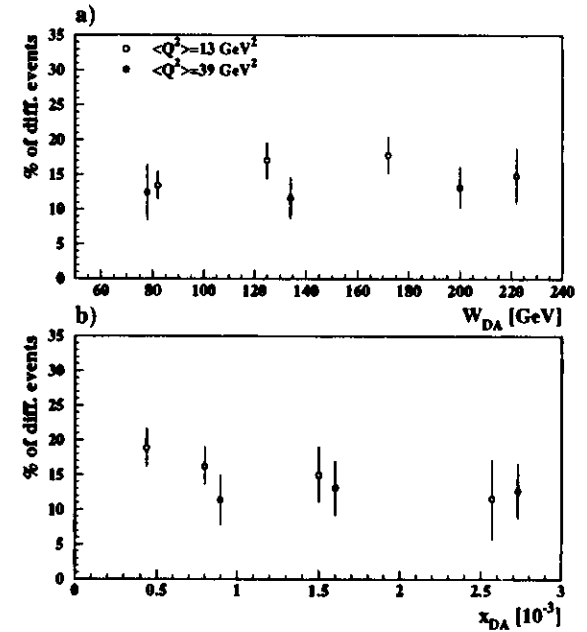
Figure 9.8: Observed fraction of diffractive events as a function of W_{DA} and x_{DA} in two Q^2 intervals. The data are fitted to the NZ model for diffractive processes and the CDMBGF model for the non-diffractive contribution. The errors are the statistical errors combined in quadrature with 50% of the non-diffractive DIS background.

Q^2 (GeV²)	β	x_{IP}	#events	#non-diff. background	σ_{diff} (nb)	$F_2^{D(3)} \pm$stat. $\pm$sys.
10	0.175	0.0032	54	7.1	0.128	9.7 ± 1.6 ± 2.8
10	0.175	0.0050	32	5.2	0.116	5.0 ± 1.1 ± 2.3
10	0.375	0.0013	62	0.9	0.144	37.7 ± 5.2 ± 6.5
10	0.375	0.0020	43	2.8	0.152	22.0 ± 3.7 ± 3.7
10	0.375	0.0032	15	2.8	0.097	9.2 ± 3.0 ± 4.5
10	0.65	0.00079	56	0.9	0.077	47.7 ± 8.7 ±29.9
10	0.65	0.0013	20	0.9	0.074	29.1 ± 7.0 ± 8.5
10	0.65	0.0020	23	0	0.055	10.9 ± 2.3 ± 6.9
16	0.175	0.0032	48	5.2	0.105	9.5 ± 1.6 ± 2.1
16	0.175	0.0050	50	4.7	0.117	6.5 ± 1.1 ± 1.8
16	0.175	0.0079	33	7.5	0.111	3.8 ± 0.9 ± 2.0
16	0.375	0.0013	54	2.8	0.106	38.2 ± 5.9 ± 5.3
16	0.375	0.0020	54	3.3	0.114	20.1 ± 3.1 ± 3.6
16	0.375	0.0032	52	3.3	0.122	13.3 ± 2.0 ± 3.6
16	0.375	0.0050	44	3.8	0.104	6.2 ± 1.0 ± 1.8
16	0.65	0.00079	49	0	0.054	39.8 ± 11.6 ±13.8
16	0.65	0.0013	38	2.8	0.070	32.5 ± 6.3 ± 6.5
16	0.65	0.0020	43	1.4	0.060	13.3 ± 2.5 ± 3.7
16	0.65	0.0032	29	0	0.066	8.5 ± 1.6 ± 2.3
28	0.175	0.0050	35	3.3	0.081	6.4 ± 1.3 ± 1.4
28	0.175	0.0079	32	8.0	0.085	3.8 ± 0.9 ± 1.7
28	0.375	0.0020	26	1.4	0.080	23.4 ± 5.0 ± 3.3
28	0.375	0.0032	35	1.9	0.087	15.7 ± 2.9 ± 2.0
28	0.375	0.0050	41	3.3	0.087	7.5 ± 1.3 ± 1.5
28	0.375	0.0079	19	3.3	0.071	3.1 ± 0.9 ± 1.1
28	0.65	0.0013	30	0.5	0.043	26.5 ± 6.4 ± 9.4
28	0.65	0.0020	35	1.9	0.045	15.7 ± 3.4 ± 2.5
28	0.65	0.0032	25	1.4	0.046	9.2 ± 2.1 ± 2.5
28	0.65	0.0050	23	1.4	0.036	5.4 ± 1.3 ± 2.9
63	0.375	0.0050	17	2.4	0.043	6.8 ± 2.0 ± 1.7
63	0.375	0.0079	16	3.8	0.036	2.6 ± 0.9 ± 1.5
63	0.65	0.0032	22	0.5	0.030	10.8 ± 2.9 ± 0.8
63	0.65	0.0050	17	0.5	0.031	6.2 ± 1.7 ± 0.9
63	0.65	0.0079	11	2.4	0.022	3.0 ± 1.2 ± 0.7

Table 9.2: ZEUS 1993 $F_2^{D(3)}$ results. The overall normalisation uncertainty of 3.5% is not included. The data contain an estimated 15 ± 10% fraction of double-dissociative events.
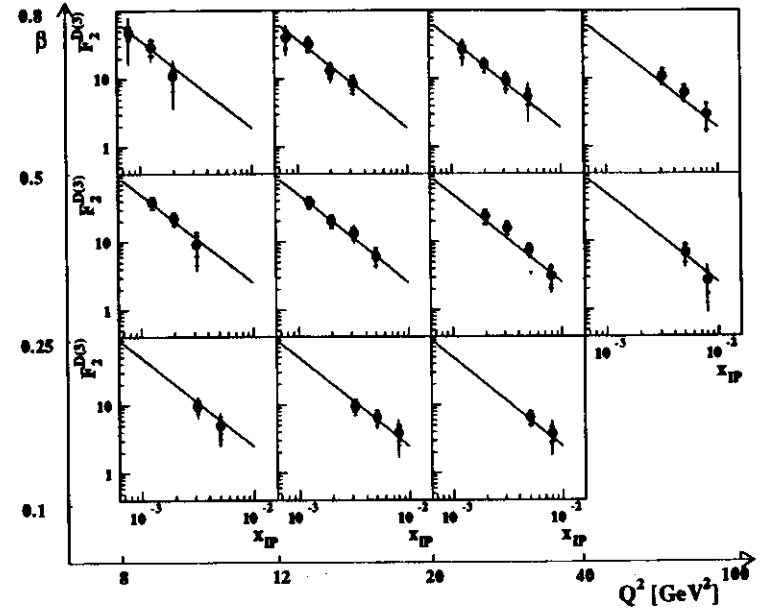
Figure 9.9: The results of $F_2^{D(3)}(\beta, Q^2, x_{IP})$ compared to the parametrisation discussed in the text. The inner error bars show the statistical errors, the outer bars correspond to the statistical and DIS event selection systematic errors added in quadrature, and the full line corresponds to the statistical and total systematic errors added in quadrature. Note that the data include an estimated 15% contribution due to double dissociation. The overall normalisation uncertainty of 3.5% due to the luminosity uncertainty is not included.
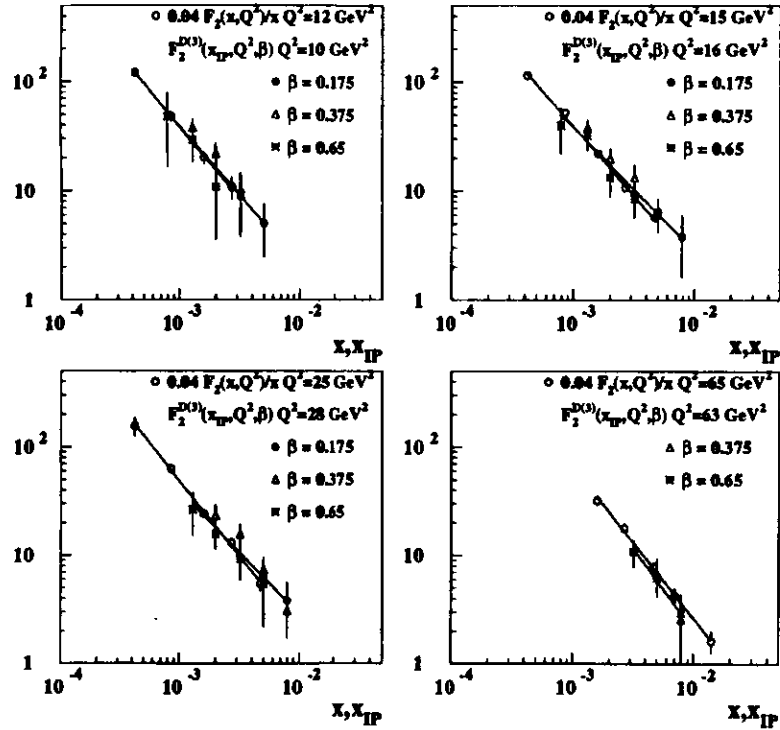
Figure 9.10: A comparison of $F_2^{D(3)}$ and F_2 to test directly the scaling law prediction of Buchmüller et al.
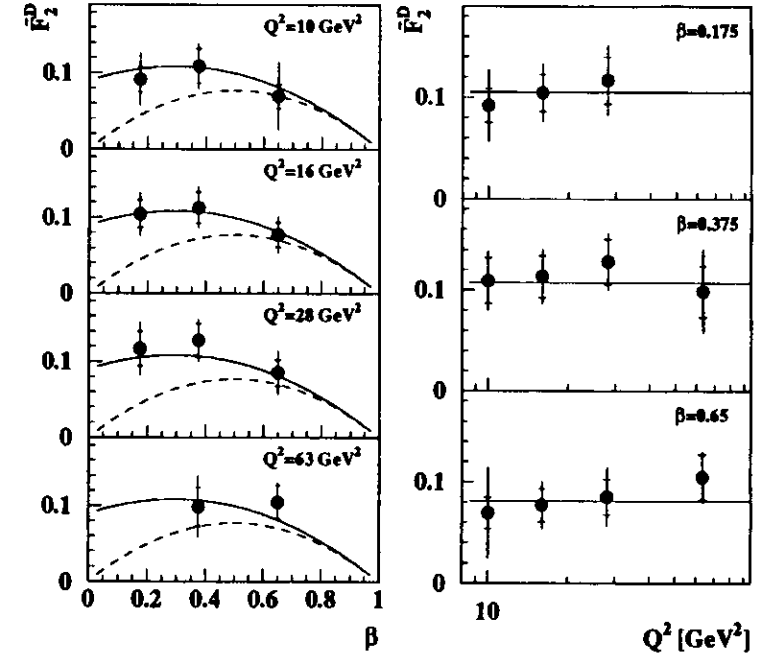
Figure 9.11: The results of $\tilde{F}_2^D(\beta, Q^2)$ compared to the parametrisation discussed in the text, indicated by the full line, and the $\beta(1-\beta)$ hard contribution, indicated by the dashed line. The inner error bars show the statistical errors, the outer bars correspond to the statistical and systematic errors added in quadrature. The systematic errors combine in quadrature the fits of the x_{IP} dependence due to each of the systematic checks discussed in the text. Note that the overall normalisation is arbitrary and is determined by the experimental integration limits over x_{IP} ($6.3 \cdot 10^{-4} < x_{IP} < 10^{-2}$). The data include an estimated 15% contribution due to double dissociation.
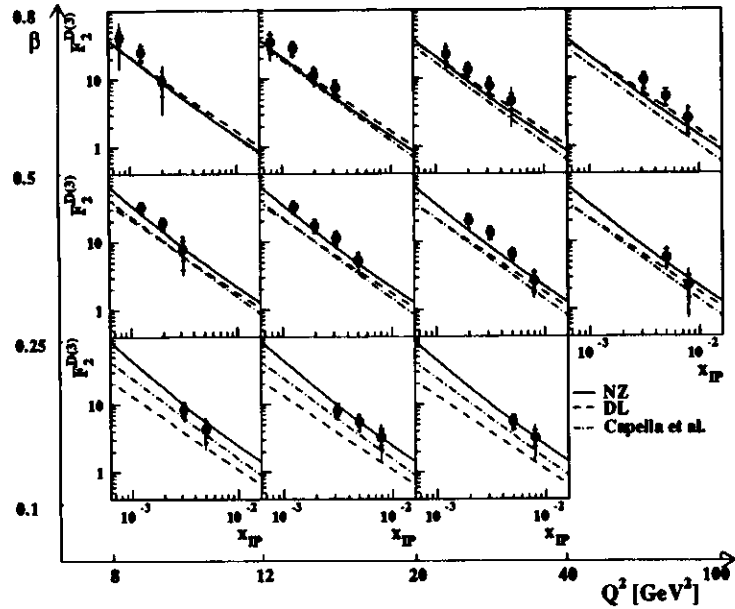
Figure 9.12: The results of $F_2^{D(3)}$ compared to various models for which the momentum sum rule for quarks within the pomeron is not assumed. Note that the estimated 15% contribution due to double dissociation has been subtracted in order to compare with models for the single dissociation cross section. The inner error bars show the statistical errors, the outer bars correspond to the statistical and DIS event selection systematic errors added in quadrature, and the full line corresponds to the statistical and total systematic errors added in quadrature. The overall normalisation uncertainty of 3.5% due to the luminosity and 10% due to the subtraction of the double dissociation background is not included.
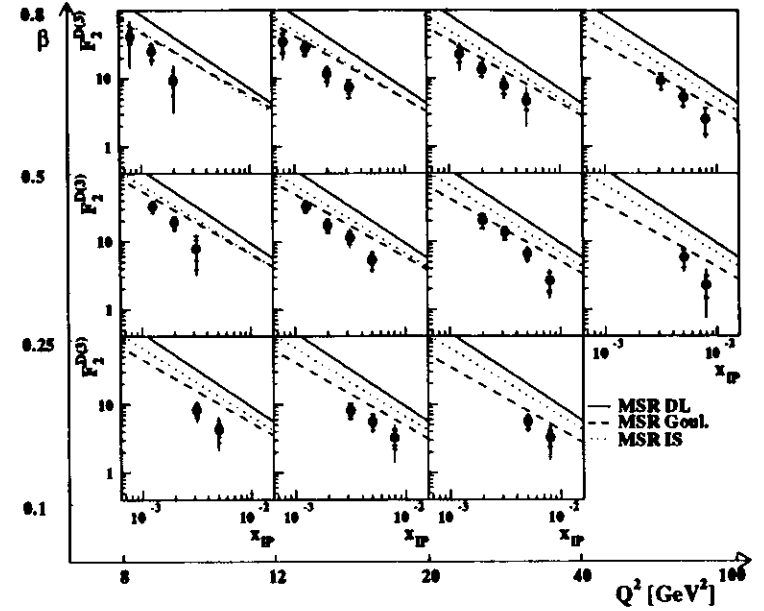
Figure 9.13: The results of $F_2^{D(3)}$ compared to an Ingelman-Schlein type model for which the momentum sum rule (MSR) for quarks within the pomeron is assumed. The β dependence is taken from the parametrisation discussed in the text. Note that the estimated 15% contribution due to double dissociation has been subtracted in order to compare with models for the single dissociation cross section. The inner error bars show the statistical errors, the outer bars correspond to the statistical and DIS event selection systematic errors added in quadrature, and the full line corresponds to the statistical and total systematic errors added in quadrature. The overall normalisation uncertainty of 3.5% due to the luminosity and 10% due to the subtraction of the double dissociation background is not included.

Chapter 10

$F_2^{D(3)}$ from 1994 LPS data

Since the pseudorapidity of a system of mass M_X produced at a center of mass energy W is proportional to $ln(M_X^2/W^2)$, the analysis of diffractive events based on a large rapidity gap requirement (i.e. low values of pseudorapidity) will immediately translate into the selection of low M_X states (the upper limit depending on the W range, but tipically never exceeding a value of $20GeV$). One of the advantages of the analysis based on the tagging of the forthgoing proton with the Leading Proton Spectrometer consists in the abolition of the upper M_X boundary (the presence of a rapiditiy gap is not any longer synonim of diffraction), leading to an extension of the measured range to lower β and higher x_{IP} states. This can be seen in Fig. 10.1 where the distribution of the events selected with the use of the LPS in the (x_{IP}, β) plane is compared with the bins (for one Q^2 range) used by the 1993 $F_2^{D(3)}$ analysis (indicated by the dashed lines) and the extension enabled by the present data (solid lines).

The second advantage of the LPS analysis for the determination of diffractive cross sections is the isolation of a process purely mediated by pomeron exchange. As it has been pointed out in chapter 6, the selection based on a pseudorapidity gap requirement does not reject events where the diffraction happens on pions or secondary reggeons rather than on the proton and where the outgoing proton carries only a small fraction ($< 80\%$) of the incoming momentum. This contribution can be as big as 30% of the observed cross section. The request of having in the final state a fast positive particle with $> 97\%$ of the incoming proton momentum excludes contributions from charge exchange and strongly limits the contamination from neutral reggeon exchange (mainly π, ρ and f). With this constraint the purest sample of pomeron diffraction on protons can be achieved, allowing a precision study of its characteristics such as factorisation, Q^2 evolution and behaviour as a function of the centre of mass energy.

10.1 Binning, resolution and purity

Although the measurement of the proton transverse momentum (and therefore of t) with the LPS gives the possibility of determining the diffractive differential cross section in all the variables of the phase space (β, x_{IP}, Q^2 and t or, alternatively M_X, W, Q^2 and t) the limited 1994 statistics restricts the analysis to a three dimensional space and the integration over t, which was mandatory in the 1993 analysis, has been mantained. The improvement in terms of luminosity and LPS instrumentation (i.e. the addition of the two stations $S1$
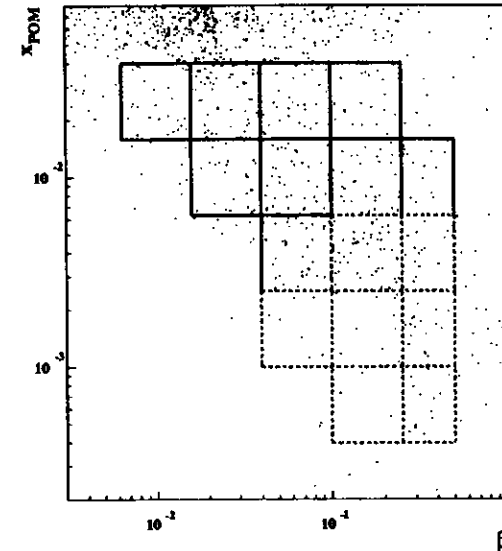
Figure 10.1: 1994 LPS data (dots) with the contour of the bins used in the 1993 $F_2^{D(3)}$ analysis (dashed lines). The extension towards lower β and higher x_{IP} values made possible by the 1994 analysis is indicated by the additional bins drawn as solid lines.

and $S2$) during 1995 data taking will most likely allow the determination of a four-fold cross section and give an even deeper insight into the mechanism of diffraction than what it has been obtained so far.

The binning in (β, x_{IP} and Q^2) for the extraction of the diffractive structure function has been determined by Monte Carlo studies (the resolution is required not to exceed the width of the bin) and by data statistics. The resolution in β and x_{IP} is shown in Fig. 10.2 and Fig. 10.3 for $5 < Q^2 < 20GeV^2$ in the bins selected for the analysis. Bins in β (x_{IP}) are selected to have a width of less than 60% and be equidistant in $log_{10}\beta$ ($log_{10}x_{IP}$) in the region of no overlap with the 1993 analysis (in the region of overlap they have been chosen to be twice the size of the 1993 bins), while a unique bin in Q^2 ($5 < Q^2 < 20GeV^2$) has been chosen according to the statistics limitations of the data sample. The bin edges in β are defined to be at $6 \cdot 10^{-3}, 1.5 \cdot 10^{-2}, 4 \cdot 10^{-2}, 1 \cdot 10^{-1}, 2.5 \cdot 10^{-1}$ and $5 \cdot 10^{-1}$, the bin edges in x_{IP} are defined to be at $4 \cdot 10^{-4}, 1 \cdot 10^{-3}, 2.5 \cdot 10^{-3}, 6.3 \cdot 10^{-3}, 1.6 \cdot 10^{-2}$, and $4 \cdot 10^{-2}$. The final number of bins used, after the requirement of having at least 7 data events in each bin, is 16.
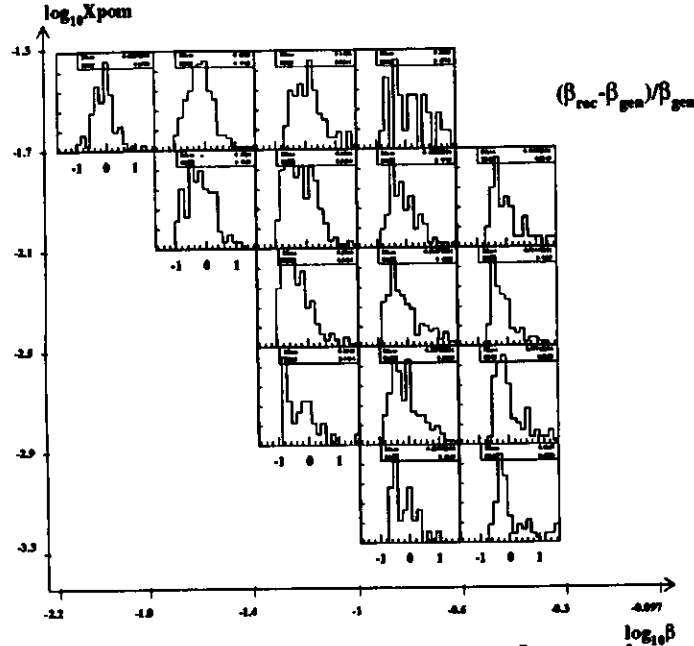
Figure 10.2: The β resolution in the bins chosen for the extraction of $F^D(3)$, in the Q^2 range $4 < Q^2 < 150 GeV^2$. The resolution improves towards lower values of β and higher values of x_{IP}, where the kinematics is mainly reconstructed starting with the scattered proton and electron (without a direct measurement of the hadronic mass M_X in the calorimeter). As described in chapter 7 the determination of M_X (and therefore β) from the proton and electron kinematics leads to a better resolution (a factor of three) with respect to the direct method.

For each bin a correction and purity factor are defined as:

$$Correction(i) = \frac{Events\ generated\ in\ bin\ i}{Events\ reconstructed\ in\ bin\ i} \qquad (10.1)$$

$$Purity(i) = \frac{Events\ reconstructed\ and\ generated\ in\ bin\ i}{Events\ generated\ in\ bin\ i} \qquad (10.2)$$

and estimated through MC simulation. The results are shown in Fig. 10.4 for the selected $F_2^{D(3)}$ bins. The values for the correction exceed largely unity since they take into account the geometrical acceptance of the LPS (typically < 10%). The purity is above 10% for all of the bins.

Good agreement between data and MC is obtained for any of the selected (β, x_{IP}) bins. Fig.10.5 and Fig.10.6 show the β and M_X distributions for data and MC in each of the bins.
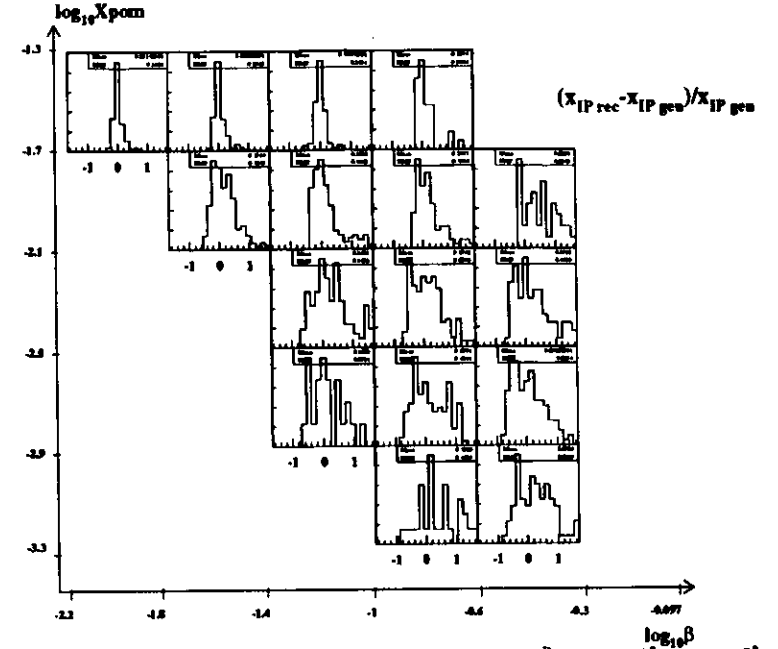
Figure 10.3: The x_{IP} resolution in the bins chosen for the extraction of $F^D(3)_2$ in the Q^2 range $4 < Q^2 < 150 GeV^2$. The resolution improves towards lower values of β and higher values of x_{IP}, where the kinematics is mainly reconstructed starting with the scattered proton and electron (without a direct measurement of the hadronic mass M_X in the calorimeter). As described in chapter 7 the determination of M_X (and therefore x_{IP}) from the proton and electron kinematics leads to a better resolution (a factor of three) with respect to the direct method.

In each β, x_{IP}, Q^2 bin the diffractive structure function $F_2^{D(3)}$ was calculated as:

$$F_2^{D(3)} = \frac{N_{data}}{\epsilon L} \cdot K_c \cdot \frac{1}{\Delta\beta\Delta Q^4 \Delta x_{IP}} \cdot C_c \qquad (10.3)$$

where $\epsilon = \frac{N^{MC}}{N_{gen}^{MC}}$ is the MC estimated acceptance (bin by bin correction), L is the luminosity of the data sample, K_c is the kinematical factor estimated at the center of the bin:

$$K = const \cdot \frac{\beta x_{IP}^a Q^4}{4\pi\alpha^2 \cdot (1 - y - y^2/2)} \qquad (10.4)$$

(the x_{IP} dependence has been varied from the value of $1/x_{IP}^3$ obtained by the analysis of the 1993 diffractive structure function to the soft phenomenological Donnachie Landshoff value of $1/x_{IP}^{1.0}$), C_c is the bin centering correction applied to the cross section ($\sigma \approx 1/\beta x_{IP}^a Q^4$).
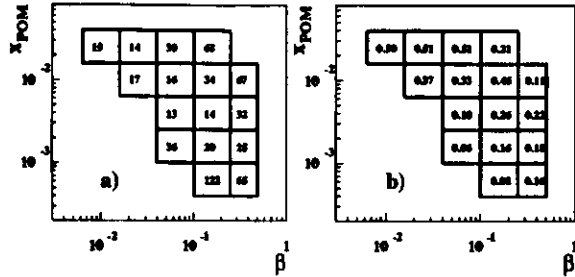
Figure 10.4: a) correction and b) purity factors for the selected $F_2^{D(3)}$ bins

10.2 Systematic checks

Several systematic checks were performed in order to estimate the uncertainties due to the selection cuts, background determination and acceptance corrections. As mentioned in chapter 8, the estimate of the systematic uncertainty is strongly affected by the statistics of the data sample, depending on the population of the bin.

Systematic errors due to the deep inelastic scattering event selection were evaluated in the following way:

1) the lower Q^2 cut was raised to $6GeV^2$ to study the possible effects of a strong migration of low Q^2 events towards higher values. The relative changes in the $F_2^{D(3)}$ values were of the order of 10%.

2) the upper Q^2 cut was raised to $30GeV^2$ to increase statistics and check the stability of the bin centering correction in Q^2. The $F_2^{D(3)}$ changes were in general below 20%.

3) the cut on E'_e was decreased from 10 to $8GeV$ to the study the effect of a possible mismatch of the shower profiles of data and Monte Carlo at small energies. The variation of $F_2^{D(3)}$ was less than 20% in each bin.

4) the y_{JB} cut was removed. Changes around 10% were observed.

5) the δ cut was raised from $35GeV$ to $40GeV$, to study the effect of radiative corrections. This resulted in changes of the order of 3%.

6) the DA variables were used instead than the electron ones to reconstruct the kinematics of the deep inelastic event resulting in changes of the order of 15% and in general below 30%.

7) the box cut was lowered to $12 \times 12cm$ to study the effects of the electron position reconstruction. The changes were of the order of 10%.

8) a vertex was required with $|Z_{vtx}| \leq 40cm$. The changes were of the order of 3%.
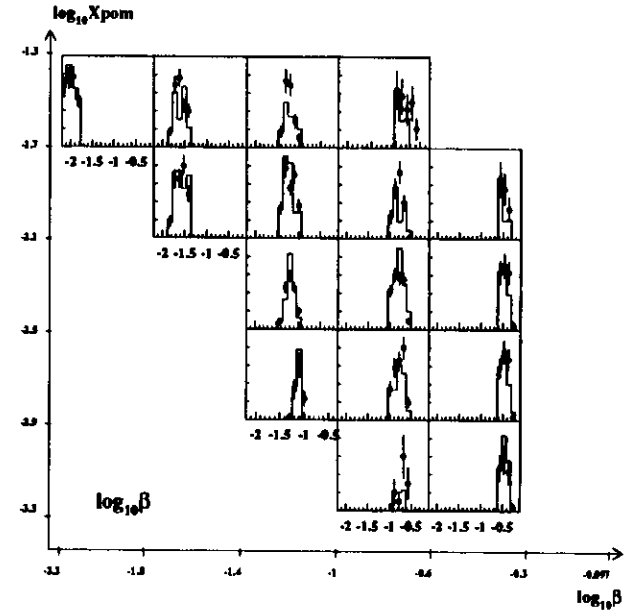
Figure 10.5: Distribution of $log_{10}\beta$ for data (dots) and MC (RAPGAP, solid line) in the selected bins for the $F_2^{D(3)}$ analysis.

Systematic errors due to the LPS diffractive event selection were evaluated in the following way:

9) the cut on the χ^2_{ndof} of the track was lowered to 6 to study possible mismatches between data and Monte Carlo. The changes in $F_2^{D(3)}$ were of the order of 5%.

10) the cut on the distance of approach to the beam pipe Δ_{pipe} was raised from 0.05 to 0.1 leading to small changes (of the order of 5%).

11) the cut on $E + p_z$ was raised from $1655GeV$ to $1670GeV$. Changes around 4% were observed.

12) a cut on the p_x of the track was performed $(0.25 < p_x < 0.3GeV)$ in order to study acceptance effects at the edges of the measured p_x range. This cut affects severely the statistics of the sample and leads to strong fluctuations. The changes in $F_2^{D(3)}$ were around 20%, with higher values in the less populated bins.

Errors due to the acceptance correction procedure were estimated as following:

13) the NZ model was used instead than RAPGAP for unfolding the data. The changes to $F_2^{D(3)}$ were tipically $\simeq 20 \div 30\%$.
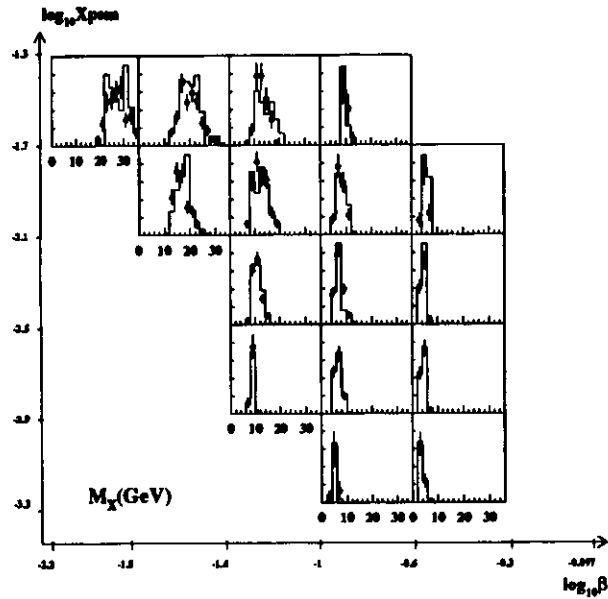
Figure 10.6: Distribution of M_X for data (dots) and MC (RAPGAP, solid line) in the selected bins for the $F_2^{D(3)}$ analysis.

14) an unfolding method based on the Bayes theorem was used in order to correct the data for acceptance and smearing. Changes around 15% were observed.

15,16) the input MC t distribution was reweighted by increasing (decreasing) of one unit the slope of its exponential behaviour in order to check the sensitivity of the corrections to the input model. The effect was a change of 3% and 4% respectively.

17) similarly the input MC W distribution was changed to be $W^{1.8}$ with a change of less than 10% in $F_2^{D(3)}$.

18) the x_{IP} dependence of the bin centering corrections was changed from $1/x_{IP}^{1.3}$ to $1/x_{IP}^{1.16}$ with negligible change in the result.

The deviation in percentage relative to the central value of $F_2^{D(3)}$ is presented in Fig. 10.7 in each bin for the 18 different systematic checks. The values of the above listed uncertainties are added in quadrature to give the total systematic error on each $F_2^{D(3)}$ point.
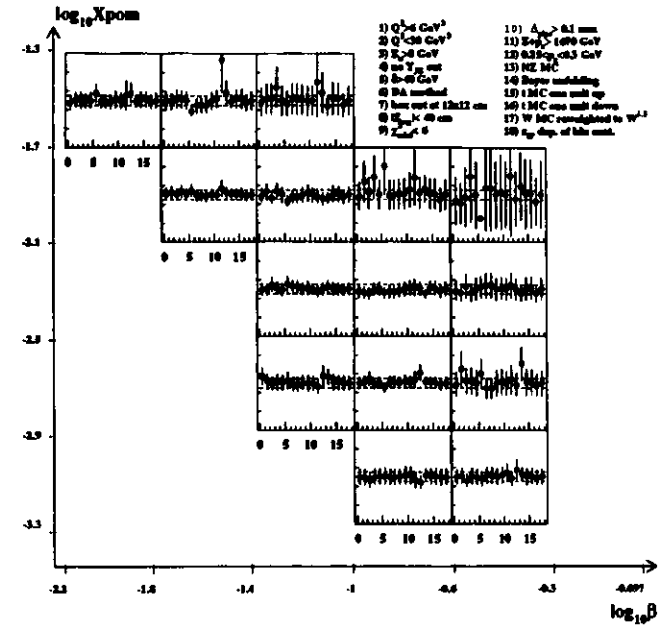
Figure 10.7: Percentage deviation of $F_2^{D(3)}$ from the central value for the 18 systematic checks listed in section 10.2. The dashed lines indicate a $\pm 20\%$ variation.

10.3 Results

The results for $F_2^{D(3)}$ are summarised in Table 10.1. The statistical errors include statistical uncertainties both from the data and the Monte Carlo samples used for the acceptance corrections. Fig. 10.8 displays the results for $F_2^{D(3)}$ as a function of x_{IP} for different bins of β. For the three β intervals $\beta = 0.07, 0.175, 0.375$ the x_{IP} dependence can be fitted to the form:

$$b_i \cdot (1/x_{IP})^a,$$

where the normalisation constants b_i are allowed to vary while the exponent a is the same in each β interval, yielding a value for a of:

$$a = 1.20 \ \pm 0.09 \ (stat.) \ ^{+0.1}_{-0.3} \ (sys.),$$

with a χ^2 of 4.2 per 9 degrees of freedom. A simultaneous fit to the x_{IP} and β dependence as given by eq. 9.3 gives the following result for a:

$$a = 1.21 \ \pm 0.085 \ (stat.) \ ^{+0.1}_{-0.3} \ (sys.),$$

with a χ^2 of 4.4 per 10 degrees of freedom. The systematic errors (see Fig. 10.9) are calculated by refitting the $F_2^{D(3)}$ values according to the variations listed in the previous section.
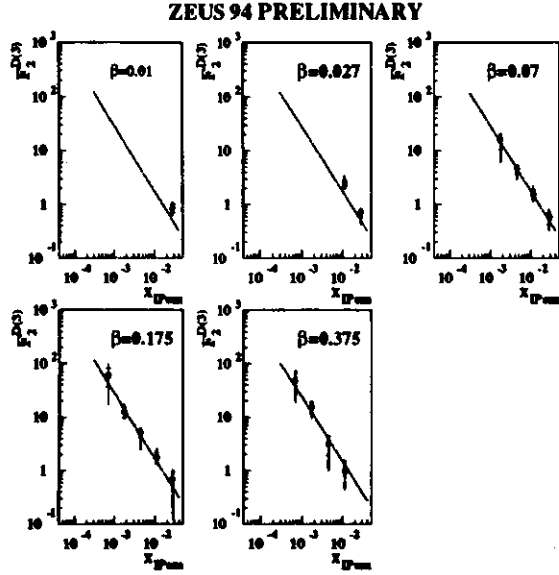
Figure 10.8: The results of $F_2^{D(3)}$ with the parametrisation obtained from the fit. The inner error bars are the statistical uncertainties, while the outer error bars correspond to the statistical and systematic uncertainties added in quadrature.

Within the present accuracy the data are consistent with the assumption of a universal $x_{I\!P}$ dependence, with the inclusion of the unprecedented range of low β values.

In order to study the β-dependence of $F_2^{D(3)}$, a fit to the parametrisation contained in eqn. 9.3 is performed a second time with $a = 1.20$. The results of the fit are:

$$b = 0.014 \pm 0.005 \ (stat.)^{+0.005}_{-0.003} \ (sys.),$$

$$c = 1.03 \pm 0.49 \ (stat.)^{+0.5}_{-0.46} \ (sys.),$$

with a χ^2 of 4.5 for 11 degrees of freedom. A fit without the $(1-\beta)^2$ soft contribution results in χ^2 of 53 for 11 degrees of freedom. This confirms one of the conclusions of the 1993 analysis, i.e. that a soft component is required in the pomeron structure function. This statement is of course even more strongly supported as the measured β range is shifted, in comparison with the 1993 analysis, towards smaller values of β where a sea component of the structure function, if existing, should dominate.

The β-dependence is furthermore investigated by integrating $F_2^{D(3)}$ over the measured $x_{I\!P}$ range $(6.3 \cdot 10^{-4} < x_{I\!P} < 10^{-2}$ was chosen in order to allow a comparison with the 1993 data)

$Q^2 (GeV^2)$	β	x_{IP}	N_{obs}	$F_2^{D(3)}$	stat.	sys.
12.5	0.01	0.028	27	0.857	0.152	$+0.210$ -0.212
12.5	0.027	0.028	34	0.678	0.112	$+0.223$ -0.125
12.5	0.027	0.011	28	2.395	0.296	$+0.230$ -0.855
12.5	0.07	0.028	19	0.562	0.140	$+0.202$ -0.190
12.5	0.07	0.011	28	1.515	0.292	$+0.333$ -0.638
12.5	0.07	0.0044	28	4.527	0.813	$+1.448$ -0.502
12.5	0.07	0.0017	5	15.269	4.828	$+7.923$ -2.166
12.5	0.175	0.028	5	0.683	0.258	$+0.498$ -0.217
12.5	0.175	0.011	21	1.761	0.415	$+0.141$ -0.084
12.5	0.175	0.0044	33	4.897	0.828	$+2.303$ -0.980
12.5	0.175	0.0017	24	12.462	2.786	$+1.744$ -3.614
12.5	0.175	0.0007	4	59.628	22.567	$+36.377$ -32.798
12.5	0.375	0.011	7	0.963	0.482	$+0.221$ -0.296
12.5	0.375	0.0044	5	3.113	1.176	$+1.774$ -0.844
12.5	0.375	0.0017	21	15.194	3.581	$+4.802$ -3.632
12.5	0.375	0.0007	8	49.664	18.771	$+24.362$ -15.39

Table 10.1: ZEUS LPS 1994 $F_2^{D(3)}$ results. The values are corrected for the run by run acceptance dependence which results in an overall shift of ~ +14%.

using the fitted $x_{I\!P}$ dependence:

$$\tilde{F}_2^{D(2)}(\beta, Q^2) \equiv \int_{0.00063}^{0.01} F_2^{D(3)}(\beta, Q^2, x_{I\!P}) dx_{I\!P}. \tag{10.5}$$

The derivation is strongly dependent upon the assumption that a universal $x_{I\!P}$ holds in all regions of β and Q^2, in particular in the regions where this hypothesis cannot be tested. The $\tilde{F}_2^{D(2)}$ values as a function of β are shown in Fig. 10.10 together with the parametrisation (solid line) obtained from the fit to eqn. 9.3. The dotted line corresponds to the hard $\beta(1-\beta)$ contribution. The $\tilde{F}_2^{D(2)}$ values and errors are listed in Table 10.2.

$Q^2 (GeV^2)$	β	$F_2^{D(2)}$	stat.	sys.
12.5	0.01	0.072	0.019	$+0.021$ -0.017
12.5	0.027	0.075	0.026	$+0.025$ -0.023
12.5	0.07	0.060	0.026	$+0.030$ -0.023
12.5	0.175	0.100	0.035	$+0.040$ -0.034
12.5	0.375	0.079	0.038	$+0.038$ -0.051

Table 10.2: ZEUS LPS 1994 $\tilde{F}_2^{D(2)}$ results. The values are corrected for the run by run acceptance dependence which results in an overall shift of ~ +14%.

The 1993 $\tilde{F}_2^{D(2)}$ values and their parametrisation (dashed line), included in the same plot, show a $\simeq 30\%$ higher normalisation factor. The discrepancy is observed whenever the cross
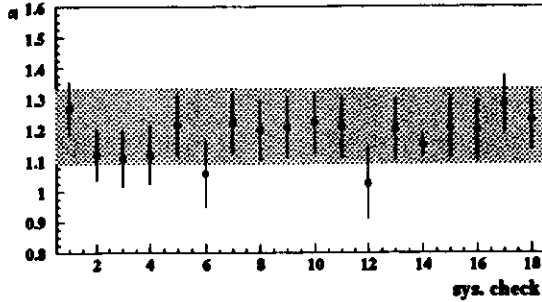
Figure 10.9: The value of α for each of the systematic checks is plotted versus the systematic check number as listed in section 10.2. The biggest variations, which exceed the 10% range indicated by the shaded band, correspond to a restriction of the proton's p_z range, which strongly affects the available statistics, and to the use of the DA variables.

Figure 10.10: $\tilde{F}_2^{D(2)}$ versus β for the 1994 LPS analysis and one Q^2 subset of the 1993 analysis. The parametrisation discussed in the text is indicated by the full (dashed) line for the 1994 (1993) analysis. The dotted line corresponds to the 1994 parametrisation $\beta(1-\beta)$ hard contribution. The inner error bars show the statistical errors and the outer bars the statistical and systematic errors added in quadrature.

section, as obtained with a direct tag of the diffracted proton, is compared with the cross sections measured with the indirect methods, either the requirement of a large rapidity gap or a small not exponentially suppressed hadronic invariant mass M_X [119] (see Fig 10.11), both by ZEUS and H1 [120].

One possible explanation, already touched in chapter 7, is that, by tagging the forward proton a full host of "background" processes, such as diffractive scattering on pions and other reggeons rather than pomeron, and proton dissociative states, are automatically discarded.

10.4   The diffractive differential cross section $d\sigma/dM_x$

From the diffractive structure function $F_2^{D(3)}$ (or, more precisely, from the differential cross section in β, x_{IP} and Q^2) it is possible to obtain, through a jacobian transformation, the differential cross section in M_X as a function of W and Q^2, since every point of the (β, x_{IP}, Q^2) phase space maps into a unique point of the $(M_X, W$ and $Q^2)$ space.

As mentioned in chapter 1, in a Regge type description, the W dependence of the diffractive cross section is of the form

$$\frac{d\sigma(M_X, W, Q^2, t)}{dt\,dM_X} \propto (W^2)^{2\alpha_{IP}(0)-2} \cdot e^{t(b_0 + 2\alpha'_{IP}\ln(W^2/M_X^2 + Q^2)))}, \qquad (10.6)$$

where $\alpha_{IP}(t) = \alpha_{IP}(0) + \alpha'_{IP} t$ is the pomeron trajectory. Averaging over t the cross section in each (M_X, Q^2) interval is fitted to the form:

$$\frac{d\sigma(M_X, W, Q^2)}{dM_X} \propto (W^2)^{2\bar{\alpha}_{IP}-2}, \qquad (10.7)$$

where $\bar{\alpha}_{IP}$ stands for $\alpha_{IP}(t)$ averaged over the t distribution. The fit has been performed in three M_X ranges ($M_X = 3.5 - 6, 6 - 10.5, 10.5 - 17 GeV$) by considering $\bar{\alpha}_{IP}$ and the three normalisation contants as free parameters. A value of:

$$\bar{\alpha}_{IP} = 1.1 \pm 0.04 \ (stat.) \ ^{+0.04}_{-0.16} \ (sys.)$$

has been obtained. Note that the W dependence of $\frac{d\sigma}{dM_X}$ for fixed Q^2 and β is equivalent to the x_{IP} of $F_2^{D(3)}$, the values of α and α_{IP} being connected by the relation $\bar{\alpha}_{IP} = (\alpha + 1)/2$. The results are displayed in Fig 10.12.

10.5   Summary

The LPS has considerably improved the measurement of the diffractive structure function with regard to the enlargement of the kinematical range and to the purity of the event selection. The abolition of the constraint in the M_X range allows to vary freely the value of the scaling variable $\frac{M_X^2}{Q^2}$ thus probing possibly different regimes of diffraction (i.e. the valence and sea component of the exchange) at every point in Q^2.

The study of the Q^2 evolution is presently prevented by the restricted statistics. The same limitation holds for the determination of the complete structure function $F_2^{D(4)}(\beta, Q^2, x_{IP}, t)$.

Within the present limits the dependence in x_{IP} is consistent with the expectation of the "soft" pomeron models. The β-dependence of the pomeron structure function requires a susbstantial contribution from a "sea" component at low β values.

When compared with the previous measurements, the normalisation appears to be consistently lower ($\sim 30\%$) indicating that, in a selection not based on the direct measurement of the proton, a noticeable portion of events could originate from non pomeron-mediated processes (e.g. dissociation of the proton into a resonance or a higher mass state and Reggeon exchange).

■ZEUS 93 – etamax Q²=12
■ H1 94 prel Q²=12 ▲ZEUS 94 LPS Q²=12.5

β=0.90 H1

β=0.65 H1

β=0.37 ZEUS
β=0.37 LPS
β=0.4 H1

β=0.17 ZEUS
β=0.17 LPS
β=0.2 H1

β=0.10 H1

β=0.07 LPS

β=0.027 LPS
β=0.04 H1

β=0.01 LPS

x_{IP}

x_{IP}
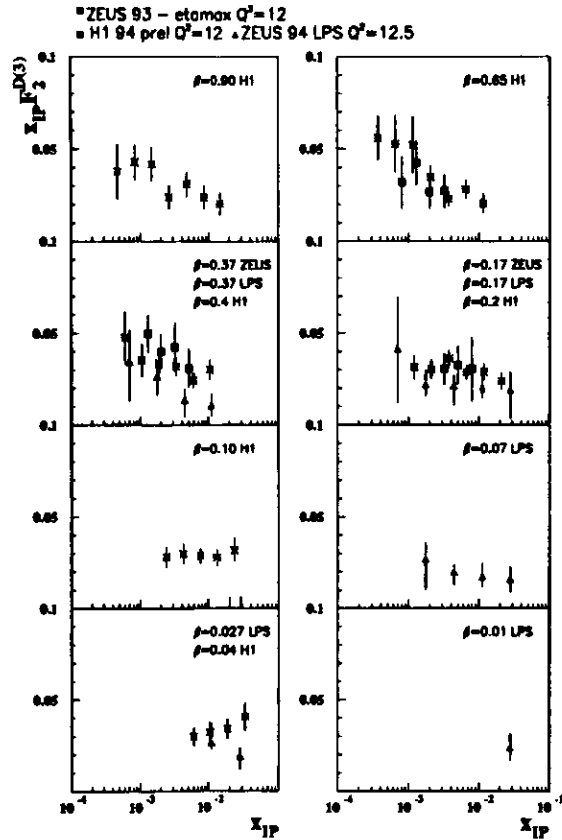
Figure 10.11: $x_{IP} \cdot F_2^{D(2)}$ as a function of x_{IP}. Comparison between the 1993 data, the 1994 LPS data and the H1 preliminary data in compatible Q^2 and β ranges.

ZEUS 1994 PRELIMINARY

28.5<M_x<45.5 GeV · 17<M_x<28.5 GeV · 10.5<M_x<17 GeV · 6<M_x<10.5 GeV · 3.5<M_x<6 GeV

W(GeV)
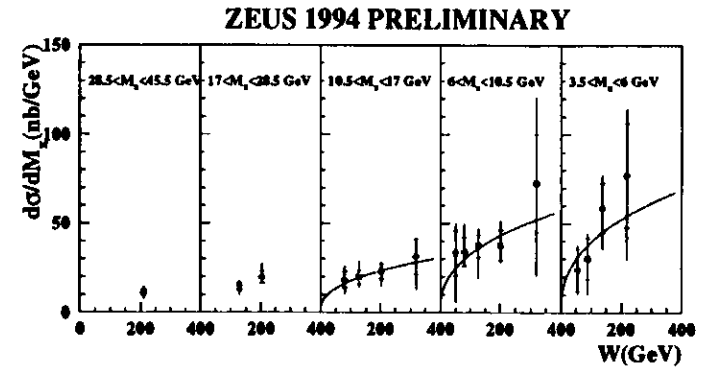
Figure 10.12: The differential cross section $\frac{d\sigma}{dM_X}$ as a function of W at $Q^2 = 12.5 GeV^2$. The inner error bars show the statistical errors and the outer bars the statistical and systematic errors added in quadrature. The curves show the results from fitting all cross sections to the form $\frac{d\sigma(M_X,W,Q^2)}{dM_X} \propto (W^2)^{2\alpha_{IP}-2}$ with a common α_{IP}, see text.

Bibliography

[1] see e.g. F. Halzen and A. D. Martin, Quarks and Leptons, J. Wiley, New York (1984).

[2] T.P. Cheng and L.F. Li, Gauge theory of elementary particle physics, Oxford University Press, Oxford (1984).

[3] M. N. Rosenbluth, Phys.Rev. 79 (1950)615.

[4] R. E. Taylor, H. W. Kendall and J. I. Friedman, Nobel Prize lectures, Rev.Mod.Phys. 63 No. 3 (1991)573.

[5] W. K. H. Panofsky, in the Proceedings of the 14th International Conference on High Energy Physics, ed. J. Prentki and J. Steinberger, Vienna (1968).

[6] R. P. Feynman, Phys.Rev.Lett. 23 (1969)1415.

[7] J. D. Bjorken, Phys.Rev. 179 (1968)1547;
J. D. Bjorken, Phys.Rev. 185 (1969)1975

[8] R. Taylor, H. Kendall and J. Friedman, Rev. Mod. Phys, 63 (1991).

[9] R. Brandelik et al., Evidence for planar events in e^+e^- annihilation at high energies, Phys. Lett. B86 (1979)243.

[10] C. G. Callan and D. Gross, Phys.Rev.Lett 22 (1969)156.

[11] M. Gell-Mann and Y. Ne'eman, The Eightfold Way, Benjamin, New York (1964).

[12] G. Zweig, CERN preprints 8182/TH 401 and 8182/TH 412, (1964).

[13] V. N. Gribov and L. N. Lipatov, Sov.Journ.Nucl.Phys. 15 (1975)438,765;
G. Altarelli and G. Parisi, Nucl.Phys. B126 (1977)298.

[14] L. V. Gribov, E. M. Levin and M. G. Ryskin, Phys.Rep. 100 (1983)1.

[15] L.N. Lipatov, Sov. J. Nucl. Phys. 23 (1976) 338;
Y.Y. Balitsky and L. N. Lipatov, Sov. J. Nucl. Phys. 28 (1978)822;
E.A. Kuraev, L. N. Lipatov and V. S. Fadin, Sov. Phys. JETP 45 (1977)199.

[16] Yu. L. Dokshitzer, Sov.Phys.JETP 46 (1977)641.

[17] J. Bjorken, SLAC summer school 1993.

[18] P.D.B. Collins, An introduction to Regge theory and high energy physics, Cambridge university press, Cambridge (1977).

[19] A. Donnachie and P.V. Landshoff, Physics Letters B296 (1992)227.

[20] WA91 Collab.: S. Abatzis et al., Physics Letters B324 (1994)509.

[21] D.R.O Morrison, CERN preprint D.Ph.II/Phys 73-46.

[22] A.H. Mueller, Phys. Rev. D2 (1970)2963.

[23] ZEUS Collab., M. Derrick et al., Measurement of total and partial photon proton cross-sections at 180 GeV center of mass energy. Z. Phys. C63 (1994)391–408.
H1 Collab., T. Ahmed et al., Measurement of the total photon proton cross section and its decomposition at 200 GeV centre of mass energy, Z.Phys. C69(1995)27.

[24] ZEUS Collab., M. Derrick et al., Measurement of elastic ρ^0 photoproduction at HERA. Z. Phys., C69 (1995)39–54.
H1 Collab., T. Ahmed et al., Elastic photoproduction of ρ^0 mesons at HERA, Nucl.Phys. B463(1996)3.

[25] ZEUS Collab., M. Derrick et al., Measurement of the cross-section for the reaction $\gamma p \rightarrow J/\psi p$ with the ZEUS detector at HERA. Phys. Lett. B350 (1995)120–134.
H1 Collab., T. Ahmed et al., Elastic and inelastic photoproduction of J/ψ mesons at HERA, Nucl.Phys. B472(1996)3.

[26] L. Frankfurt et al., Hard diffractive electroproduction of vector mesons in QCD, HEP-PH/9509311.
S.J. Brodsky et al., Phys. Rev. D50 (1994)3134.
M.G. Ryskin, Z. Phys. C57 (1993)89.
J. Nemchik et al., Phys. Lett. B341 (1994)228.

[27] A. Levy, Soft interactions at high energy, DESY 95-204 (1995).

[28] M. Bertini, M. Giffon and E. Predazzi, Two pomerons?, LYCEN/9504 (1995).
P. V. Landshoff: The two pomerons, HEP-PH-9410250 (1994).

[29] L.L. Jenkovszky, Ukrainian journal of physics, Vol.41 (1996)270.

[30] J.T. Cudell et al., The BFKL pomeron: can it be detected?, DAMTP-96/02 (1996).

[31] W. Buchmüller, Phys. Lett. B335 (1994)479.
W. Buchmüller and A. Hebecker, DESY 95-077.

[32] B. Foster et al., Nucl. Phys., Proc.Suppl. B32 (1993)181.

[33] ZEUS Collab., Proposal for a Small Angle Rear Track Detector for ZEUS, ZEUS-Note 93-016, February 1993.

[34] F. Benotto et al., The LPS trigger system, ZEUS-Note 95-165.

[35] A. Stajano, Silicon Detectors for the Leading Proton Spectrometer at ZEUS, proceedings of the Third International Workshop on Vertex Detectors, IUHEE-95-1.

[36] E. Barberis et al., Design, testing and performance of the frontend electronics for the LPS silicon microstrip detectors, Nucl. Instr. and Meth. A364 (1995)507-515.

[37] E. Barberis et al., A fast shaping amplifier-comparator integrated circuit for silicon strip detectors, SCIPP-92-40, Presented at the Nuclear Science Sym., Orlando, Fl, 26-31, Oct. 1992.

[38] E. Barberis et al., A low power bipolar amplifier integrated circuit for the ZEUS silicon strip system, SCIPP-92-35, Nucl. Phys. B, Proc Suppl 32(1993)513-518.

[39] N. Cartiglia et al., Radiation hardness measurement on bipolar test structures and an amplifier-comparator circuit, SCIPP 92-3530, 1992.

[40] J.De Witt, The Digital Time Slice Chip, University of California, Santa cruz, June 7, 1991.

[41] J. Rahn et al., Testing the yield of an amplifier-discriminator chip fabricated in Tektronix SHPi, SCIPP 93-02, 1993.

[42] E. Barberis et al., Capacitances in silicon microstrip detectors, SCIPP-93-16, Presented at the Int. Symp. on Development and Application of Semiconductor Tracking Detector, Hiroshima, 1993

[43] E. Barberis et al., A test station for silicon microstrip detectors and associated electronics, DPF92, Word Science.

[44] The ZEUS Detector, Status Report 1993, DESY (1993).

[45] CMZ, A Source Code Management System, User's Guide & Reference Manual.

[46] K.Long, How to generate input to MOZART, ZEUS-Note 91-13.

[47] R. Brun et al., GEANT3 user's guide and reference manual.

[48] R. van Woudenberg, ZGANA Version 3.05/01 User Manual and Documantation (1993).

[49] E.Tscheslog, Zeus Reconstruction Program, Organisation and Control, ZEUS-Note 91-37.

[50] A. F. Whitfield, A measurement of vector meson production in ep collisions with the ZEUS detector at HERA, Ph.D. Thesis, University of London and Imperial College (1996).

[51] L. Lamberti and A. Solano, How to use MC weights for physics analysis, ZEUS-Note 94-091, July 1994.

[52] K.Goulianos, Phys. Rep. 101 (1983)169.

[53] H. Jung, DESY report 93-182

[54] A. Donnachie and P.V. Landshoff, Nucl. Phys. B244 (1984)322; Phys. Lett. B296 (1992)227.

[55] G. Ingelman and P. Schlein, Phys. Lett. 152B (1985) 256.

[56] K.H. Streng, in Proc. of the Workshop "Physics at HERA", p. 365, ed. R.D. Peccei (Hamburg 1987).

[57] K. Kwiatkowski, H. Spiesberger and H.-J. Möhring, Proceedings of the Workshop "Physics at HERA" vol. 3, DESY (1992)1294.

[58] L. Lönnblad, Comp. Phys. Comm. 71 (1992) 15; L. Lönnblad, Z. Phys. C65 (1995)285.

[59] T. Sjöstrand and M. Bergtsson, Comp. Phys. Comm. 43 (1987)367.

[60] POMPYT 1.0: P. Bruni and G. Ingelman (unpublished); DESY 93-187; Proceedings of the Europhysics Conference on HEP, Marseille 1993, 595.

[61] T. Gehrmann and W.J. Stirling, Durham preprint DTP/95/26.

[62] UA4 Collab., M. Bozzo et al., Phys. Lett. 136B (1984)217.

[63] N.N. Nikolaev and B.G. Zakharov, Z. Phys. C53 (1992)331.

[64] M. Genovese, N.N. Nikolaev and B.G. Zakharov, KFA-IKP(Th)-1994-37 and CERN-TH.13/95.

[65] F. E. Low, Phys. Rev. D12 (1975)163; S. Nussinov, Phys. Rev. Lett. 34 (1975)1286 and Phys. Rev. D14 (1976)246.

[66] A. Solano, Ph.D. Thesis, University of Torino 1993 (unpublished); A. Solano, Proceedings of the International Conference on Elastic and Diffractive Scattering, Nucl. Phys. B (Proc. Suppl.) 25 (1992)274;

[67] M. Kasprzak, EPSOFT - a Monte Carlo generator of soft photon-proton collisions, ZEUS-Note 95-069, June 1995.

[68] G. Marchesini, B.R. Webber, G. Abbiendi, I.G. Knowles, M.H. Seymour and L. Stanco, Comput. Phys. Commun. 67 (1992)465.

[69] H. Abramowicz, E.M. Levin, A. Levy, U. Maor; Phys. Lett. B269 (1991)465.

[70] M.G. Ryskin, Z. Phys. C57 (1993)89.

[71] M. Arneodo, L. Lamberti and M.G. Ryskin, submitted to Comp. Phys. Comm. (1995).

[72] K. Muchorowski, private communication.

[73] Y. Azimov, Y. Dokshitzer, V. Khoze, S. Troyan, Phys. Lett. B165 (1985)147; G. Gustafson, Phys. Lett. B175 (1986)453; G. Gustafson, U. Pettersson Nucl. Phys. B306 (1988)746; B. Andersson, G. Gustafson, L. Lönnblad, U. Pettersson Z. Phys. C43 (1989)625.

[74] A.D. Martin, W.J. Stirling and R.G. Roberts, Phys. Rev. D50 (1994)6734.

[75] A.D. Martin, W.J. Stirling and R.G. Roberts, Phys. Rev. D51 (1995)4756.

[76] B. Foster, ZEUS tracking meeting, 1992.

[77] LPS group: On the 1994 LPS efficiency, ZEUS-Note 94-156.

[78] S.M.Fischer, P.Palazzi, ADAMO Entity-Relationship Programming System, Reference Manual version 3.3.

[79] LARSEN,Henning. Leading Proton Spectrometer - Serial Readout Controller. CERN-LAA Internal Report, 1991.

[80] LARSEN,Henning. Leading Proton Spectrometer - Read-Out Controller. CERN-LAA Internal Report, 1994.

[81] C. Nemoz, ZEUS Leading Proton Spectrometer, Online Definition Data Language ZEUS-Note 94-100.

[82] D.E. Dorfan et al., Nucl. Instr. and Meth. A 342 (1994)260.

[83] R. Sacchi, Ph.D. Thesis, University of Torino 1996 (unpublished).

[84] T. Massam, BEAM9, a program for LPS aperture and acceptance calculations.

[85] LPS Group, LPS alignment, Calibration and Reconstruction for 1994 Data, ZEUS-Note in preparazione.

[86] G.Anzivino et al., Intallation and Alignment of the HERA Pots, ZEUS-Note 91-023.

[87] T.Massam et al., Alignment Optics for the Leading Proton Spectrometer, ZEUS-Note 92-036.

[88] T.Massam et al., Motor Positions and Clock Gauge Calibration, LPS Internal Note (1995).

[89] ZEUS Collab., M. Derrick et al., Measurement of elastic ρ^0 photoproduction at HERA, Z. Phys., C69 (1995) 39-54.

[90] T.Massam et al., The Leading Proton Spectrometer: High Precision Momentum Calibration, ZEUS-Note 94-075.

[91] F. Jacquet and A. Bloudel, Proceedings of the Study for an ep facility for Europe, DESY 79/48 (1979)391.

[92] S. Maselli and A. Solano, ZEUS-Note-91-112.

[93] S. Maselli and R. Sacchi, ZEUS-Note-92-43.

[94] D. Bandyopadhyay, MUTRIG: A Third Level Trigger Muon Finder, ZEUS-Note 93-013, February 1993.

[95] F.S. Chlebana, First measurement of the proton structure function F_2 with the ZEUS detector, Ph.D. Thesis, University of Toronto (1993).

[96] S. Bentvelsen, Measurement of the proton structure function at HERA using the ZEUS detector, Ph.D. Thesis, University of Amsterdam and NIKHEF-H(1993).

[97] S. Bentvelsen, J. Engelen and P. Kooijman, Proceedings of the workshop on physics at HERA, DESY Vol.1 (1992)23.

[98] A. Prinias, Measurement of the F_2 proton structure function using the ZEUS detector, Ph.D. Thesis, University of London and Imperial College (1995).

[99] R. Sinkus and H. Abramowicz, Electron identification with neural networks at ZEUS, ZEUS-Note 93-11, November 1993.

[100] T. Doeker et al., Electron position reconstruction, ZEUS-Note 94-123, May 1994.

[101] J. Ng and W. Verkerke, An overview of SRTD analysis, ZEUS-Note 95-037, July 1995.

[102] E. Gallo, A measurement of F_2 from 2.5pb^{-1} in 1994, ZEUS-Note 95-142, September 1995.

[103] The Structure Function Group, A determination of F_2 with the 1992 data, ZEUS-Note 93-078, July 1993.

[104] J. Biltzinger, Effect of noise on the reconstruction of kinematical variables in DIS events, ZEUS-Note 93-073, July 1993.

[105] J. Biltzinger, Uranium calorimeter noise of 1994 data, ZEUS-Note 95-02, June 1995.

[106] ZEUS Collab., M. Derrick et al., Measurement of the proton structure function F_2 at low x and low Q^2 at HERA, Z. Phys., C69 (1996)607-620.

[107] P.V. Landshoff, The soft pomeron, DAMTP 96/48

[108] E.Barberis, N.Cartiglia, J.Rahn, R.Sacchi, A,Stajano, LPSWEIGHT.CAR: a reweighting routine for 1994 LPS data analysis, ZEUS-Note 95-105.

[109] F.Willeke, private communication.

[110] M.Albrow et al., Nucl. Phys. B54 (1973)6.

[111] ZEUS Collab., M. Derrick et al., Phys. Lett. B356 (1995)601. H1 Collab., T. Ahmed et al., Nucl.Phys. B468 (1996)3.

[112] G. D'Agostini, A multidimensional unfolding method based on Bayes' theorem, DESY 94-099, June 1994.

[113] ZEUS Collab., M. Derrick et al., Phys. Lett. B315 (1993)481.

[114] ZEUS Collab., M. Derrick et al., Phys. Lett. B332 (1994)228.

[115] ZEUS Collab., M. Derrick et al., Phys. Lett. B346 (1995)399.

[116] H1 Collab., T. Ahmed et al., Phys. Lett. B345 (1995)3.

[117] H1 Collab., T. Ahmed et al., Phys. Lett. B348 (1995)681.

[118] ZEUS Collab., M. Derrick et al., Z. Phys. C65 (1995)379.

[119] ZEUS Collab., M. Derrick et al., Z. Phys. C70 (1996)391.

[120] A. Metha, Ph.D. Thesis, "Measurement of the Diffractive Proton Structure Function and Calibration of the Forward Muon Detector at H1", Manchester University, RALT-037.